NASA CR-122407

N72-24289

NUS-786/1
Volume 1

FINAL REPORT FOR MODIFICATION OF CODES NUALGAM AND BREMRAD

For

NATIONAL AERONAUTICS AND
SPACE ADMINISTRATION
Goddard Space Flight Center
Glenn Dale Road
Greenbelt, Maryland

CONTRACT NAS5-11781

By

J. J. Steyn

R. Huang

and

H. Firstenberg

May 1971

CASE FILE
COPY

NUS CORPORATION
4 Research Place
Rockville, Maryland 20850

NUS CORPORATION

NUS–786/1
Volume 1

FINAL REPORT FOR MODIFICATION OF CODES NUALGAM AND BREMRAD

For

NATIONAL AERONAUTICS AND SPACE ADMINISTRATION
Goddard Space Flight Center
Glenn Dale Road
Greenbelt, Maryland

NASA Contract Number: NAS5–11781

By

J. J. Steyn

R. Huang

and

H. Firstenberg

May 1971

NUS CORPORATION
4 Research Place
Rockville, Maryland 20850

ABSTRACT

Three computer codes have been developed for the IBM-360 computer, namely: NUGAM2, NUGAM3 and SSALB. Two existing computer codes have been modified and made operational on the IBM-360 computer, namely: BREMRAD and 05S. The existing codes are described summarily and the new codes are detailed.

The NUGAM2 code predicts forward and backward angular energy differential and integrated distributions for gamma photons and fluorescent radiation emerging from finite laminar transport media. It determines buildup and albedo data for scientific research and engineering purposes; it also predicts the emission characteristics of finite radioisotope sources. It has been shown in this report that Sample results, in very good agreement with available published data, are presented. The code predicts data for many situations in which no published data is available in the energy range up to 5 MeV.

The NUGAM3 code predicts the pulse height response of inorganic (NaI and CsI) scintillation detectors to gamma photons. Because it allows the scintillator to be clad and mounted on a 'photomultiplier' as in the experimental or industrial application, it is a more practical and thus useful code than others previously reported. Results are in excellent agreement with published Monte Carlo and experimental data in the energy range up to 4.5 MeV.

The SSALB code determines single scatter albedo data analytically and is thus applicable to certain engineering problems. It was developed in support of the NUGAM2 code.

TABLE OF CONTENTS

LIST OF FIGURES

LIST OF TABLES

1. INTRODUCTION

This final report was prepared by NUS CORPORATION for the National Aeronautics and Space Administration, Goddard Space Flight Center, under Contract NAS5-11781. The work scope consisted of modifying existing digital computer codes, namely: BREMRAD, NUALGAM and 05S.

Under contract Task I, BREMRAD(1,2) an existing IBM-7094 computer code for generating external and internal bremsstrahlung distributions, was modified. The modifications consisted of translation for operation on the NASA/GSFC IBM-360/91 computer, the redesign of code logic, the internal storage of frequently used data tabulations and the simplification of data input. The completion of this task was reported to NASA/GSFC in Technical Report NUS-TM-NA-109(3) and is thus not further discussed in this present report.

Under contract Task II, NUALGAM(4), an existing IBM-7094 computer code was modified. NUALGAM is a Monte Carlo code for calculating the emission of gamma photons from finite source media. The modifications resulted in the development of two new Monte Carlo gamma photon transport codes, NUGAM2 and NUGAM3, for operation on the NASA/GSFC IBM-360/91 computer. This report is principally concerned with describing these new codes. Also under Task II, the 05S(5) computer code package was obtained from the Radiation Shielding Information Center, Oak Ridge National Laboratory(6) and made operational on the NASA/GSFC IBM-360/91. 05S is a Monte Carlo code for calculating fast neutron transport and pulse height response distributions in organic scintillators exposed to monoenergetic neutrons. This code is described in an appendix of this report.

Code NUALGAM was derived from an existing unpublished code--ALGAM, developed at the Oak Ridge National Laboratories(7-9). ALGAM was developed for radiobiological application whereas NUALGAM was intended for the study of finite source photon number and energy distributions. Code NUALGAM predicts the angular-energy differential and integral escape of gamma photons from right-cylindrical homogeneous source media by means of the Monte Carlo technique. The modifications to NUALGAM reported herein consisted of the development of two gamma photon transport codes to predict buildup factors, albedos, fluorescent radiation emission and scintillation crystal pulse height response. The modified codes reported herein have been designated NUGAM2 and NUGAM3.

The NUGAM2 code was developed to predict the forward and backscatter angular-energy distribution of photons and fluorescent radiation emerging from finite transport media of single or laminar composition. The code predicts buildup and albedo data for either finite or semi-infinite transport media. An intermediate version of NUGAM2, namely NUGAM1, was developed by NUS for NASA/GSFC as part of the S0SC code package(10). The shield transmission capabilities of NUGAM1 have been extended and incorporated into NUGAM2.

The NUGAM3 code was developed to predict the pulse height response of inorganic scintillation crystals exposed to gamma photon radiation. It differs from previous codes which have been reported, in that the crystal model may be encased in a cladding material and mounted on a hypothetical photomultiplier.

The present final report is composed of three volumes. Volume I describes the NUGAM2 and NUGAM3 Monte Carlo codes. Section 2 of Volume I presents the theory upon which the code logistics are based while Section 3 discusses significant sample results obtained. Section 4 consists of a summary. NUGAM2 and NUGAM3 are generally separated in Volume I through the use of subsection discussion, excepting where it is otherwise expedient. The important features of the 05S code as taken from reference (5), are noted in Appendix I.

Volume II of this report consists of a code users description for each of the codes NUGAM2, NUGAM3 and 05S. The 05S code information is given in Appendix V of Volume II. In addition to a users description, Volume II also gives listings of code sample input and output; the code FORTRAN listings are omitted so that upon request a latest version may be supplied.

Volume III of this report considers the statistics of the Monte Carlo method relative to the interpretation of the NUGAM2 and NUGAM3 results. A numerical experiment using NUGAM2 code is presented and the results are interpreted.

2. THEORETICAL DISCUSSION

2.1 General

The NUGAM2 and NUGAM3 codes predict gamma photon transport distributions according to the Monte Carlo technique. Source photons are initiated stochastically and followed throughout their history in the transport medium.

The NUGAM2 code categorizes those photons which escape from the medium. The escape categorization is performed as a function of escape energy and angle with additional separation into the backward and forward directions. Thus the code predicts "all space", albedo and buildup angular-energy distributions as a function of source photon energy and transport geometry. The distributions are predicted for photon number, energy and exposure. In addition to categorizing Compton and pair production photon escape the NUGAM2 code categorizes the escape from the transport medium of the characteristic x-rays of designated elements in the medium. The code also categorizes unscattered, single and multiple scatter escapes.

The NUGAM3 code categorizes the energy-differential distribution of photon energy absorbed by a scintillation phosphor. It differs from previously published Monte Carlo scintillator response codes in that the phosphor may be encased in a cladding material and mounted on a "hypothetical" photomultiplier tube. The code predicts the energy absorption spectrum and its Gaussian distributed counterpart analogous to the experimental measurement obtained with a multichannel pulse height analyzer. In addition to pulse height response the code predicts the angular-energy distribution of photons escaping from the "detector configuration". The escape categorization is similar to that of the NUGAM2 code.

The NUGAM2 code is designed for either a right-cylinder or a rectangular parallelepiped transport medium. The NUGAM3 geometry is right-cylindrical. The multiple media in NUGAM2 are parallel discs or slabs. The multiple media in NUGAM3 consist of a scintillation phosphor eg. NaI or CsI, clad on the front and sides and backed by a cylinder-simulated photomultiplier tube.

The codes are designed to expose the transport medium to source photons originating from either a point isotropic source located outside or inside the medium (the internal source may be either a point or a uniform distribution) or parallel incident source photons.

Since the codes do not at present follow photo, Compton or pair electrons and the bremsstrahlung they generate along their torturous transport paths, the codes are upper-energy limited. NUGAM2 is valid to ~ 6.0 MeV and NUGAM3 to ~4.5 MeV. Above these energies the codes will operate but will tend to deviate progressively from a "correct" prediction.

2.2 Monte Carlo Gamma Photon Transport Theory

Codes NUGAM2 and NUGAM3 are programmed to predict gamma photon number transport in multiple media geometries. They employ the Monte Carlo technique of following and catagorizing a large number of photons from "birth to death"$^{(11, 12)}$. They use random number and probability theory combined with known interaction distributions to determine such as source and collision site spatial location, as well as trajectory energy and direction throughout each history. For the purpose of clarity the text in this section assumes and thus refers to a right-cylindrical transport geometry, unless otherwise noted.

After n interaction events in the transport medium, photon number state may be characterized as

$$N_n = N\,(E_n, \theta_n, \Phi_n, x_n, y_n, z_n; E_m, \theta_m, \Phi_m, x_m, y_m, z_m), \qquad (1)$$

where

E = photon energy
θ = polar angle
Φ = azimuth angle
x, y, z = Cartesian co ordinates
n = subscript to denote n^{th} event
m = $n-1$, a subscript; $0, 1 \ldots, m, n, \ldots$
o = subscript to denote photon history origin, i.e. ,

which describes the spectrum at the arbitrary point P_n (x_n, y_n, z_n). If interaction site P_n is outside the boundaries of the cylinder of length L and radius ρ, and P_m is within, then the "fate" of the photon is deemed as "escape", and is so tallied by the code. If an escape is recorded at P_n where $P_m = P_o$, then the photon escape energy and direction is unaltered and identical with the initial or birth values ie. uncollided escape. A typical escape history is indicated in Figure 1, where escape is shown between P_2 and P_3.

The codes employ Cartesian coordinates and direction cosines to define source and interaction positions and the intermediate trajectories. The codes are presently designed for external collimated point isotropic sources of photons, parallel incident photons and internal point or uniformly distributed sources. The determination of their various coordinates and direction cosines is described in Section 2.2.

The path length between interactions, ℓ, is a function of energy, material composition and geometry. The codes determine path length according to the Monte Carlo technique(12) as

$$\ell = \ell_1 + \ell_2 + \cdots + \ell_{j-1} + \lambda_j \left[-\log_e R_i - (\mu_1 \ell_1 + \mu_2 \ell_2 + \cdots + \mu_{j-1} \ell_{j-1}) \right] \qquad (2)$$

where

R_i = the i^{th} random number in a sequence of random numbers,

ℓ_j = actual uncollided path length of photon in medium region j, between events m and n,

λ_j = total mean free path for a photon of energy E in medium j,

μ_j = total macroscopic interaction cross-section for a photon of energy E in medium $j = \lambda_j^{-1}$.

Figure 2 illustrates a typical photon trajectory between interactions in a a three-medium transport geometry.

For a single transport medium , $j = 1$, and thus Equation (2) reduces to

$$\ell = -\lambda_1 \log_e R_i \quad . \tag{3}$$

Source photons are initiated with a probability of existence or weight W, equal to 1.0. This weight is reduced after each interaction by the ratio of the scattering to total cross-section. Thus photons are not lost to absorption unless their reducing weight drops below an assigned value, for example, 10^{-5}. Photons may be lost to absorption if their degraded energy drops below a "user" designated threshold value, eg. 0.025 MeV cutoff.

Energy deposition within the transport medium at the n^{th} interaction site is determined as

$$I_n = \frac{W_m}{\sigma_t} \left[(E_m - 1.02)\, \sigma_{pp} + E_m - E_n) \right] \quad , \text{(MeV)} \tag{4}$$

where

W_m = weight after m^{th} interaction,

E_m = photon energy before interaction (MeV),

E_n = photon energy after interaction (scattered photon), (MeV),

σ = microscopic interaction cross-section,(13-17)

pp, pe, s, t = subscripts to identify pair production, photoelectric, scattering and total cross-sections,

$\sigma_t = \sigma_{pp} + \sigma_{pe} + \sigma_s$.

Equation (4) neglects electron transport effects and is thus only totally valid where they are not significant eg. away from geometrical boundaries.

The total macroscopic Compton scattering cross-section per atom is defined as

$$\sigma_{s_i} = Z_i \cdot \sigma_{es} , \qquad (5)$$

where

Z_i = material or element atomic number,
σ_{es} = total microscopic Compton scattering cross-section per electron.

The scattering cross-section σ_{es} is obtained from the Klein-Nishina relationship as(11)

$$\sigma_{es} = 2\pi r_o^2 \left[\frac{2}{E^2} + \frac{1+E}{(1+2E)} \quad 2 + \ln(1+2E) \left(\frac{E^2-2E-2}{2E^3} \right) \right] , \qquad (6)$$

where

r_o = 2.8183 x 10^{-13}cm; classical electron radius,
E = photon energy in m_oc^2 (=0.51097 MeV) units.

The macroscopic cross-section μ is determined from the microscopic cross-section σ in accord with the relationship

$$\mu = Ao \sum_{i=1}^{i=k} \frac{\rho i \, \sigma i}{A_i} , \qquad (7)$$

where

A_o = Avogadro number; 0.6023×10^{24},
ρ = material or element density,
A = material or element atomic weight,
i = subscript to denote summation for elements; $i = 1, 2, \ldots, k$.

Photon direction and energy after a scattering are governed by the angular-differential form of the Klein-Nishina distribution, with energy related to direction by the Compton scattering relationship(11)

$$E_n = E_m/(1 + (E_m/0.51097)(1-\cos\theta_s)), \tag{8}$$

where

θ_s = photon scattering angle,
E_m = photon energy before scatter (MeV),
E_n = photon energy after scatter (MeV),

The codes select scattering angle and energy at each interaction site in accord with the algorithm of Kahn outlined in reference (18) (reproduced in Appendix II).

At photon energies greater than 2 m_oc^2 (=1.02 MeV) the codes account for the pair production phenomenon. The codes temporarily store the parent photon characteristics and initiate a daughter photon with isotropically selected direction and energy m_oc^2 (=0.51097 MeV). Upon termination of the daughter history, the parent history is recontinued. In code NUGAM2 the daughter history is initiated with twice the parent weight in order to simulate an actual photon pair. In NUGAM3, the scintillation phosphor code, two back-to-back daughters are initiated, each with the parent weight, and followed separately to termination.

2.3 Geometry

The NUGAM2 and NUGAM3 codes are designed for five different photon source geometries, namely:

I. external axial point isotropic source,
II. external parallel incidence,
III. cases I and II with collimation,
IV. internal point isotropic source,
V. internal uniformly distributed source.

The various geometries allowed are indicated in Figure 3. The angle of parallel incident photons may be user designated.

For the case of an axial point isotropic source as in Figure 3a, all source photons are initiated at the coordinates $(x_o, y_o, z_o) = (0, 0, -r)$ with direction cosine

$$\gamma_o = 1 - (1-\tau) R_i \ , \tag{9}$$

where

$\tau = r/(r^2 + \rho 2)1/2$,
ρ = radius of transport medium cylinder,
r = source-to-cylinder distance,
$R_i = i^{th}$ random number in a sequence of random numbers.

The azimuth angle is obtained as

$$\phi_o = (2R_{i+1}-1)\ \pi \ . \tag{10}$$

Direction cosines α_o and β_o are determined as

$$\alpha_o = (q^2-r^2)^{1/2} \cos\phi_o/q \quad , \tag{11}$$

and

$$\beta_o = (q^2-r^2)^{1/2} \sin\phi_o/q \ , \tag{12}$$

where

$$q = r/\gamma_o \ .$$

Collimation of the source cone is obtained by replacing the transport cylinder radius ρ with ρ', the radius of collimation.

Parallel incident photons are initiated on the front face of the transport cylinder, the $z = z_o = 0$ plane, at a radial distance d_o from the axis and at a radial angle ϕ_o where

$$d_o = R_i^{1/2} \cdot \rho \ , \tag{13}$$

and

$$\phi_o = (2R_{i+1}-1)\,\pi \quad . \tag{14}$$

If the parallel beam is collimated ρ' replaces ρ. Equation (14) is identical to Equation (10). The directional cosines are $(\alpha_o, \beta_o, \gamma_o) = (0,0,1)$.

For rectangular-parallelepiped transport geometry exposed to an axial point source, the above equations are valid where ρ is the radius of the circle circumscribing the rectangular front face. In this geometry an additional test is required to ascertain if the individual photons "hit or miss" the rectangular front face. For the special case of axial incidence the coordinates (x_o, y_o, z_o) are "user" specified. For uncollimated parallel incidence $z_o = 0$ and

$$x_o = w \cdot R_i , \tag{15}$$

$$y_o = b \cdot R_{i+1} , \tag{16}$$

where

w = rectangular width,

b = rectangular breadth

For the internally located point source case the photons are initiated at the specified coordinates (x_o, y_o, z_o). For the internal uniformly distributed cylindrical source the coordinates are chosen by random number selection as

$$z_o = R_i \cdot L , \tag{17}$$

$$x_o = d_o \cos\phi_o , \tag{18}$$

$$y_o = d_o \sin\phi_o , \tag{19}$$

where

$$d_o = \rho \cdot R_{i+1}^{1/2} , \tag{20}$$

$$\phi_o = (2R_{i+2} - 1)\,\pi , \tag{21}$$

and

$$L = \text{cylinder length.}$$

The initial direction cosines of each history for the internal sources are determined as

$$\begin{aligned} \alpha_o &= 2R_i - 1 \ , \\ \beta_o &= \cos[(2R_{i+1} - 1)\pi] . (1-\alpha_o^2)^{1/2} , \\ \gamma_o &= \sin[(2R_{i+1} - 1)\pi] . (1-\alpha_o^2)^{1/2} . \end{aligned} \tag{22}$$

For the internal uniformly distributed rectangular source the coordinates (x_o, y_o, z_o) are obtained from equations (15), (16) and (17).

When the photon path length ℓ as determined from Equation (2), exceeds the vector path in the transport geometry the photon is deemed to have escaped from the medium geometry. In this event the history is terminated and categorized with respected to its energy, direction and weight. At the termination of each history in the NUGAM2 code, the energy and exposure (dose) is tallied. At this same point in the NUGAM3 code the absorbed energy is weight distributed and tallied.

Although the code determines exact angles and location of photon escapes with respect to the transport medium boundary surface, a general categorization is carried out with respect to specific coordinate points, namely: the axial end points and geometric center. These locations (0, 0, 0), (0, 0, L/2) and (0, 0, L) are used as references points for albedo, 4π and buildup data tabulations.

If a detection band about the Z-axis is assumed to be relatively distant from the transport medium then photons escaping from any point on the medium surface and striking the band, may be considered as having the same Z-axis directional cosine, ie. the medium is viewed as if a point source. If the detection band subtends the differential solid angle $d\Omega$ at $(0, 0, 0 \leq z \leq L)$ then, the photon escape state may be characterized as

$$N = N(E, \Omega), \tag{23}$$

where

E = photon escape energy.

In Equation (23) the understood arguments and subscripts are omitted. Multiplying by differentials in energy and solid angle, the differential angular-energy photon number escape spectrum is given by

$$dN (E \quad \Omega) = N (E, \Omega) \, dE d\Omega , \tag{24}$$

keeping in mind that

$$d\Omega = \mathrm{Sin}\,\theta \, d\,\theta d\,\Phi, \tag{25}$$

where

θ = polar angle between escape vector and Z-axis; $0 \leq \theta \leq \pi$,

Φ = azimuth angle of escape vector; $0 \leq \Phi \leq 2\pi$.

Substitution of Equation (25) into Equation (24) and integration over energy and angle between desired limits, gives the total photon number escaping. The geometry for photon history escape classification is illustrated in Figure 4 for the reference point (0, 0, L/2). The escape classification geometry for the reference points (0, 0, 0) and (0, 0, L) is illustrated in Figure 5. Figure 5 gives the hemispherical segmentation for categorization of escape direction. Figure 6 gives the coded equivalent of Figure 5.

2.4 X-Ray Transport

Code NUGAM2 is programmed to predict the escape from the transport medium of characteristic K x-rays originating in the photoelectric interactions. The present code version allows this option only for geometries consisting of a single transport medium. An additional restriction limits the x-rays to those of a single element in a medium composed of one or two elements. For example the escape of either the iodine or sodium K x-rays in a sodium-iodide medium may be predicted providing no adjacent media are considered.

The number of element-B K-shell x-rays, generated at the nth interaction site in a medium composed of elements A and B, is obtained as

$$N_x = \frac{\sigma_{pe_B}}{\sigma_{pe_{A+B}}} \cdot \frac{\sigma_{K_B}}{\sigma_{pe_B}} \cdot W_m \cdot F_B \quad , \tag{26}$$

where

σ_{pe_B} = microscopic photoelectric cross-section for photons of energy E and element B,

$\sigma_{pe_{A+B}}$ = microscopic photoelectric cross-section for photons of energy E and elements A+B,

σ_{K_B} = microscopic photoelectric cross-section for photons of energy E interacting with the K-shell electrons of element B,

F_B = fluorescent yield of element B,

W_m = weight of interacting photon prior to n^{th} interaction i.e. = W_{n-1}

The cross-section σ_{K_B} is obtained from reference (17) if the cross-section σ_{pe_B} is known. Table 1 reproduced from the reference, gives values of the ratio σ_{pe}/σ_K as a function of element atomic number. The code determines element ratios by quadratic interpolation of the Table 1 data. Fluorescent yield data as a function of atomic number, reproduced from reference (19), are given in Figure 7 and Table 2. The code obtains F_B from the Table 2 data by quadratic interpolation.

The code initiates K series x-rays at the n^{th} interaction site with a weight W_m, which is shared by the $K\alpha_1$, $K\alpha_2$, $K\beta_1$, etc. in accord with relative intensities given in Table 3 (and input by the user). The code initiates K series x-rays in the same random isotropically selected direction with energies corresponding to the difference in the K and L or M shell energy levels$^{(20-22)}$. Intensity and energy data reproduced from reference (20) are given in Table 3.

The code assigns a zero probability of x-ray escape for those interaction sites located at greater than a critical distance, $d = 4.6\lambda\ (E\alpha_1)$ from the transport medium bounding surface. For interaction sites located at less than the critical distance from the medium boundary, escape or absorption is determined by comparing the Monte Carlo path length obtained from Equation (2) with the vector distance to the boundary.

2.5 Scintillation Detector Response

Code NUGAM3 determines the response of a scintillation crystal to incident gamma photons according to the Monte Carlo technique. The crystal may be encased in a cladding material and backed by a hypothetical "photomultiplier" analogous to the experimental situation. Thus the code allows the transport medium to consist of three distinct submedia, namely:

I. front and side cladding
II. "photomultiplier"
III. scintillation crystal

The code may be used for the combinations: I and III, II and III or III only. A typical detector geometry is shown in Figure 8.

The source photons are followed from their entry into the detector until they escape from the detector. The energy deposited at each photon interaction within the crystal site is weighted and subtallied as absorbed energy. The weighted subtallies are stored as weighted counts in the appropriate energy bins or channels at the termination of each history, i.e. after either escape from the detector system or weight/energy cut-off termination.

A hypothetical photon history is shown schematically in Figure 9. In this example the main path, indicated by the solid lines, is characterized by four interactions followed by escape from the detector. Photon weight is reduced at each interaction by the ratio of scatter to total cross-section; photon energy is also reduced at each interaction in accord with the Compton scattering relationships (see Section 2.2). Since the photon energy prior to interactions 1 and 2 exceeds 2.0 mc^2, the pair production threshold energy, two pair of "back to back" 1.0 mc^2 photon histories are initiated as indicated by the dashed lines. In the figure the photon weights and energies (in parentheses) are shown before and after each collision. For example, it is noted that the main history initial energy and weight are 8.0 mc^2 and 1.0, respectively; the final (escape) values are 0.5 mc^2 and 0.1, respectively.

The NUGAM3 code follows both main and annihilation histories; in the Figure 9 example five histories are followed. Figure 10 demonstrates the energy absorption and escape distribution corresponding to Figure 9. Figure 10(a) corresponds to the main history and Figures 10(b) and 10(c) correspond to the two pair of annihilation photon histories. Energy distribution matrices corresponding to Figure 10 are given in Table 4, 5 and 6.

The energy absorption termination distribution for the example is given in Figure 11. The data for this figure, as tabulated in Table 7, is obtained from the "weights" and "absorptions per photon" given in Tables 4, 5 and 6. The "absorption per photon" data of Table 5 is 6 mc^2 larger in Table 7 to account for pair electron energy deposition in the crystal. There is no electron energy addition for the second interaction since it occurs in the "photomultiplier". Table 7 data of the same energy has been "grouped" for plotting in Figure 11.

The NUGAM3 code tallies each history as in Figure 11. The result for a large number of histories is a spectrum of scintillation crystal absorbed energy. The solid points in Figure 12 present the Monte Carlo absorbed energy spectrum for a 3" x 3" NaI (Tℓ) crystal as determined by NUGAM3; the source energy in this example is 2.615 MeV. The solid points in Figure 12 would be the final useful result if experimental scintillators responded discretely to absorbed energy deposition. However, since the response is not unique but is instead spread out (smeared) over a range of pulse-heights, a"line-broadening" operation is necessary for simulation of the experimental spectrum. The line distribution in Figure 12 represents the "line-broadened" spectrum; it is discussed below.

Experimentally it is an observed and fortunate fact that the "line-broadening" in scintillators is approximately a normal, i.e., Gaussian, distribution(23). It has been found empirically that the standard deviation of the Gaussian, though not constant with energy, has a systematic dependence. In the NUGAM3 code the Gaussian standard deviation $\sigma(E)$ is computed from the relationship(24,25).

$$\sigma(E) = kE^n \quad , \tag{27}$$

where

> k and n are determined by fitting the photopeaks of standard source spectra with Gaussians (k and n are the intercept and slope in a log-lot plot of $\sigma(E)$).

The NUGAM3 code redistributes the $j = 1$ to m channel elements of the Monte Carlo absorbed energy spectrum $M(E_j)$, over $i = 1$ to n channels, according to the Gaussian relationship (defined in reference (26))

$$g_{ij} = \frac{(2\pi)^{-\frac{1}{2}} M(E_j)}{\sigma(E_j)} \exp\left(-1/2\left[\frac{E_j - E_i}{\sigma(E_j)}\right]^2\right) \quad , \tag{28}$$

The final Gaussian broadened spectrum is obtained from the summation of the m spectra as

$$G_i = \sum_{j=1}^{m} g_{ij} \text{ ; } i = 1, n. \tag{29}$$

In equations (28) and (29) E_i and E_j are the energies at the channel mid-points. In the event that the standard deviation $\sigma(E)$ is small relative to the selected constant channel width, $\Delta V = E_m/m$, the code determines the Gaussian in each i^{th} channel as a histogram i.e. Equation (28) is integrated over each channel from $V-0.5\Delta V$ to $V+0.5\Delta V$(27). The distribution in Figure 12 is the Gaussian smoothed absorbed energy spectrum corresponding to the solid points.

In addition to determining the Monte Carlo absorption and Gaussian smeared spectra the code also calculates the detector photofraction(28), P(E) and efficiency, $\epsilon(E)$, according to the relationships

$$P(E) = \frac{\text{Full Energy Absorption Counts}}{\text{Total Counts}}, \tag{30}$$

and

$$\epsilon(E) = \frac{\text{Total Counts}}{\text{Number of Detector Incident Photons}}. \tag{31}$$

The "number of detector incident photons" is defined by the frontal cladding, i.e., a lesser number are defined by the crystal front face for obvious geometrical reasons.

3. DISCUSSION OF RESULTS

3.1 Introduction

In this report section, results obtained with the NUGAM2 and NUGAM3 codes are presented and discussed. The NUGAM2 code was used to obtain gamma photon buildup, albedo, finite source self-absorption and finite source emission data. The NUGAM3 code was used to determine NaI(Tℓ) scintillation detector response function data. The NUGAM3 code was also used to obtain encapsulated source self-absorption and emission data.

Buildup factor and albedo distributions were determined for gamma photons incident on finite laminar shields using the Monte Carlo technique. Angular energy differential and integrated number, energy and exposure distributions *were obtained as a function of angle and energy* (0.5 to 6.0 MeV) *of incidence* as well as dimensions of the medium. The buildup factors for single medium composition are in good agreement with the published theoretical(29,30) and experimental data(31). The albedo data for single media are in similar good agreement with published data(32-43). The albedo data is presented in Section 3.2. The buildup data is presented in Section 3.3. The source self-absorption and emission data is given in Section 3.4.

NaI(Tℓ) experimental pulse-height response functions were numerically simulated using the NUGAM3 code. The analysis was carried out for right-cylindrical NaI crystals encased in typical side and front cladding material and rear-mounted on a material typifying a photomultiplier assembly. The results are for exposure of the encased detector to isotropic point sources of gamma photons in the energy range up to 4.45 MeV; parallel beam photon incidence was also investigated. The results obtained were: crystal energy deposition and Gaussian-smeared pulse-height response distributions; photofractions; interaction efficiencies and detector angular-energy differential escape distributions. The importance of single and double scatter effects was also investigated. The results for a "bare" crystal are in excellent agreement with the data of reference (44). The results for the clad crystal simulate the experimental data of reference (23) with very good agreement.

3.2 Albedo Results

The NUGAM2 code determines gamma photon albedo data as a function of photon angle of incidence and energy, material atomic number and composition, laminar disposition, material lateral dimension and thickness, and incident radiation beam geometry such as parallel beam, point source, etc.

The number of gamma photons backscattered as a function of the transport medium total thickness L and within an escape category radius d located on the transport medium backscatter plane, as in Figure 13, were determined to ascertain the limitations of the albedo technique. Total number albedos for 0.662 and 1.25 MeV normal photon incidence are given in Figures 14 and 15 as a function of both L (open points) and d (solid points), in units of mean free path λ (E), with transport medium atomic number Z as a parameter. The arrows on the right hand ordinate of the figures indicate comparison data from the references (33-43). For Z = 13 the number albedo reaches a saturation value at $d = d_\infty < 0.25\ \lambda$ for both 0.662 and 1.25 MeV. As the figures indicate, approximately half of the backscattered photons emerge within a characteristic distance, $d = d_{\frac{1}{2}}$, typical values of which are given in Table 8 in units of

λ (E). Analogous half and saturation thicknesses $L_{\frac{1}{2}}$ and L_∞ were observed to be approximately 85% of the $d_{\frac{1}{2}}$ and d_∞ values. The total number albedos may be approximated as a function of either d or L, by the exponential relationship form reported by others. (45, 46) The saturation total number, energy and exposure albedos were found to be in excellent agreement with the published Monte Carlo data and in good agreement with the experimental data.

Figure 16 gives total number and exposure albedo distributions for normally incident 1.0 MeV photons as a function of lamination thickness and composition, for L = 1λ, 2λ, and 4λ. The number (open points) and exposure (solid points) albedo are seen to vary over the entire lamination thickness fraction range for Al - Pb and Al - Fe. The lamination order in the figure is source - Al - Fe (or Pb). For example, the total number albedo for 1.0 MeV photons is 0.08 for 1λ aluminum 'backed' by 3λ of Pb (thickness fraction = 0.25/0.75); 1λ Al = 6.034 cm, 3λ Pb = 3.865 cm, L = 4λ = 9.899 cm.

Figure 17 gives the total number albedo distributions for normally 'incident' 1.0 MeV photons and a medium thickness L = 4λ as a function of lamination arrangement order, e.g., Al - Pb and Pb - Al. The albedo example in the last paragraph reduces to 0.01 if 1λ Pb is 'backed' by 3λ Al. In fact it can be seen that the albedo is that of Pb only until the Pb thickness is reduced to less than 0.25λ. The same behavior is evident for the Al - Fe and Fe - Al data.

Figure 18 shows the code calculated total number albedo as a function of normally incident photon energy, with atomic number as the parameter. Calculations were not carried out above 6.0 MeV since the code does not account for bremsstrahlung generation which will be significant at higher energies. Similarly the Pb data in the figure does not account for fluorescent radiation backward emission; this is significant for high Z as indicated in the references (33, 34).

Figure 19 gives examples of the total number albedo as a function of the angle of incidence θo; θo is measured with respect to the outward normal of the scattering medium. For the sake of the expected albedo at $\theta o = 90^{\circ}$, the albedos in this figure are multiplied by $\cos\theta o$. The increasing albedo with increasing angle θo is very evident in the figure for Z = 82, even though it does occur for Z = 13. The dependence on energy is also noticeable.

Figure 20 shows the ratio of the 'single scatter' to 'total scatter' for the total number albedo, as a function of energy. The ratio α_{Nss}/α_{NT} is plotted as a function of E_o, with atomic number as a parameter. Typical single and double scatter to total number albedo ratios α_{ss} and α_{ds}, are given in Table 9. It can be seen that multiple (>2) scattering in lead accounts for only $\lesssim$ 1% of the number albedo at $E \leq 0.662$ MeV. However, even for 0.412 MeV photons incident on aluminum, multiple scatter accounts for ~ 50% or more of the total number albedo. The Monte Carlo single scattering data were substantiated by a double numerical integration of the analytic differential transport equation, indicating that albedos for high Z media may be readily approximated by this method. The analytic transport equation used in this evaluation was defined, with reference to Figure 21, as

$$\alpha_{Nss} = 2\pi r_e^2 N_e \int_0^L e^{-\mu_o z} \int_{\theta=0}^{\theta_{max}} \sigma(\theta, E_o)\, e^{-\mu_s z/\cos\theta} \sin\theta d\theta \ dz, \quad (32)$$

where

r_e = classical electron radius,

= 2.8183×10^{-3} (cm),(26)

N_e = number of electrons/cm^3,

$\sigma(\theta, E_o)$ = Klein-Nishina function (cm^2/ster.-electron),(26)

μ_o = total cross-section for E_o (cm^{-1}),

μ_s = total cross-section for E_s (cm^{-1}),

E_o = incident photon energy (MeV),

$$E_s = \frac{E_o}{1 + (E_o/0.511)(1-\cos\theta_s)} \; ; \theta_s = \pi - \theta, \text{ (MeV)}.$$

Table 10 presents a comparison of Al, Fe, Sn and Pb analytic (Equation (32)) and NUGAM2 Monte Carlo single scatter albedos for different values of thickness L, escape category radius d and energy E (0.662 and 1.25 MeV). The agreement can be seen to be very good for low atomic number and as poor as 15% "error" for high atomic number. The deviation expresses to a large extent, the statistical error in the Monte Carlo data. The analytic equation was encoded and solved using Simpson's Rule in a separate computer code: SSALB. Code SSALB is detailed and listed in Appendix VI of Volume II of this report.

Code SSALB is considered as the basis of a very useful engineering code for radiation backscatter analysis. For example, Table 10 indicates $(\alpha_{N_{ss}})$ anal. = 0.0656 for Z = 13 and E_o = 0.662. Table 9 gives R_{ss} = 0.24, thus using the analytic single scatter albedo the total albedo may be estimated as $\alpha_N = (0.0656/0.24) = 0.274$, which is in very good agreement with 0.26 in Figure 14. This approach based on Monte Carlo data, offers an economical method for engineering analysis.

3.3 Buildup Results

The NUGAM2 code determines gamma photon buildup distributions as a function of photon angle of incidence and energy, material atomic number and composition, laminar disposition, material lateral dimension and thickness, and incident radiation beam geometry.

The energy penetration buildup of 1.0 MeV photons incident on aluminum, iron and lead media, as a function thickness, is compared directly in Figure 22 with the data of reference (29) and indirectly with reference (30). The reference (29) data which in turn compares well with the reference (30) data is indicated by the solid line curves while the NUGAM2 data is given by the points. The reference (29) data was determined by the Monte Carlo method as applied to semi-infinite media. The NUGAM2 data was determined for finite media of "large" lateral extent. The agreement is seen to be very good. NUGAM2 data for aluminum is compared with reference data for ordinary concrete.

For normal axial incidence it was observed that ~ 99% of the transmitted scattered photons emerged from the transport medium within a characteristic radial distance d_∞ approximately equal to the shield thickness. Figure 23 gives photon number penetration buildup factors for $L = 0.5\lambda$, 1λ, 2λ, 4λ and 6λ as function of radial distance d (in units of $\lambda(E)$) from the axis of a cylindrical tin shield axially exposed to 0.5 (open points) and 2.0 (solid points) MeV photons. The figure indicates that photon emergence from a shield is 'negligible' at perpendicular distances >3λ from a normally incident axial photon beam. Figure 24 gives photon number penetration buildup factors for L = 2λ and 4λ as a function of d for H_2O, Al, Fe, Sn and Pb exposed to 2.0 MeV photons. The behavior is seen to be similar to that given in Figure 23 for tin.

Number and energy buildup factors for photons of 1.0 MeV, normally incident, on shields of thickness L = 4λ and 6λ, are given in Figure 25 as a function of lamination thickness for Al - Pb, Pb - Al and Al - Fe. The distributions in this figure are in agreement with qualitative arguments based on the photoelectric effect and Compton scattering. The energy buildup factors are less sensitive than the number buildup factors to the shield geometry and composition, especially when the media are relatively proximate in atomic number as in the case of Al - Fe. The Al - Pb data indicates that a laminar shield of 3λ aluminum, backed by 1λ lead, has energy and number buildup approximately equivalent to a shield of 100% lead.

Figure 26 gives the energy spectrum of scattered photons penetrating Pb - Al shields of thickness L = 4λ as a function of the lamination fraction for 2.0 MeV incident photons; the unscattered penetrating photons are not shown. The all Al shield exhibits a low energy 'buildup' whereas the all Pb shield exhibits a low energy 'depletion,' which is in agreement with qualitative considerations. The effect of reverse lamination order is seen in Figure 27 where the spectra of Pb - Al and Al - Pb are shown; shield total thickness and lamination thickness fractions are the same. Figure 27 shows that the buildup is a minimum when low Z is 'backed' by high Z material; the high Z acts as a 'catcher' for low Z scattered photons. The spectra of Figures 26 and 27 are consistent with experimental spectra of reference (31).

3.4 Source Self-Absorption and Emission

The NUGAM2 code determines gamma photon self-absorption and emission from either cylindrical or rectangular finite source geometries. Initial isotropic source distributions may be specified either as either'at a point' or uniformly distributed. The present version of NUGAM2 allows the source to be in one lamination of the laminar geometry, and thus unclad "sidewise". A NUGAM3 option allows the substitution of a source medium for the NaI(Tℓ) crystal medium and further allows the substitution of source encasement for the normally used crystal cladding and photomultiplier. Thus, NUGAM3 may be used for encased source predictions.

Figure 28presents predicted unscattered and scattered photon number fractions emitted into 4π steradians for a 2 x 2 in. samarium-oxide cylindrical source of density 1.5 gm/cm^3, as a function of source energy. The figure also gives the unscattered fraction for a 1 x 1 in. source; the scattered fraction is omitted since it lies close to that given for the 2 x 2 in. source. The effect of the samarium K-electron absorption edge at 46.8 keV is evident for both sources.

Figure 29presents unscattered and scattered photon number fractions for escape into 4π steradians as a function of source size for selected source energies and materials. For a 0.5 MeV photon source homogeneously distributed within an 8 x 8 cm aluminum cylinder, it is seen that the fraction of scattered escapes approaches that of unscattered escapes. The figure also shows that the scatterered fraction for aluminum is approaching a maximum. This maximum, followed by a gradual decrease, was observed at ~ 4 x 4 cm for the samarium example and is related to the 'quenching' effect of photoelectric absorption, which is increasingly pronounced with increasing atomic number and density. During the course of this work, the differential angular and energy variation of photon escape was obtained as a function of atomic number, transport medium density and cylinder height-to diameter ratio. Integral data was determined from the differential results.

3.5 Scintillation Crystal Results

The NUGAM3 code determines the pulse-height response distributions of a scintillation crystal exposed to a point source or a parallel beam of gamma photons. The code optionally allows the crystal to be clad and/or 'photomultiplier' mounted.

Table 11 gives photofractions and detection efficiencies determined by the NUGAM3 code for an unclad (u) (bare) and clad (c) (front and side cladding, and photomultiplier) 3" x 3" right cylindrical NaI(Tℓ) scintillation detector exposed to parallel incident photons in the energy range 0.32 to 2.754MeV; a 4" x 4" crystal is included for data comparison at 4.45 MeV. The calculations assumed 0.125" front and side cladding and a hypothetical "photomultiplier" composed of aluminum with a density of 2.0 g/cc; a 1.18 g/cm beryllium absorber was also assumed. The cladding dimensions and composition were taken as those of typical commercial detectors(47). Unclad Monte Carlo photofraction and efficiency data from references (44) and (48) are given in parentheses; clad Monte Carlo data has not been reported. The NUGAM3 and reference data can be seen to be in excellent agreement.

Figure 30 compares the NUGAM3 code Monte Carlo generated spectral response of a 3" x 3" NaI(Tℓ) scintillation detector response to 10 cm distant point sources of ^{51}Cr, ^{85}Sr and ^{22}Na, with the actual experimental response reported in reference (23). The solid-points are the Monte Carlo data and the line distributions are as obtained by graphically connecting the digital data of the reference. The Monte Carlo and experimental spectra were photopeak area and pulse-height normalized; pulse-height normalization was carried out by using the algorithm of reference (49). The reference (49) algorithm was also used to smoothen the Monte Carlo absorbed energy spectra prior to Gaussian smearing. The Monte Carlo data was 'smeared' using k and n values in Equation (27) based on a fit of reference (23) photopeaks. The NUGAM3 determination assumed 0.125" front and side cladding$^{(47)}$ and a hypothetical "photomultiplier" composed of aluminum with a density of 2.0 g/cc; the front cladding was faced with a 1.18 g/cm beryllium absorber.

As Figure 30 shows, the agreement between calculation and experiment is excellent for ^{85}Sr; very good for ^{22}Na except in the 1.275 MeV photopeak valley; and good for ^{51}Cr. The ^{22}Na valley discrepancy, although not large, may be removed by adjustment of the NUGAM3 'smearing' standard deviation $\sigma(E)$, given in Equation (27). The deviations in the ^{51}Cr Compton continuum are considered to be small and partly due to the statistics of the Monte Carlo determination. It is noted that other than normalization and smoothening no unusual effort was made to fit the calculations to the experimental data. Additionally some details of the experiment are not positively known.

Figure 31 shows the Gaussian 'smeared' effects of front and side cladding, and 'photomultiplier', as determined by the NUGAM3 code for E = 0.6616 MeV. Response A consists of the backscatter distribution for the photomultiplier. Responses B and C consist of side and front cladding distributions. The sum distribution of A + B + C is also given. Responses for A, B, and C correspond to the geometry of Figure 30. In order to determine if the trends of the distributions were real and since they were obtained from the difference of two distributions, i.e., 'with and without A or B or C,' an abnormally large thickness of cladding was investigated, namely: D and E in Figure 31. Responses D and E tend to confirm the general shapes of B and C. Additional photomultiplier dimension introduced only a negligible change in Response A, indicating that an 'infinite' 'photomultiplier' had been assumed.

Although the distributions of Figure 31 are for 0.6616 MeV photons the same general behavior was observed for the energy range 0.279 to 2.754 MeV. It was deduced that the photomultiplier backscatter effect is primarily an albedo spectrum which exhibits a 'single' scatter peak at an energy corresponding approximately to a photon scattering angle of $\sim 150^{\circ}$ to 170°. The side cladding effect is seen to be similarly an 'albedo' spectrum but with a broader and higher energy 'single' scattering peak since allowable scatter angles range from 0° to 180°. The frontal cladding effect is seen to be a distribution extending over almost the entire spectral energy range. Its contribution to the photopeak valley is apparent.

Figure 32 presents the clad and unclad (dashed distribution) spectral response of a clad and unclad 3" x 3" NaI(Tℓ) detector exposed to a 10 cm distant point source of 2.615 MeV gamma photons. The single and double escape peaks are seen in both spectra but the 0.51 MeV annihillation distribution is only evident in the 'clad' spectrum. This is one very important feature of the NUGAM3 code over previous codes, namely that it calculates the 0.51 MeV distribution. In 'thickly' clad scintillations crystals such as are proposed for space flights this is of considerable importance.

Figure 33 presents the Monte Carlo calculated high energy portion of the Compton 'tail' on which the Gaussian photopeak 'sits,' as a function of source photon energy. The distributions are normalized to 50,000 source photons emitted in the solid angle subtended by the cladding of a 3" x 3" crystal; they are also pulse-height normalized to channel 100. Typical photopeak widths (at half-height) for 0.32 and 2.615 MeV would be ~ 10.0 and ~ 4.6 channels on the normalized scale of Figure 33, respectively.

Figure 34 presents photofractions as a function of side and front cladding thickness as determined by NUGAM3 for a 3" x 3" NaI(Tℓ) crystal exposed to a 10 cm distant point source of 0.662 MeV gamma photons. The behavior is consistent with spectra of Figure 31. The front cladding is seen to have a greater influence on photofraction than side cladding.

Figure 35 presents relative photofraction determined by NUGAM3 as a function of the collimation of a parallel beam incident on a clad 3" x 3" scintillation detector, for E = 0.662 and 1.25 MeV. Collimation is expressed in a ratio: (radius of collimation) ÷ (radius of crystal). Thus the ratio range is greater than 1.0 if the cladding is taken into account. The energy dependence is evident from the separation of the two distributions in the figure. The absolute photofractions corresponding to the relative photofractions at the axis and cladding surface are given. The distributions are in very good agreement with the data given in reference (50). However, it is noted that actual collimation devices will influence photcfractions to the extent that photons scattered in the collimator intercept the detector.

4. SUMMARY AND CONCLUSIONS

Five FORTRAN language digital computer code packages have been made operational on the NASA/GSFC IBM-360/91 digital computer. The codes are BREMRAD, NUGAM2, NUGAM3, SSALB, and 05S. The existing BREMRAD code was modified as described in the reference (3). The 05S code was obtained from the RSIC / ORNL and made operational at GSFC; it is described in the appendices to this report and the references (5, 6). The NUGAM2 and NUGAM3 codes were developed from the NUALGAM code, to which they now bear very little resemblance. The SSALB code was designed and developed to substantiate the NUGAM2 code. Because of their complexity and originality the largest part of the work scope effort was necessarily devoted to the NUGAM2 and NUGAM3 codes. The remainder of this section refers to the NUGAM2 and NUGAM3 codes.

The NUGAM2 code was developed to predict forward and backward angular energy differential and integrated distributions for gamma photons and fluorescent radiation emerging from finite laminar transport media. The code is thus designed to determine buildup and albedo data for scientific research and engineering purposes. The code is also designed to predict the emission characteristics of finite radioisotope sources. Asymptotically the code will predict data for 'large' (~ semi-infinite) transport media. It has been shown in this report that sample predicted data is in very good agreement with available published data. However, since the code predicts data for many situations in which no published data is available, it is concluded that it is a contribution to the field of radiation transport.

The NUGAM3 code was developed to predict the pulse height response of inorganic scintillation detectors to incident gamma photons. Because the code is designed to allow the scintillator to be clad and mounted on a 'photomultiplier' as in the experimental or industrial application, it is a more practical and thus useful code than others previously reported. It is shown in this report that the code's results are in excellent agreement with available published data. However, since the code predicts data for application in those situations where reported data is not available, it is concluded that it is a contribution to the field of radiation spectrometry.

Insofar as the NUGAM2 code is upper energy limited to the region of 5 to 6 MeV, it is proposed that its capability be extended to include bremsstrahlung generation resulting from electron production in the transport medium. Since the code does not employ deep penetration biasing techniques it is proposed that this be considered to allow its application to thick (greater than 6 to 8 mean free paths) transport media. Finally it is proposed that the code be used to develop engineering and scientific basic data for terrestrial and space application.

Although the NUGAM3 code was developed to encompass the radioisotope general energy range, up to ~ 4.5 MeV, it is proposed that it be extended to be useful up to ~ 10 MeV. This would allow it to be of considerable value in gamma photon astronomy and planetary spectrometry as well as for many terrestrial applications. It could be applied to determine complex detector responses where standard sources cannot be used. The proposed energy extensions require that the code be designed to consider electron escape and bremsstrahlung generation. Finally, it is proposed that the NUGAM3 code be used to develop a basic data library of response function distributions for scientific and industrial applications.

FIGURES

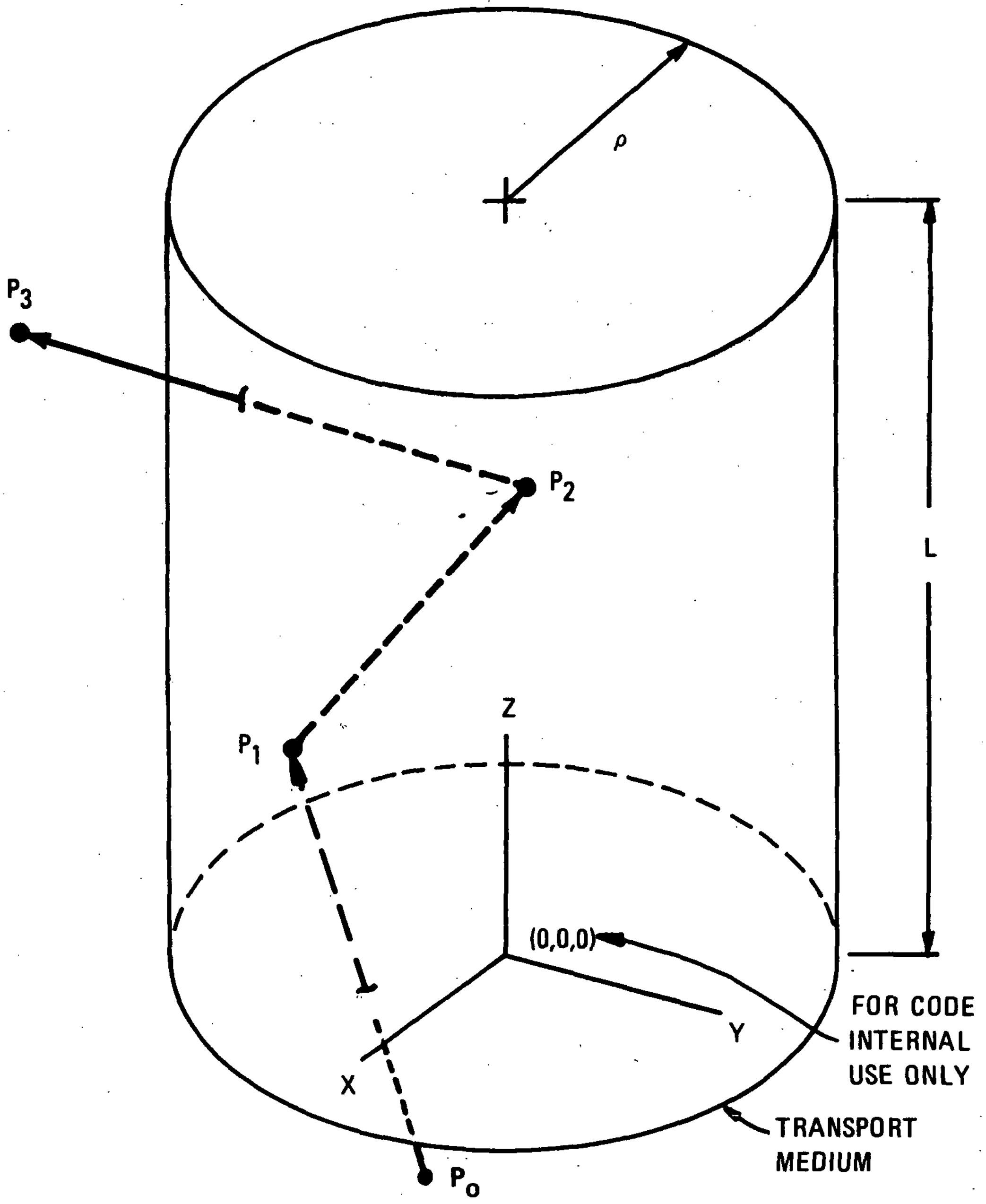

Figure 1

TYPICAL PHOTON HISTORY

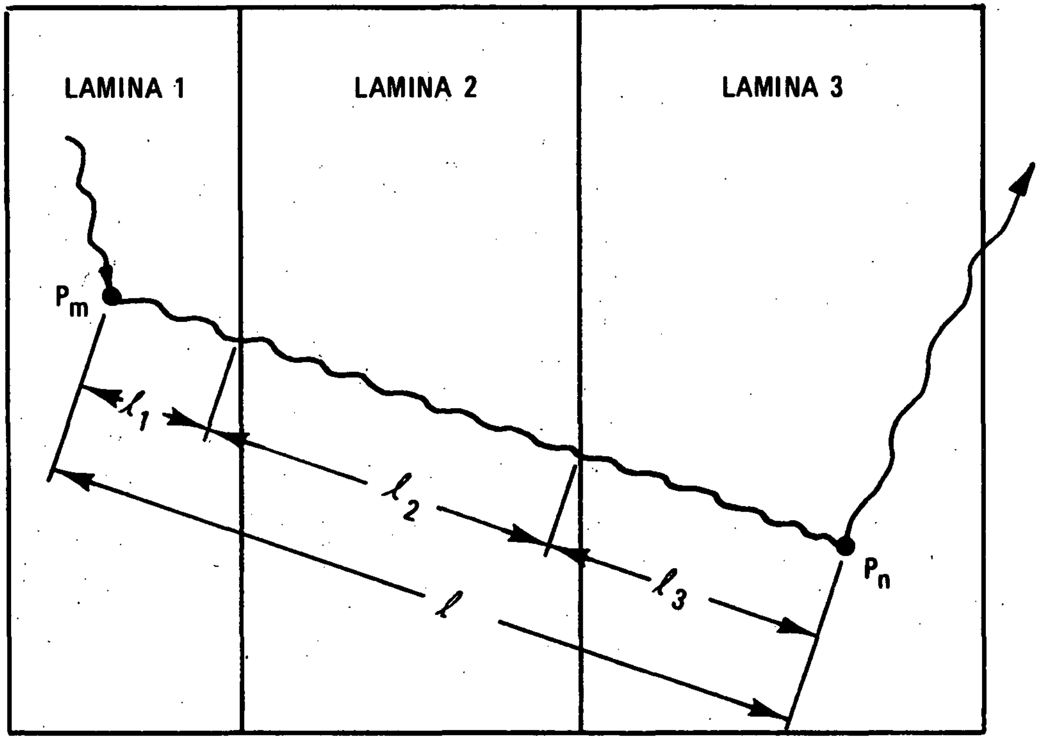

FIGURE 2
TYPICAL PHOTON TRAJECTORY BETWEEN INTERACTIONS
IN A LAMINAR GEOMETRY

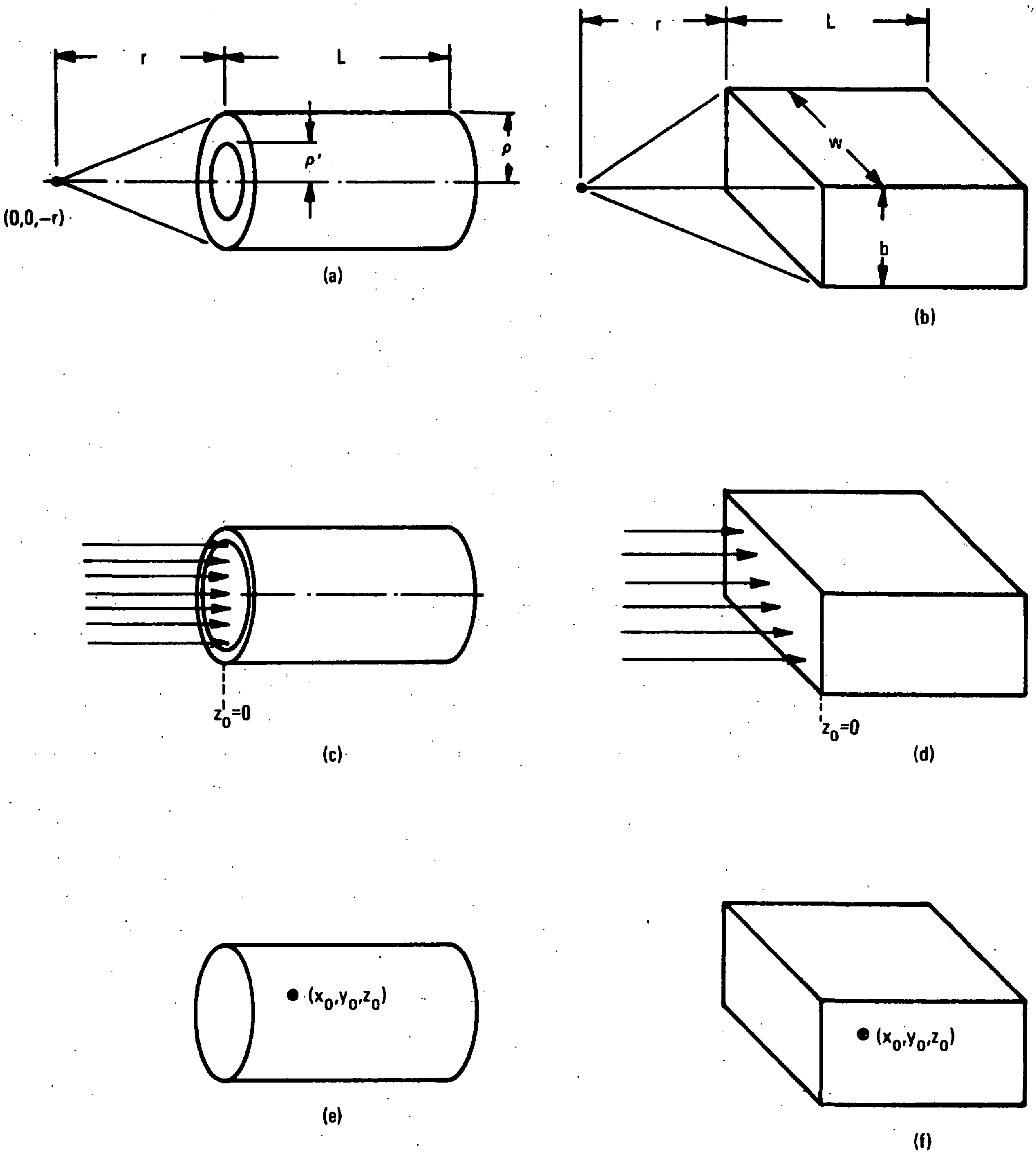

FIGURE 3
SCHEMATIC OF SOURCE AND TRANSPORT MEDIUM GEOMETRIES

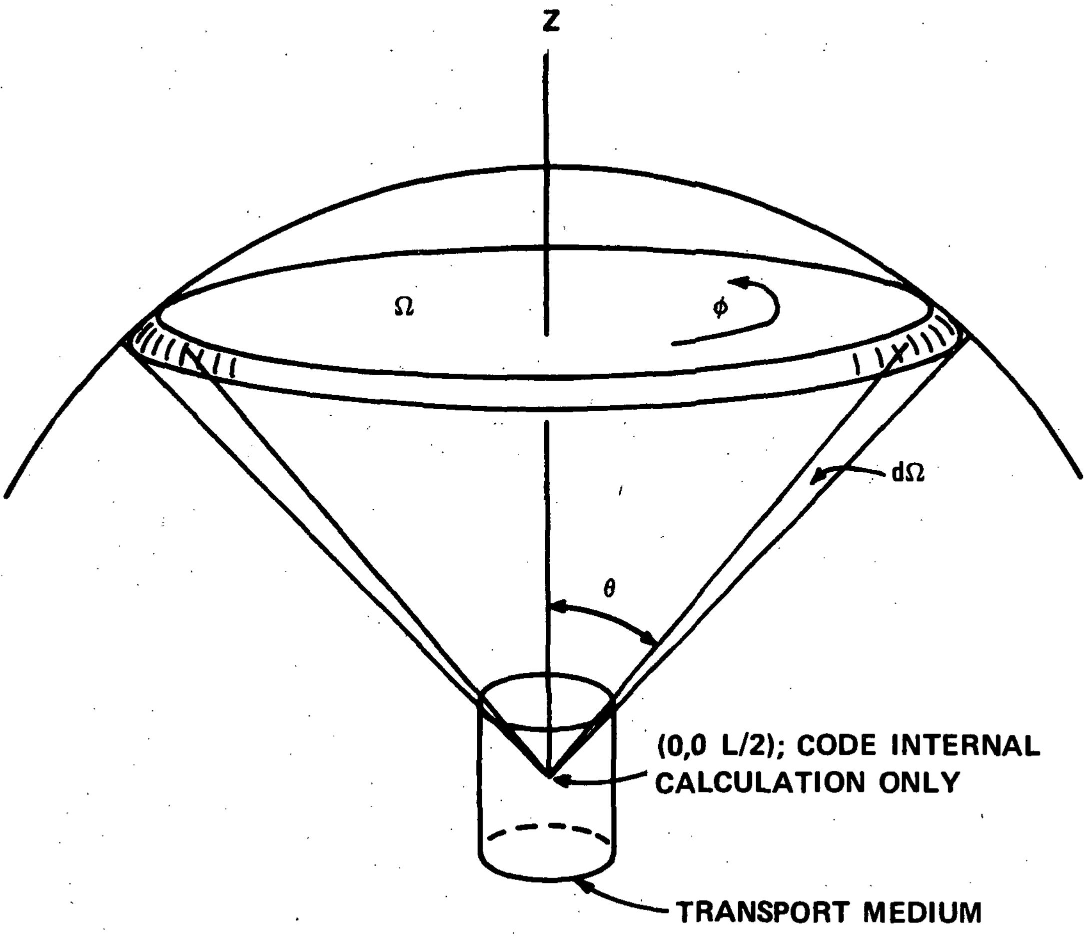

FIGURE 4

GEOMETRY OF PHOTON HISTORY ESCAPE CLASSIFICATION

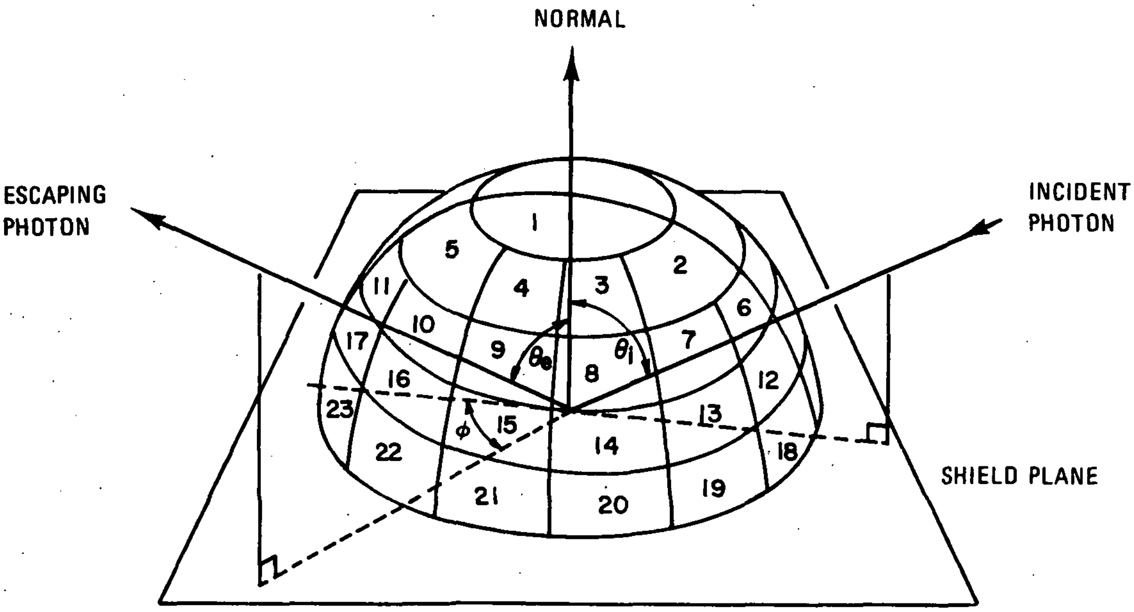

θ_i = ANGLE OF INCIDENT RAY WITH NORMAL

θ_e = ANGLE OF EMERGENT RAY WITH NORMAL

ϕ = ANGLE BETWEEN PROJECTIONS ON SHIELD PLANE OF INCIDENT AND EMERGENT RAYS

BACKSCATTER			FORWARDSCATTER		
SECTION NO.	$\pi-\theta_e$	Φ	SECTION NO.	$\pi-\theta_e$	Φ
1	165–180	0–180	24	75–90	0–30
2	145–165	0–60	25	75–90	30–60
3	145–165	60–90	26	75–90	60–90
4	145–165	90–120	27	75–90	90–120
5	145–165	120–180	28	75–90	120–150
6	125–145	0–30	29	75–90	150–180
7	125–145	30–60	30	55–75	0–30
8	125–145	60–90	31	55–75	30–60
9	125–145	90–120	32	55–75	60–90
10	125–146	120–150	33	55–75	90–120
11	125–145	150–180	34	55–75	120–150
12	105–125	0–30	35	55–75	150–180
13	105–125	30–60	36	35–55	0–30
14	105–125	60–90	37	35–55	30–60
15	105–125	90–120	38	35–55	60–90
16	105–125	120–150	39	35–55	90–120
17	105–125	150–180	40	35–55	120–150
18	90–105	0–30	41	35–55	150–180
19	90–105	30–60	42	15–35	0–60
20	90–105	60–90	43	15–35	60–90
21	90–105	90–120	44	15–35	90–120
22	90–105	120–150	45	15–35	120–180
23	90–105	150–180	46	0–15	0–180

FIGURE 5

SEGMENTATION OF HEMISPHERE FOR DEFINING DIRECTION OF FORWARD AND BACKWARD SCATTERING

NOTE: SEGMENTS 1 to 23 ARE FOR BACKSCATTERING AND SEGMENTS 24 to 46 ARE FOR FORWARD SCATTERING

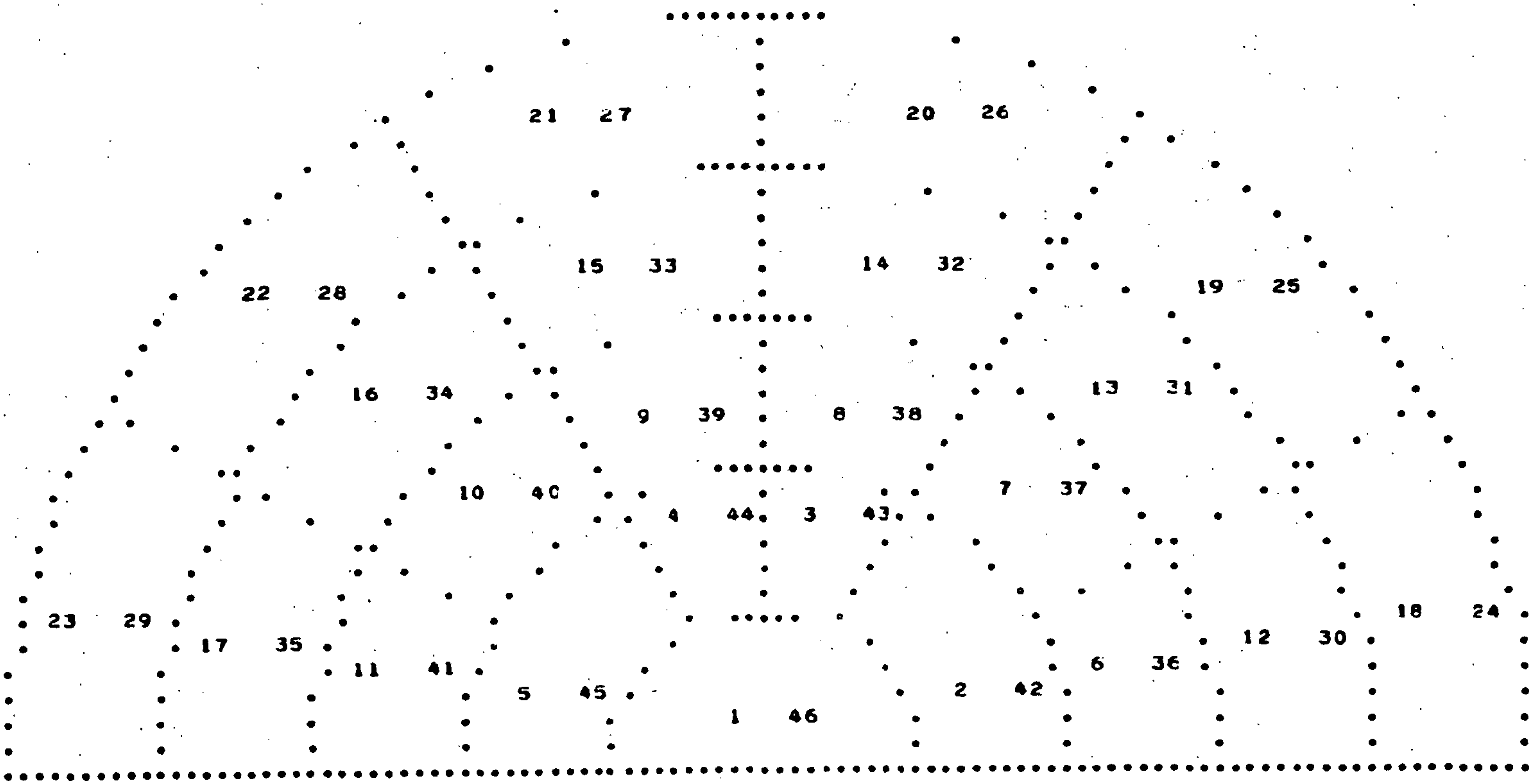

FIGURE 6
CODE SEGMENTATION MAP OF HEMISPHERE
FOR FORWARD AND BACKWARD SCATTERING

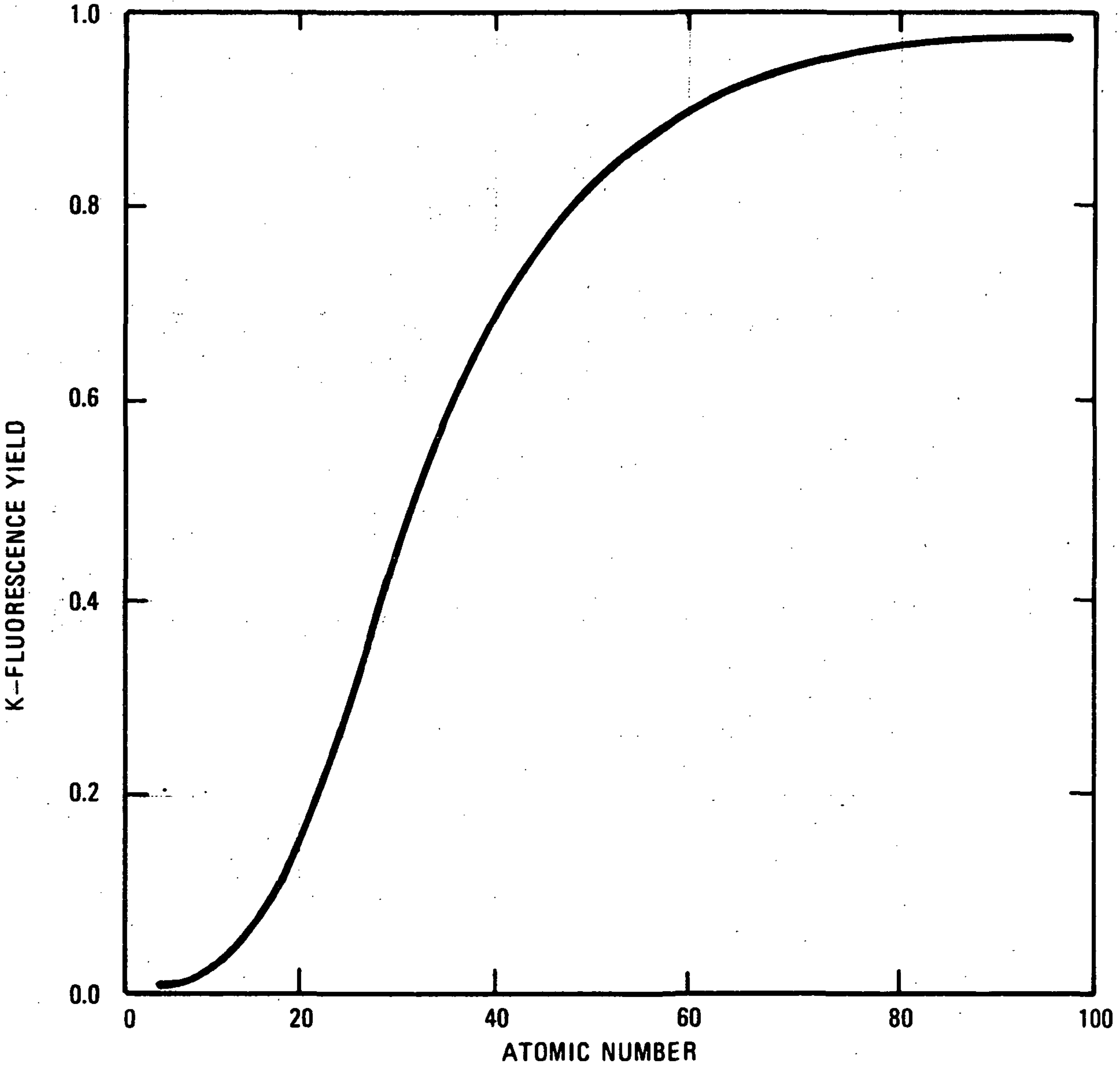

FIGURE 7
GRAPHICAL SUMMARY OF K–FLUORESCENCE YIELDS(19)

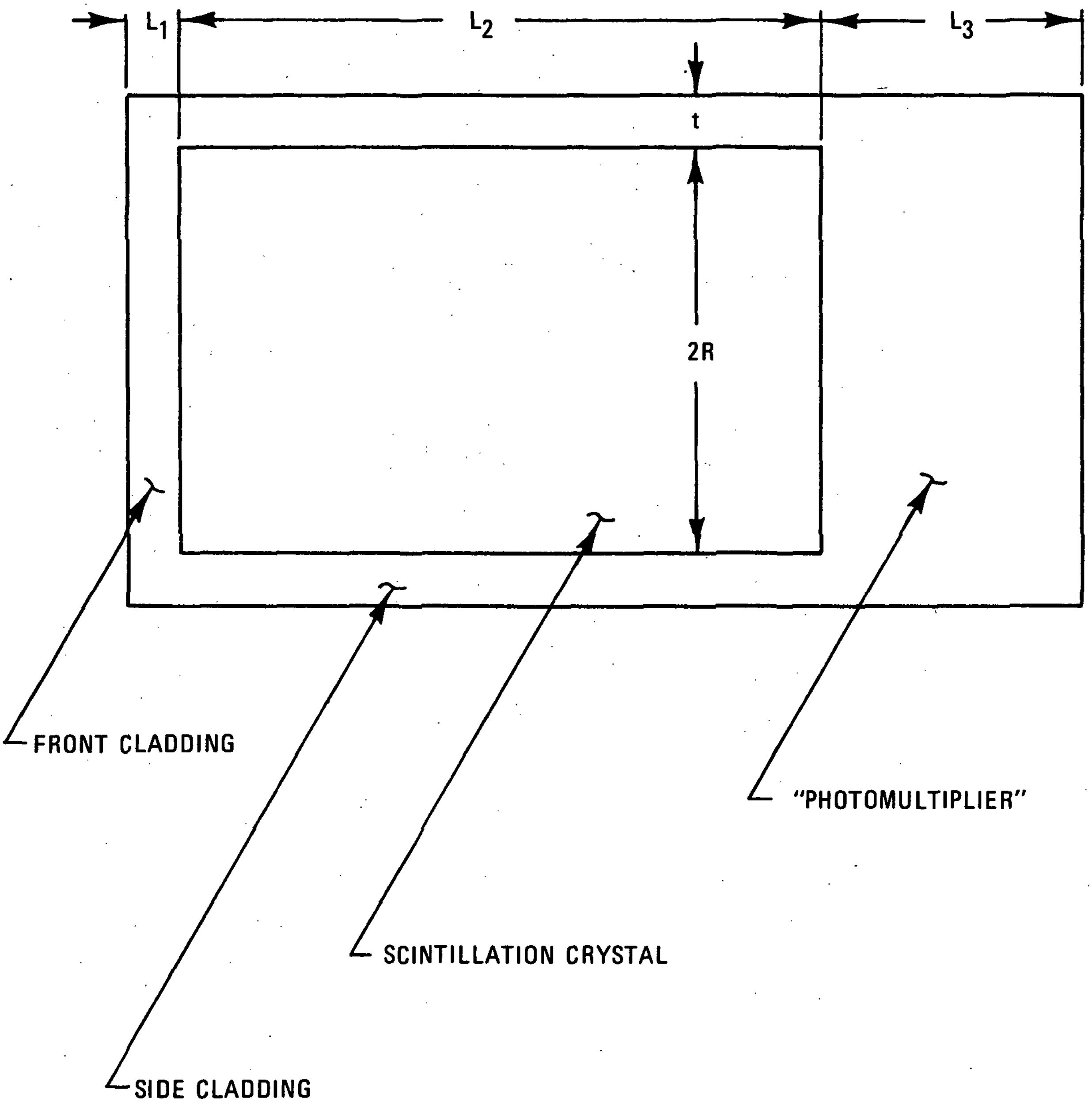

FIGURE 8
TYPICAL SCINTILLATION DETECTOR ARRANGEMENT

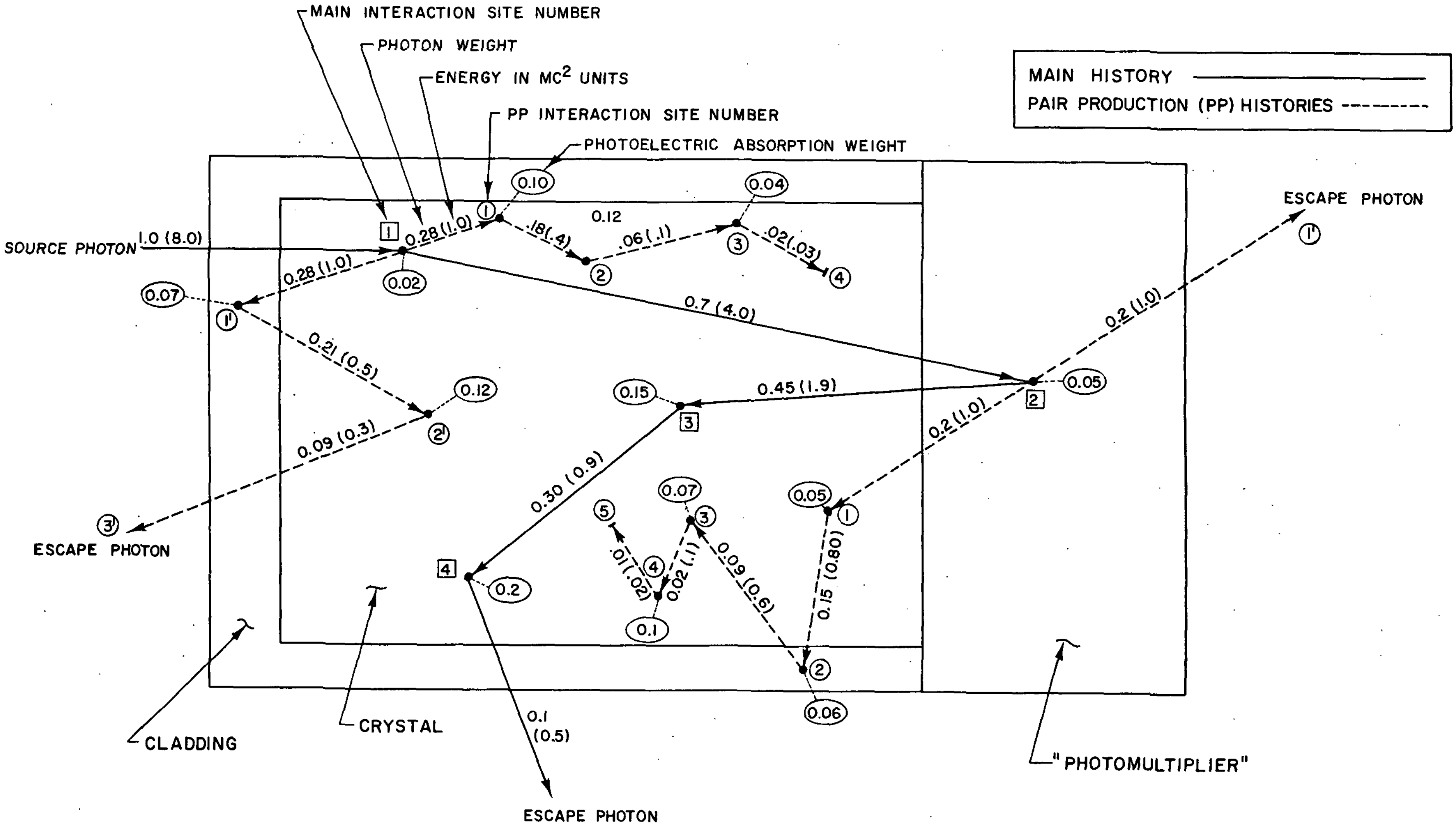

FIGURE 9

HYPOTHETICAL PHOTON HISTORY FOR
CLAD AND "PHOTOMULTIPLIER"- BACKED SCINTILLATION CRYSTAL

FIGURE 10
ENERGY DISTRIBUTION OF FIGURE 9 HYPOTHETICAL PHOTON HISTORY

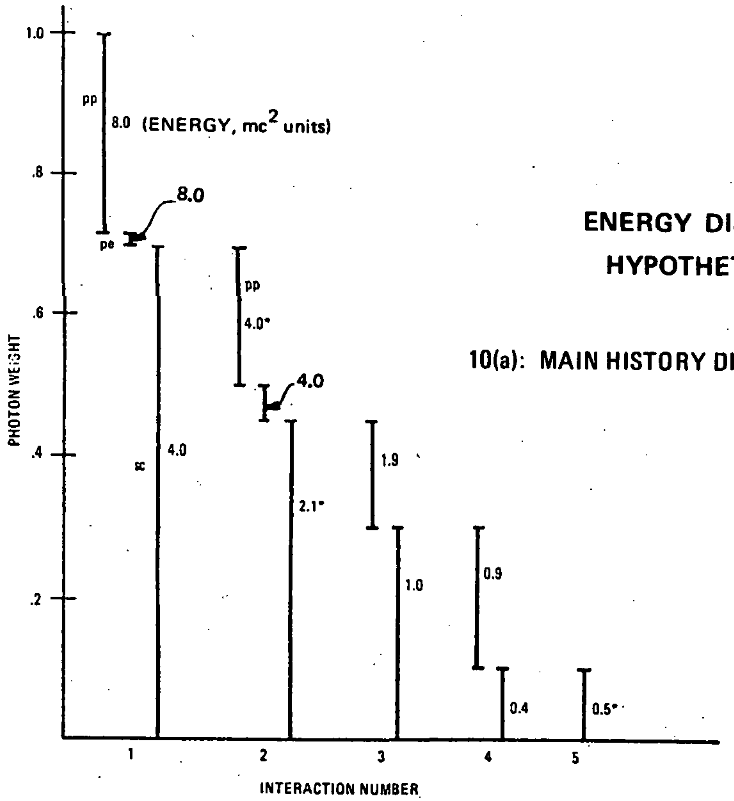

10(a): MAIN HISTORY DISTRIBUTION

NOTE: *ESCAPING ENERGY IS INDICATED BY ASTERISK (*)

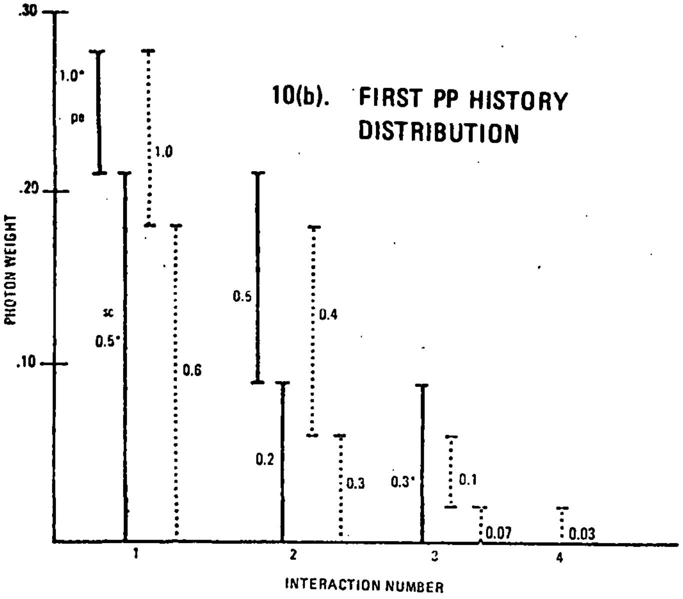

10(b). FIRST PP HISTORY DISTRIBUTION

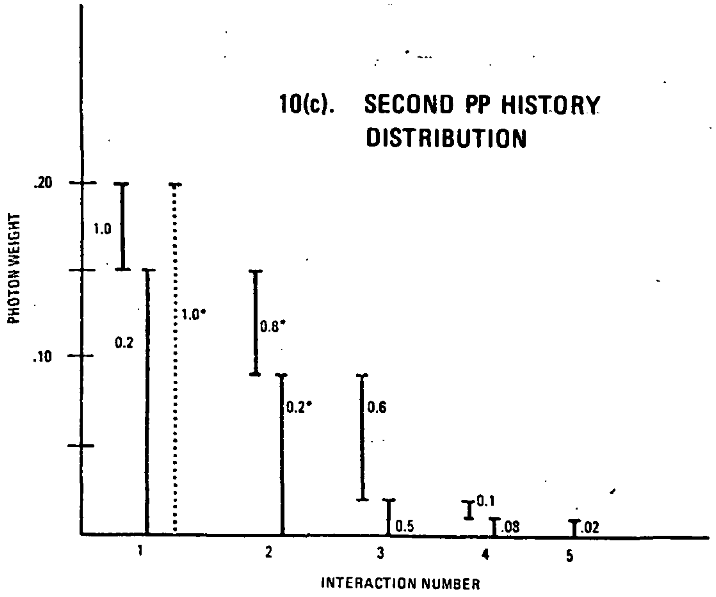

10(c). SECOND PP HISTORY DISTRIBUTION

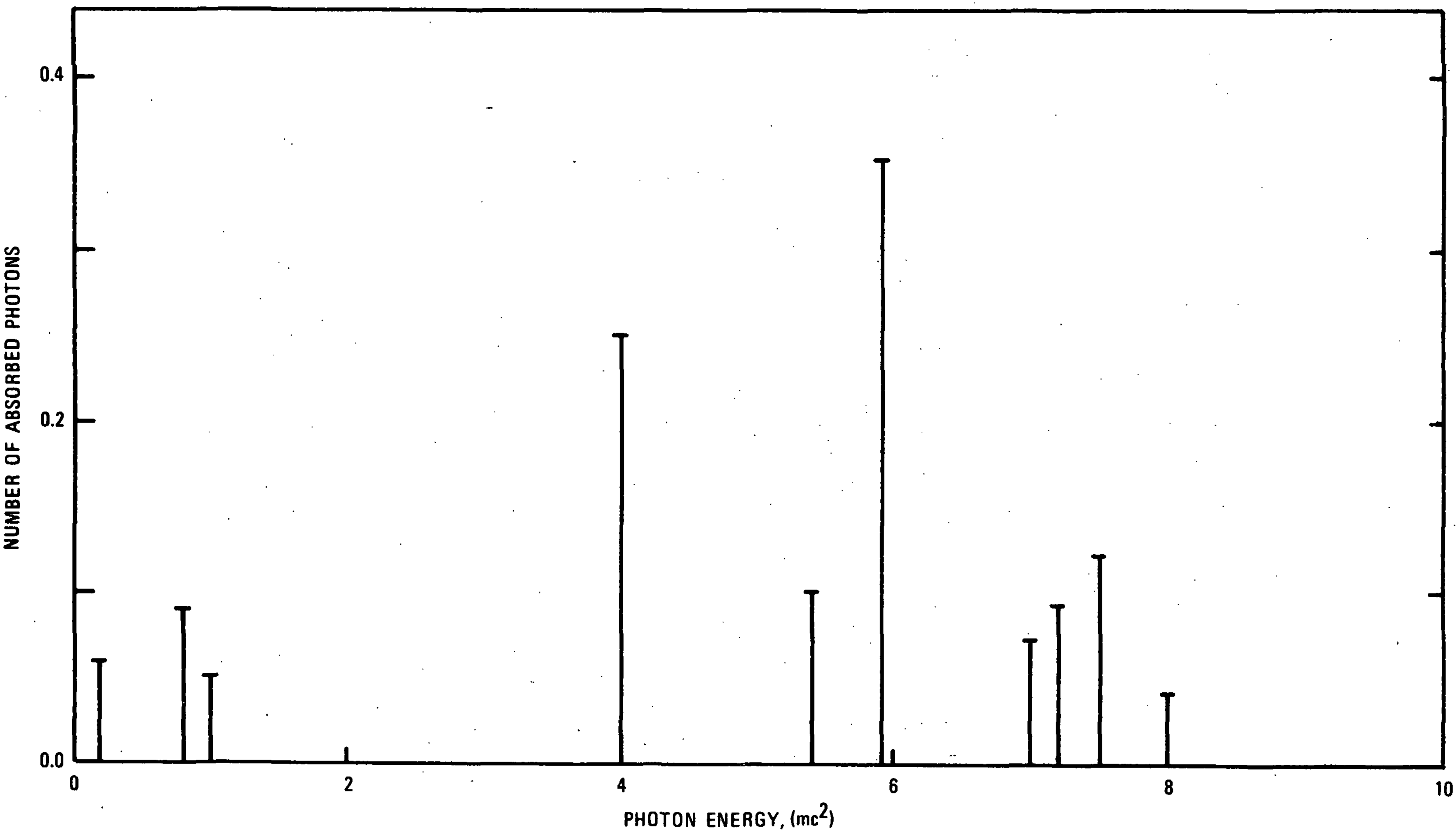

FIGURE 11
PHOTON ENERGY ABSORPTION TERMINATION DISTRIBUTION
CORRESPONDING TO FIGURE 9 HISTORY AND TABLE 7 DATA

FIGURE 12

COMPARISON OF MONTE CARLO ABSORBED ENERGY SPECTRUM AND GAUSSIAN "SMEARED" SPECTRUM FOR 2.615 MeV PHOTONS AND 3" X 3" CLAD NaI(Tl) CRYSTAL

NOTE: PHOTOPEAK NOT SHOWN
(PHOTOPEAK IN CHANNEL 100)

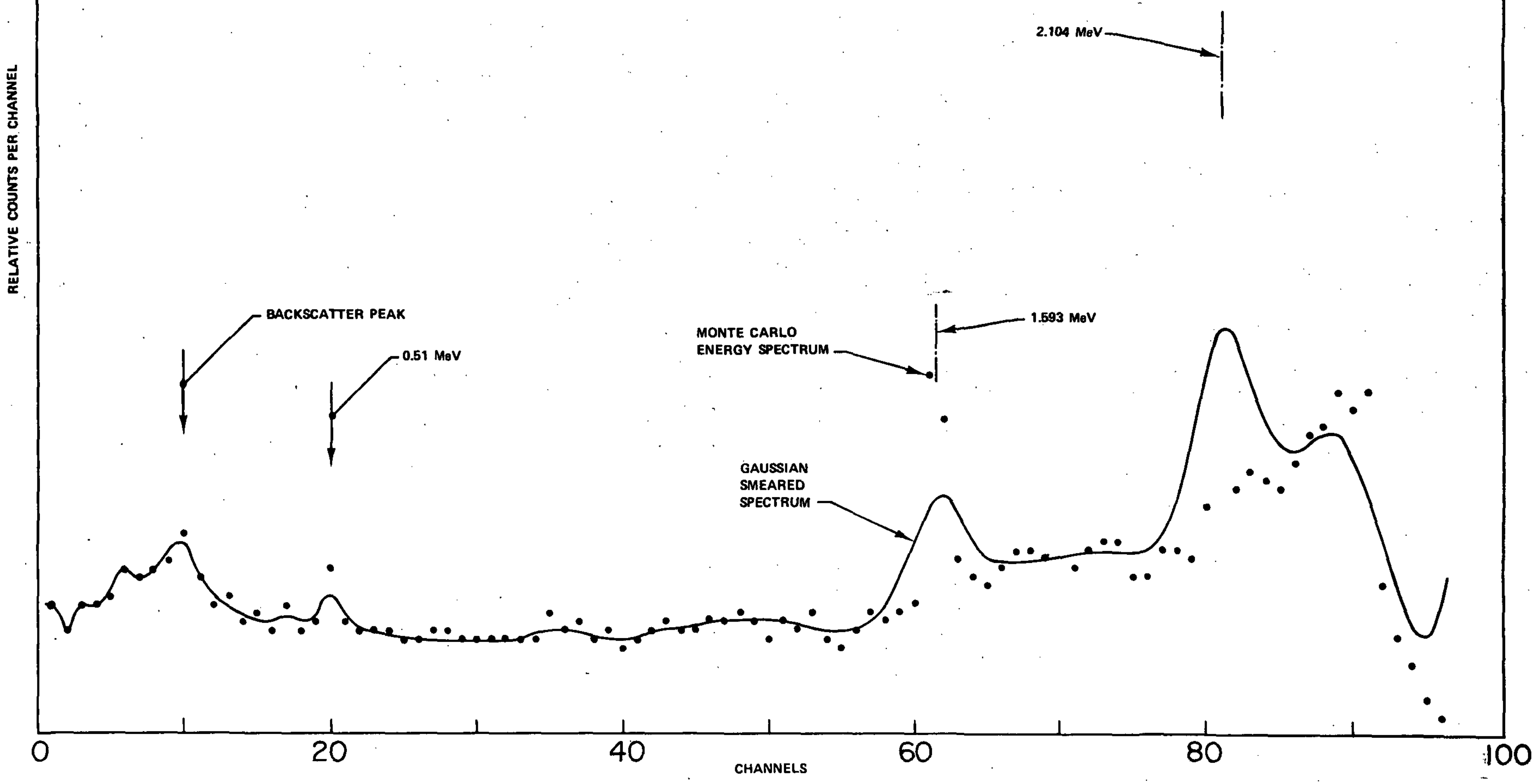

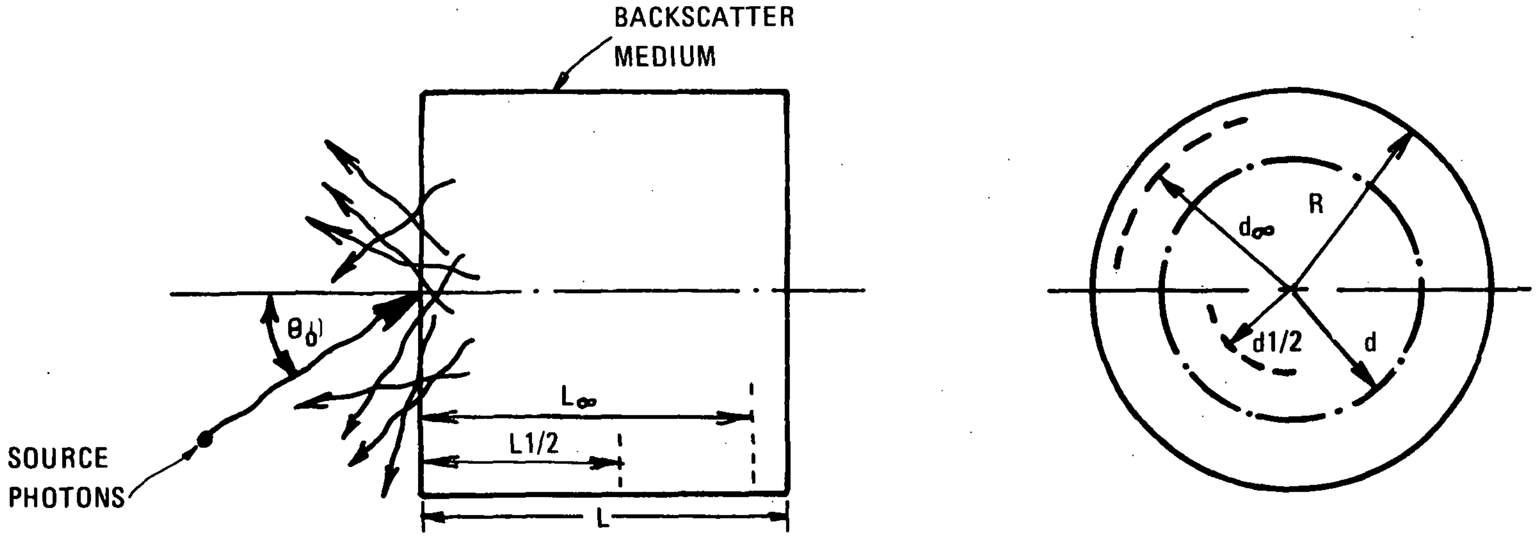

SIDE VIEW

FRONT VIEW

ALBEDO GEOMETRY

FIGURE 13

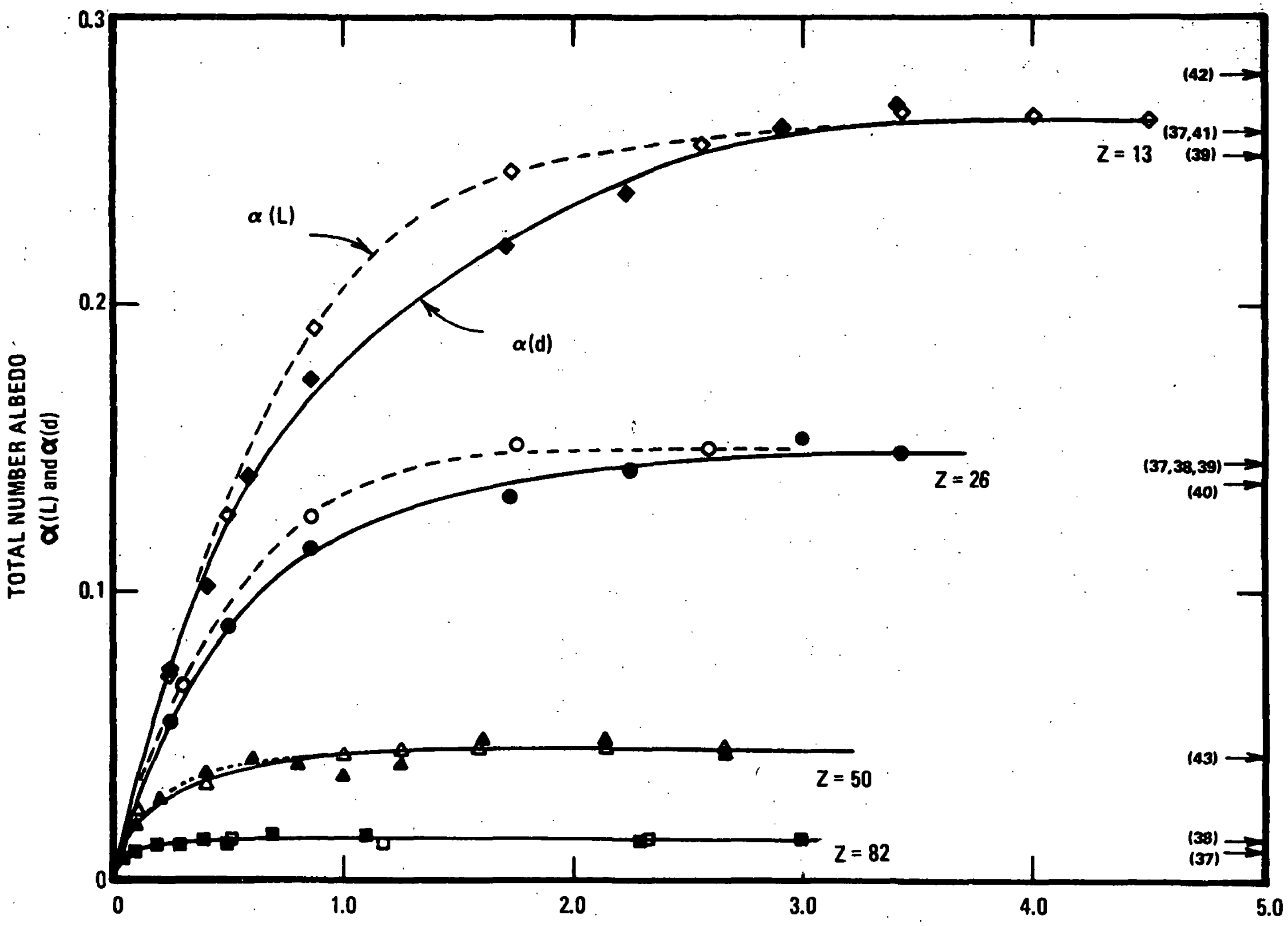

TOTAL NUMBER ALBEDO AS A FUNCTION OF L AND d
FOR E_o = 0.662 MeV AND NORMAL INCIDENCE
FIGURE 14

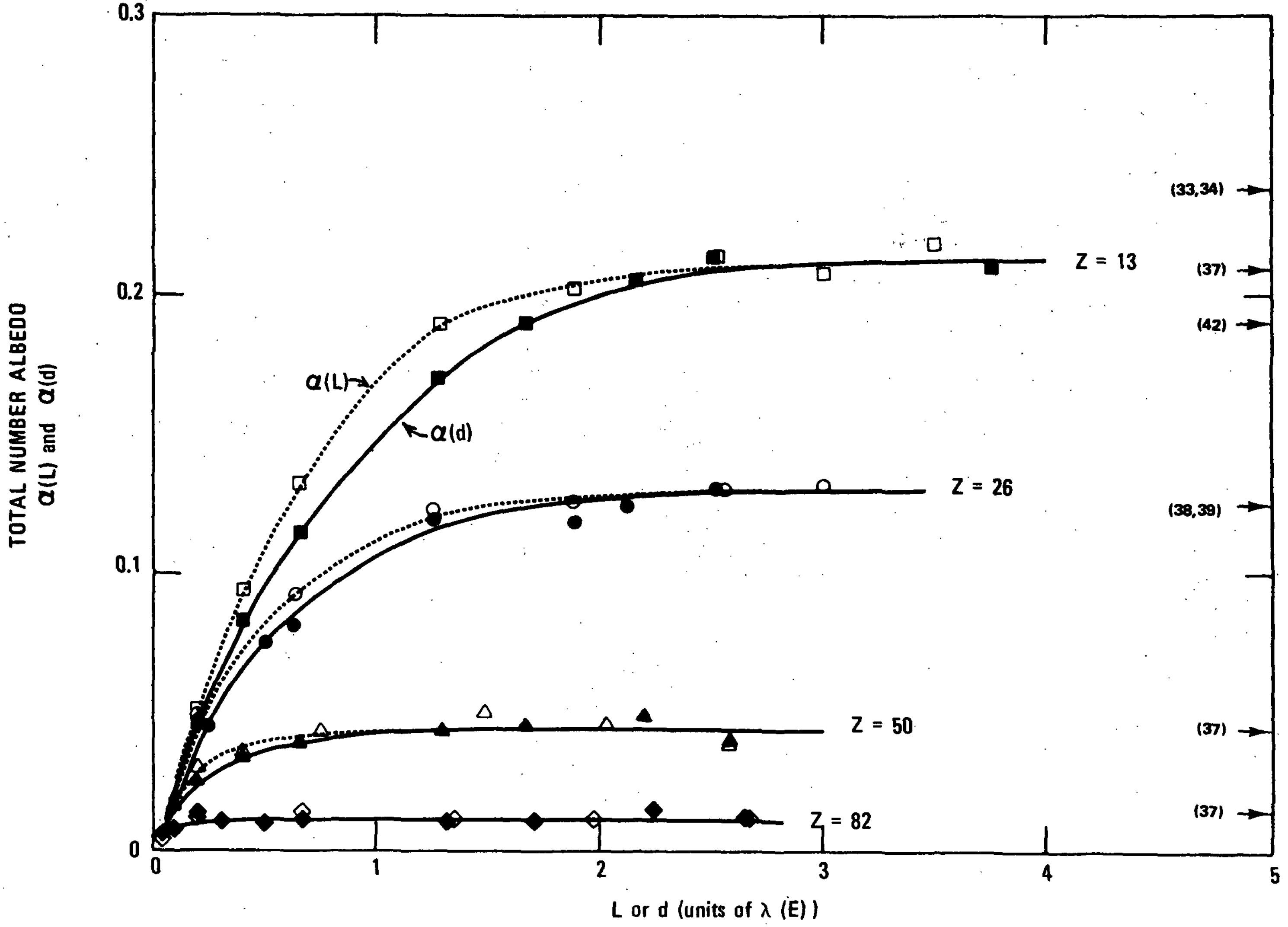

TOTAL NUMBER ALBEDO AS A
FUNCTION OF L and d FOR E = 1.25 MeV, and NORMAL INCIDENCE

FIGURE 15

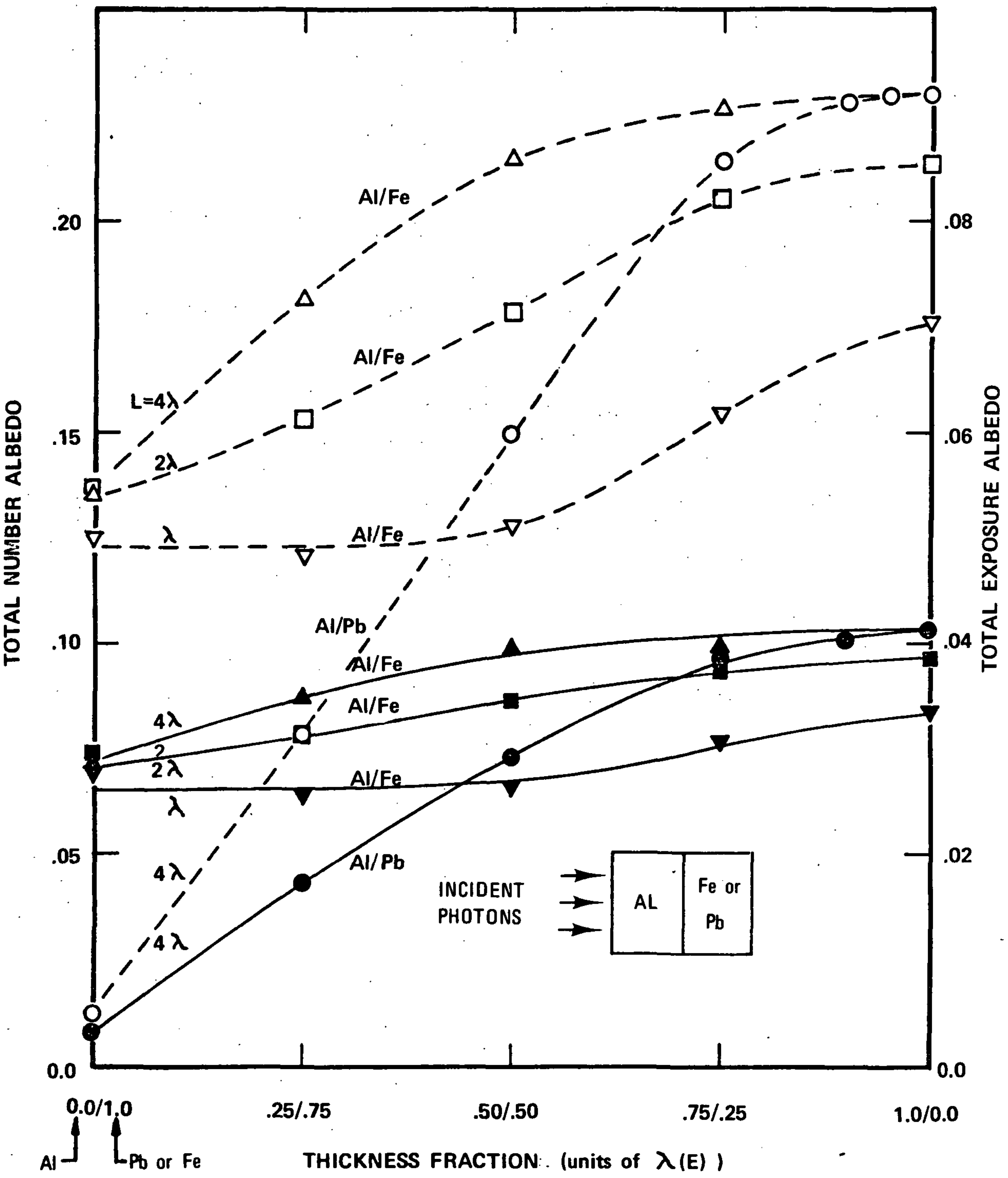

FIGURE 16
NUMBER(dashed) and EXPOSURE(solid) ALBEDOS for 1.0 MeV PHOTONS
AS A FUNCTION OF LAMINATION THICKNESS FRACTIONS

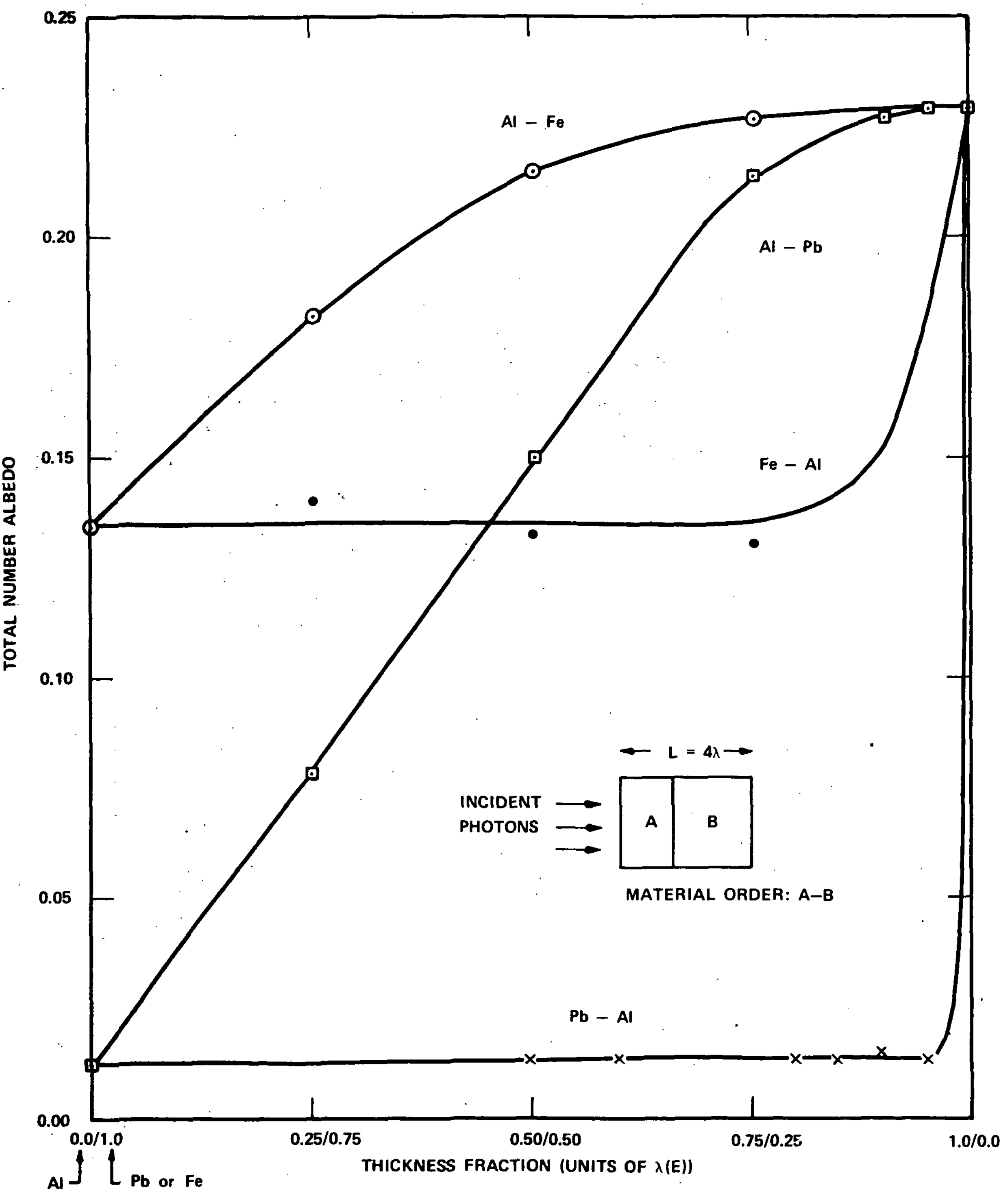

FIGURE 17

NUMBER ALBEDOS FOR 1.0 MeV PHOTONS AS A FUNCTION OF LAMINATION THICKNESS FRACTION

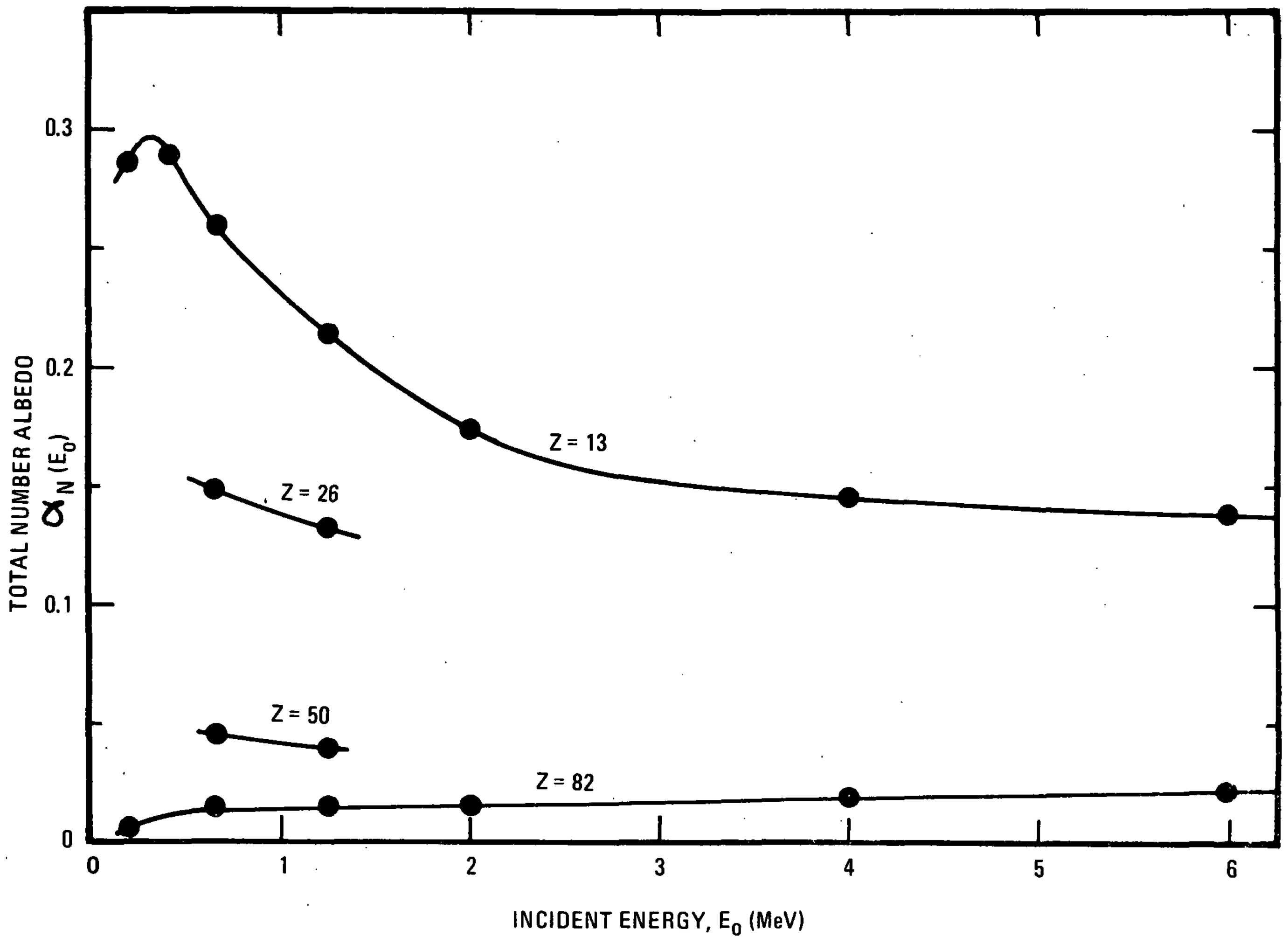

TOTAL NUMBER ALBEDO α_N AS A
FUNCTION OF INCIDENT ENERGY E_0

FIGURE 18

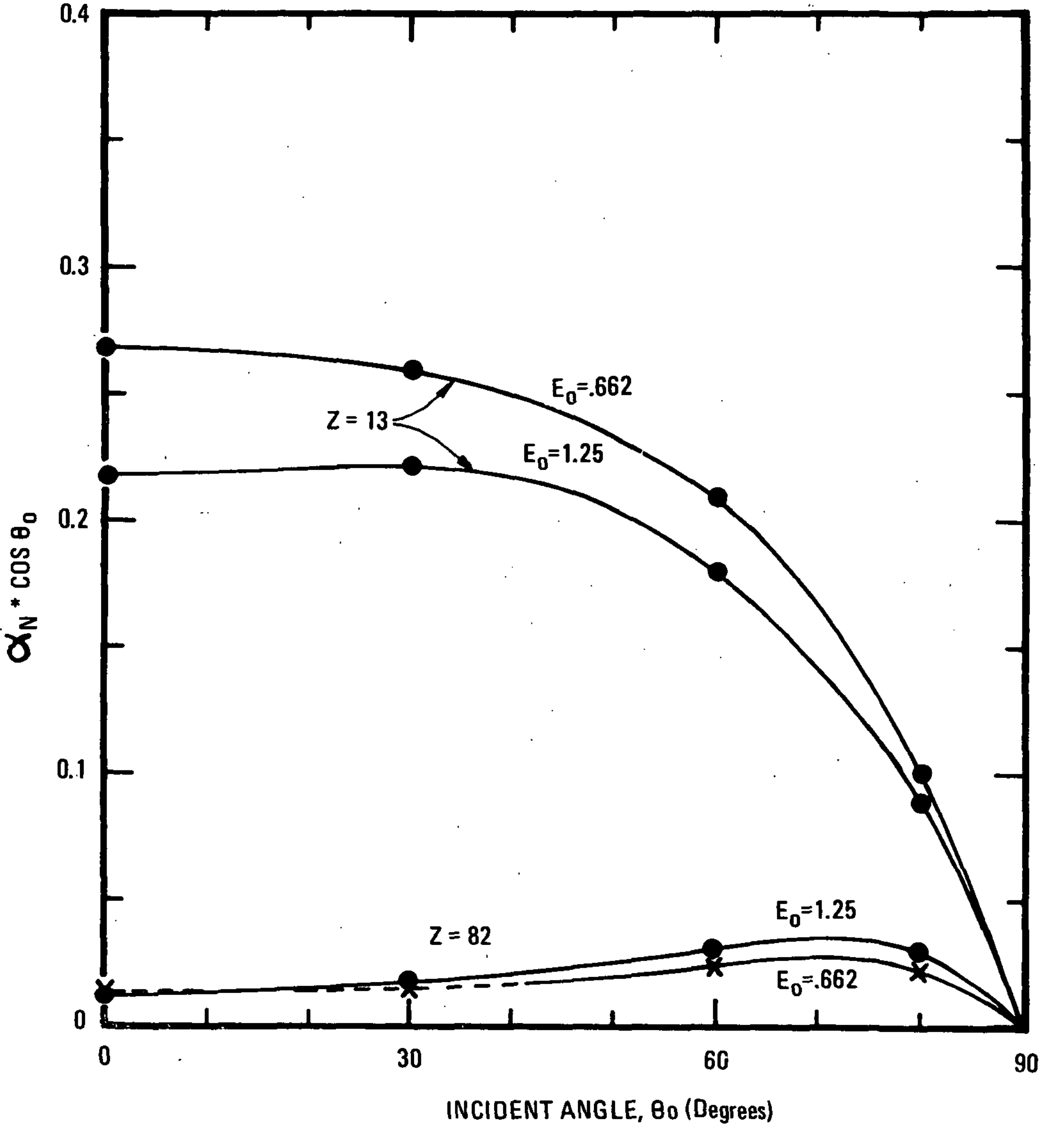

(TOTAL NUMBER ALBEDO α_N)* COS θ_o AS A FUNCTION OF INCIDENT ANGLE θ_o, FOR E_0=0.662 AND 1.25 MeV

FIGURE 19

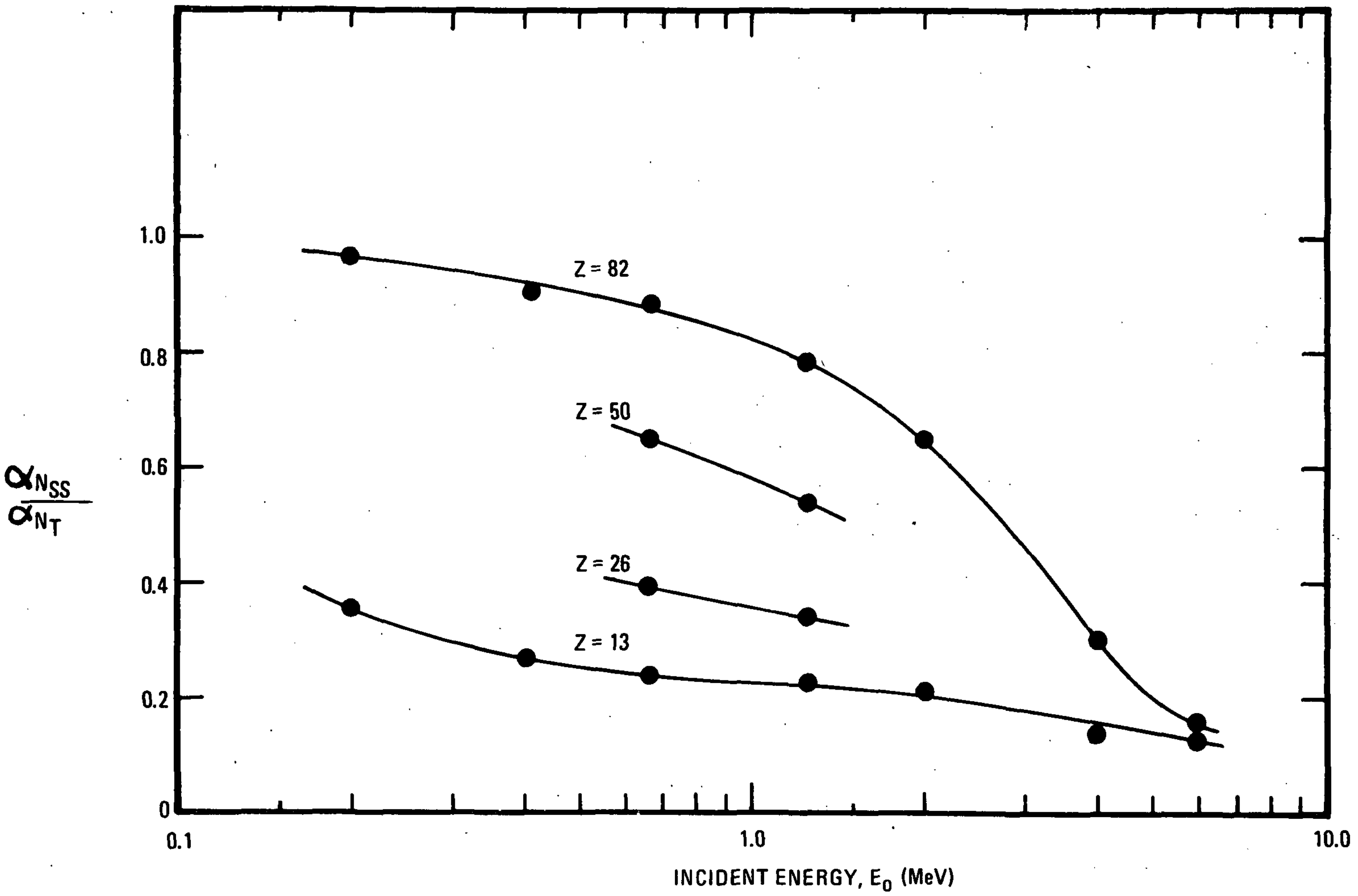

SINGLE SCATTER/TOTAL NUMBER ALBEDO RATIO AS A FUNCTION OF INCIDENT ENERGY E_o

FIGURE 20

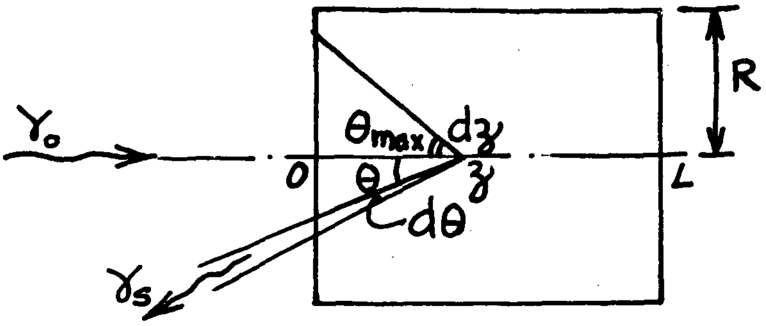

GEOMETRY FOR ANALYTIC (32)
SINGLE BACKSCATTER EQUATION

FIGURE 21

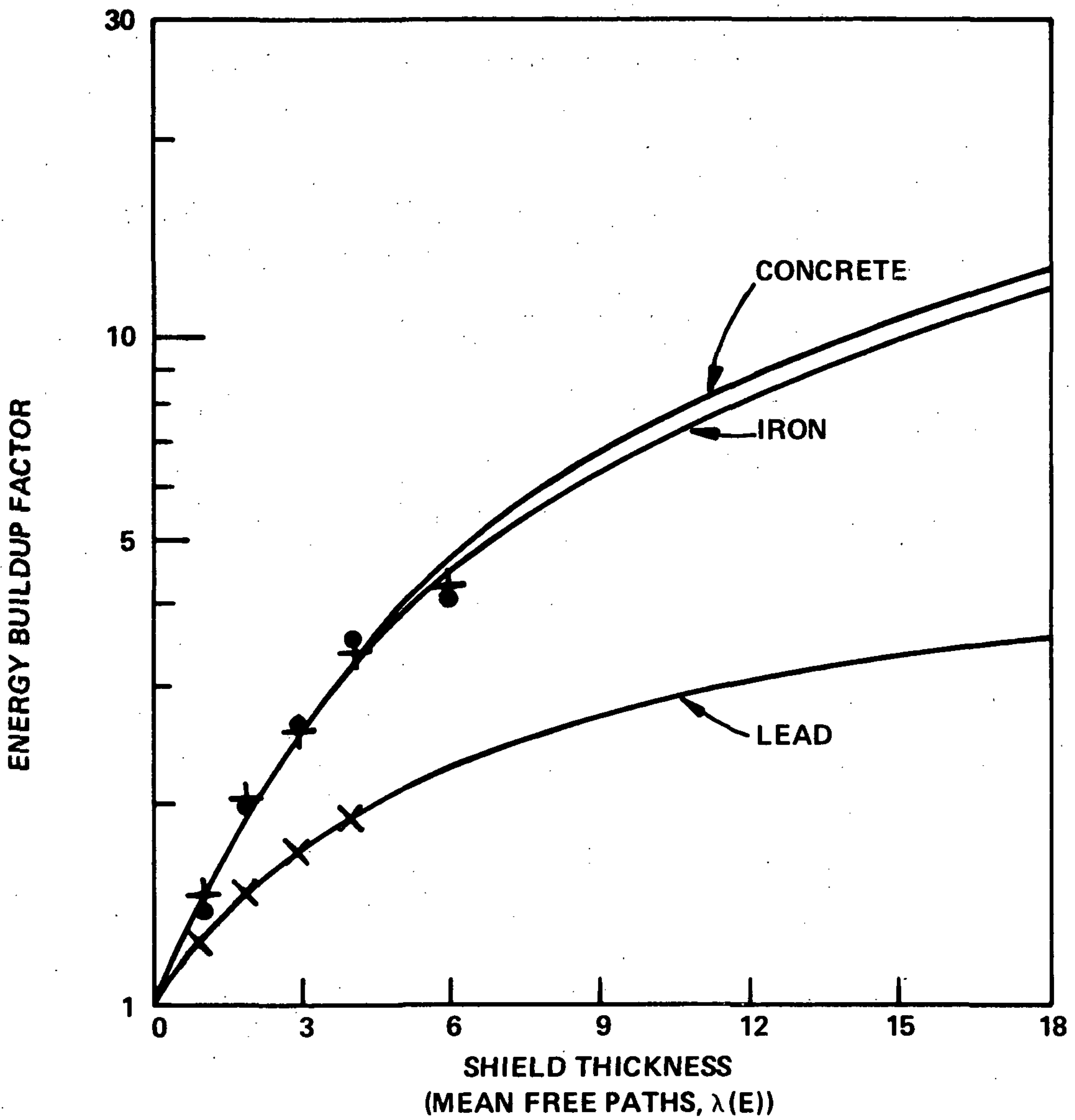

FIGURE 22

COMPARISON OF PRESENT WORK 1.0 MeV ENERGY BUILDUP FACTORS FOR Al (+), Fe (●) AND Pb (X) WITH THE DATA OF PIEPER AND BEACH,(29) AND PEEBLES.(30)

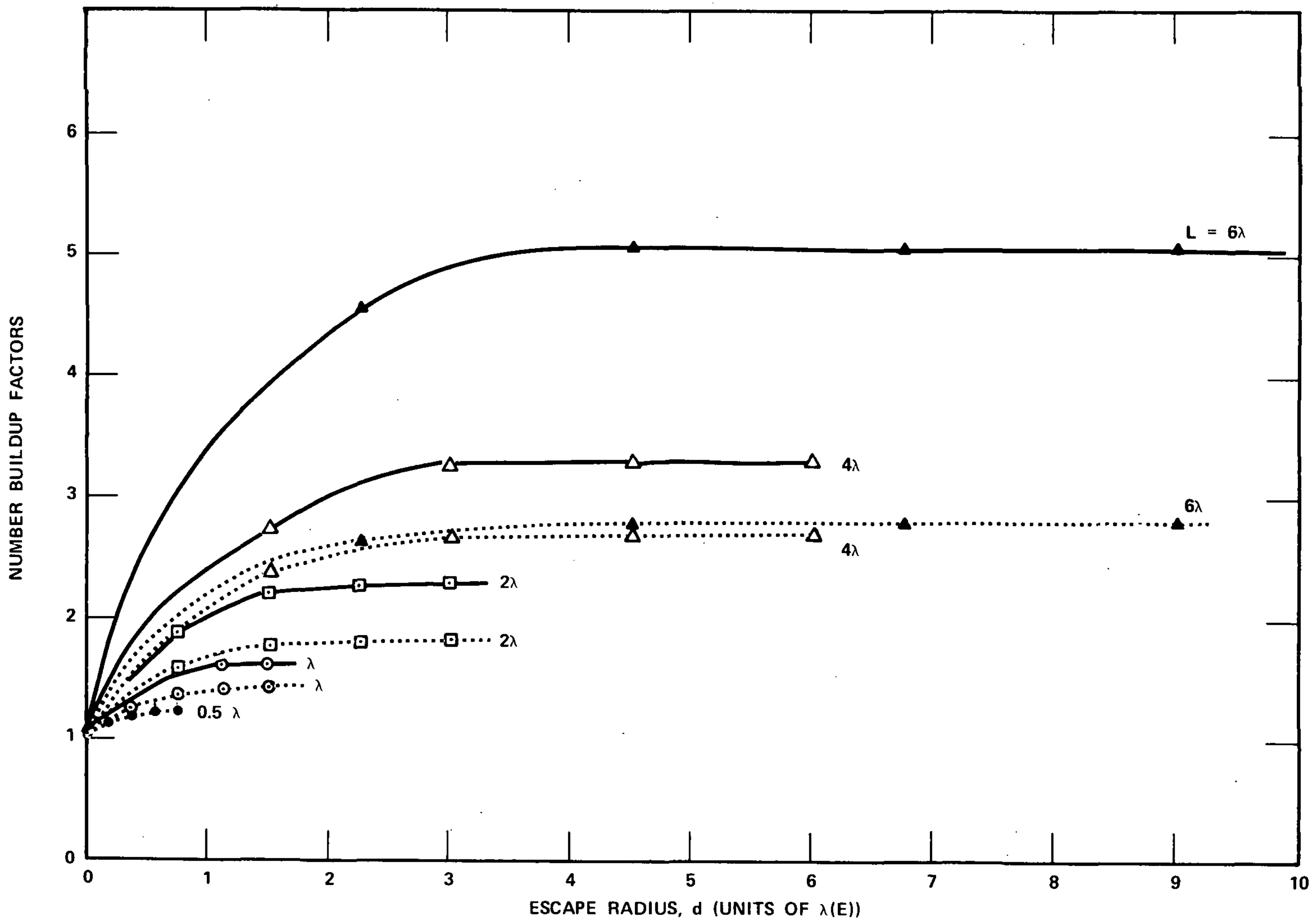

FIGURE 23

NUMBER BUILDUP FACTORS AS A FUNCTION OF RADIAL ESCAPE DISTANCE d AND SHIELD THICKNESS L FOR 0.5 (dotted) AND 1.0 MeV (solid) PHOTONS INCIDENT ON TIN

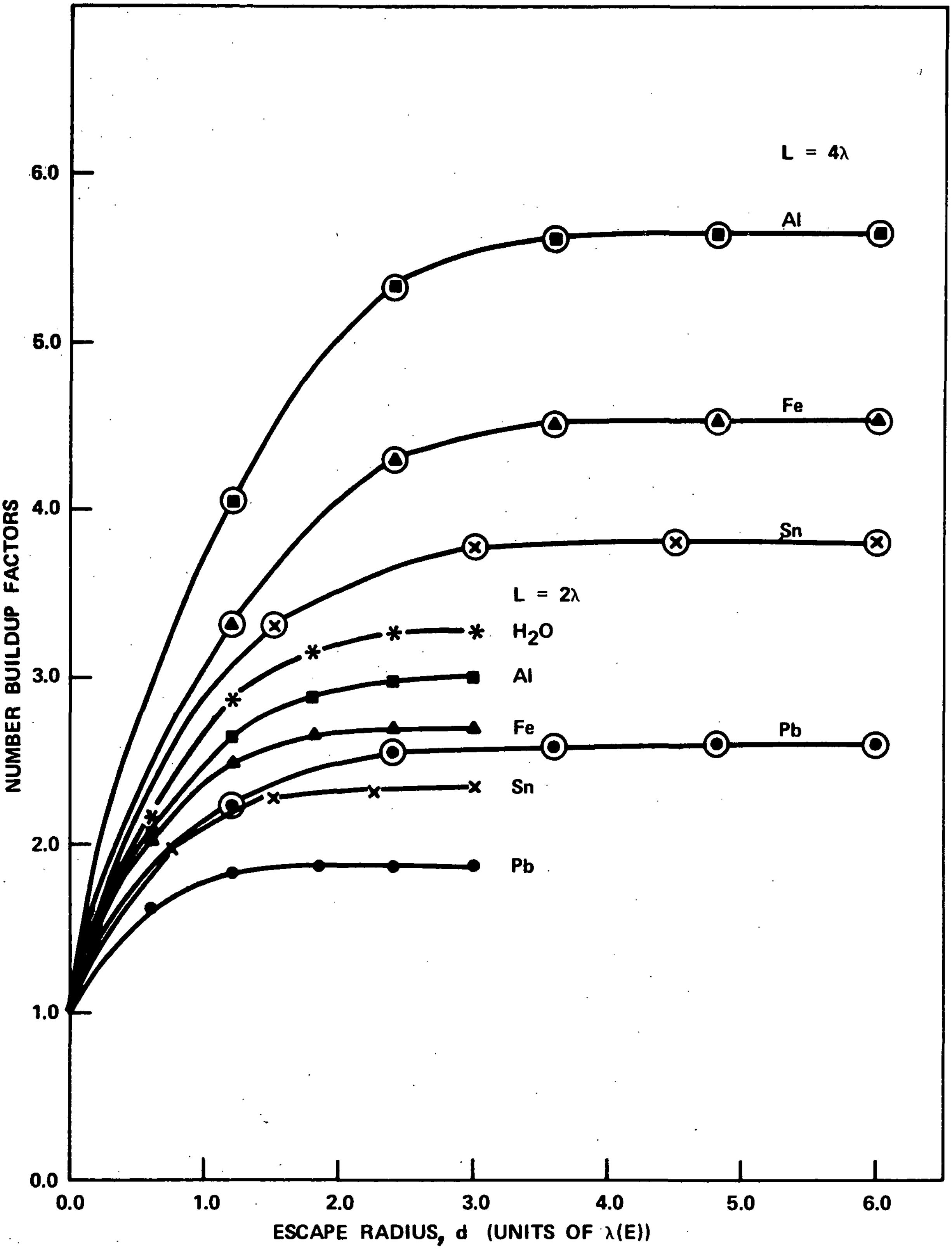

FIGURE 24

NUMBER BUILDUP FACTORS AS A FUNCTION OF RADIAL ESCAPE DISTANCE d FOR 2.0 MeV PHOTONS

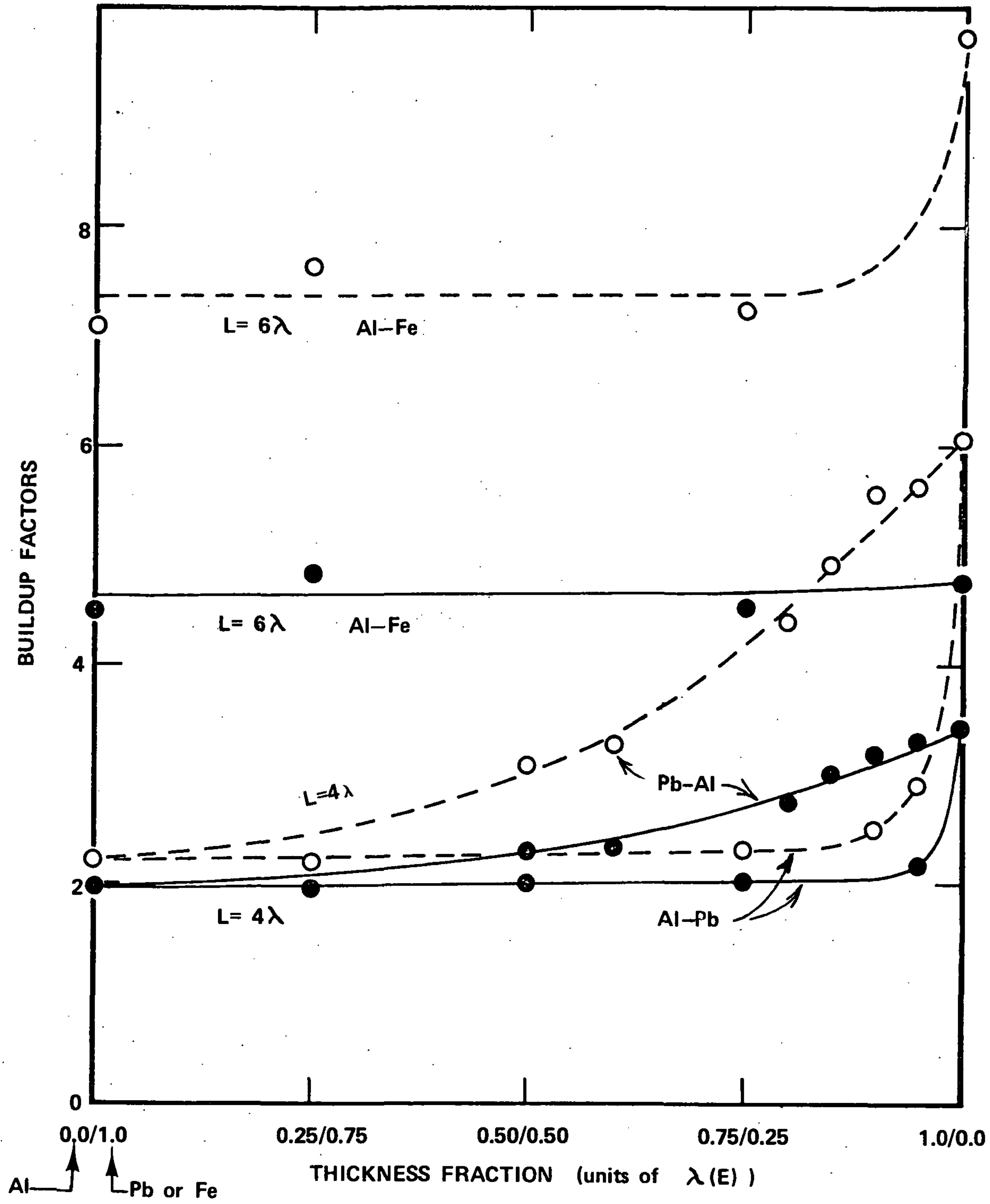

FIGURE 25

NUMBER(dashed) and ENERGY(solid) BUILDUP FACTORS for 1.0 MeV PHOTONS AS A FUNCTION OF LAMINATION THICKNESS FRACTION

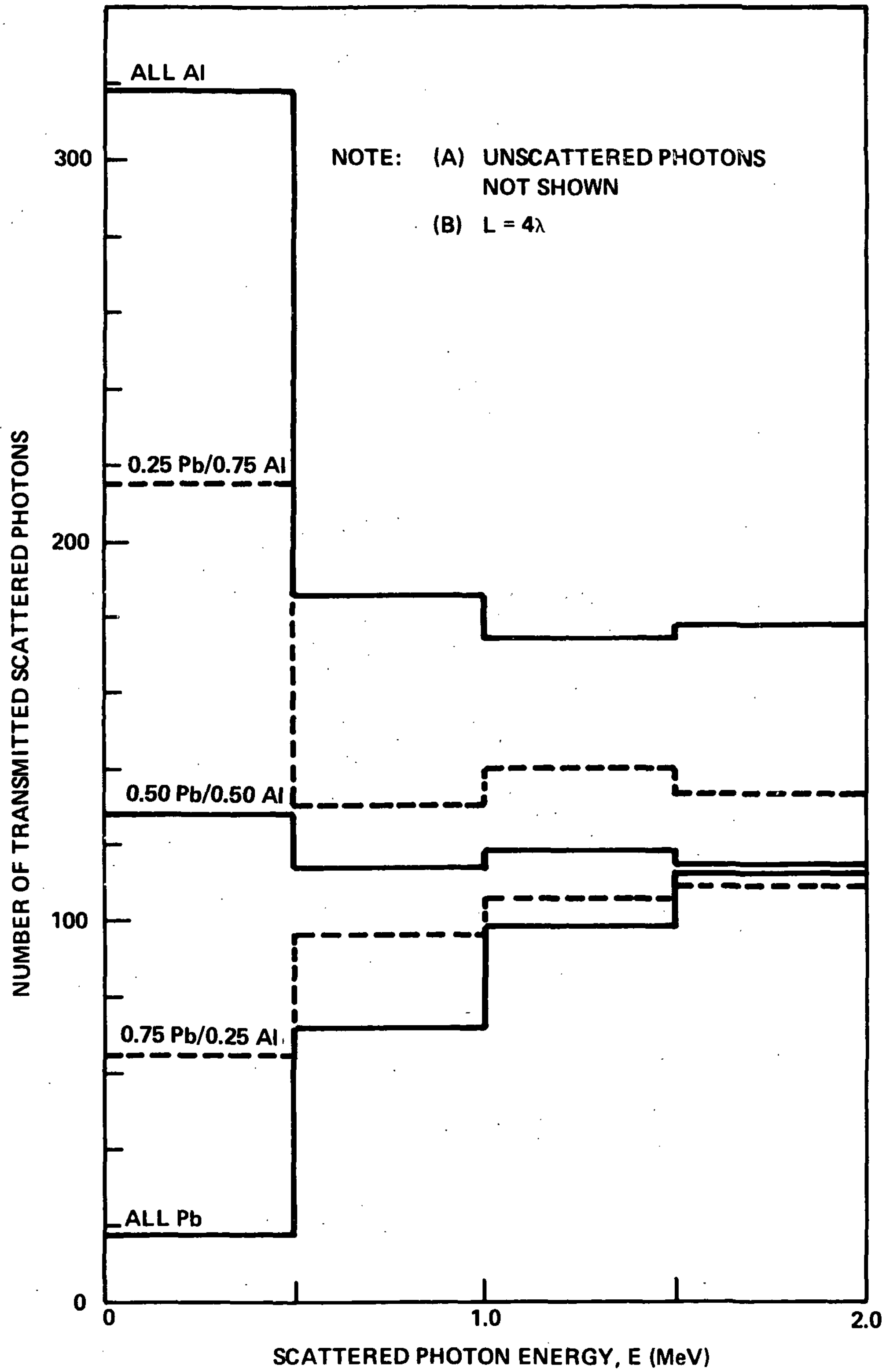

FIGURE 26

SCATTER SPECTRA FOR (2.0 MeV) PHOTONS TRANSMITTED BY Pb – Al SHIELDS AS A FUNCTION OF LAMINATION THICKNESS FRACTION

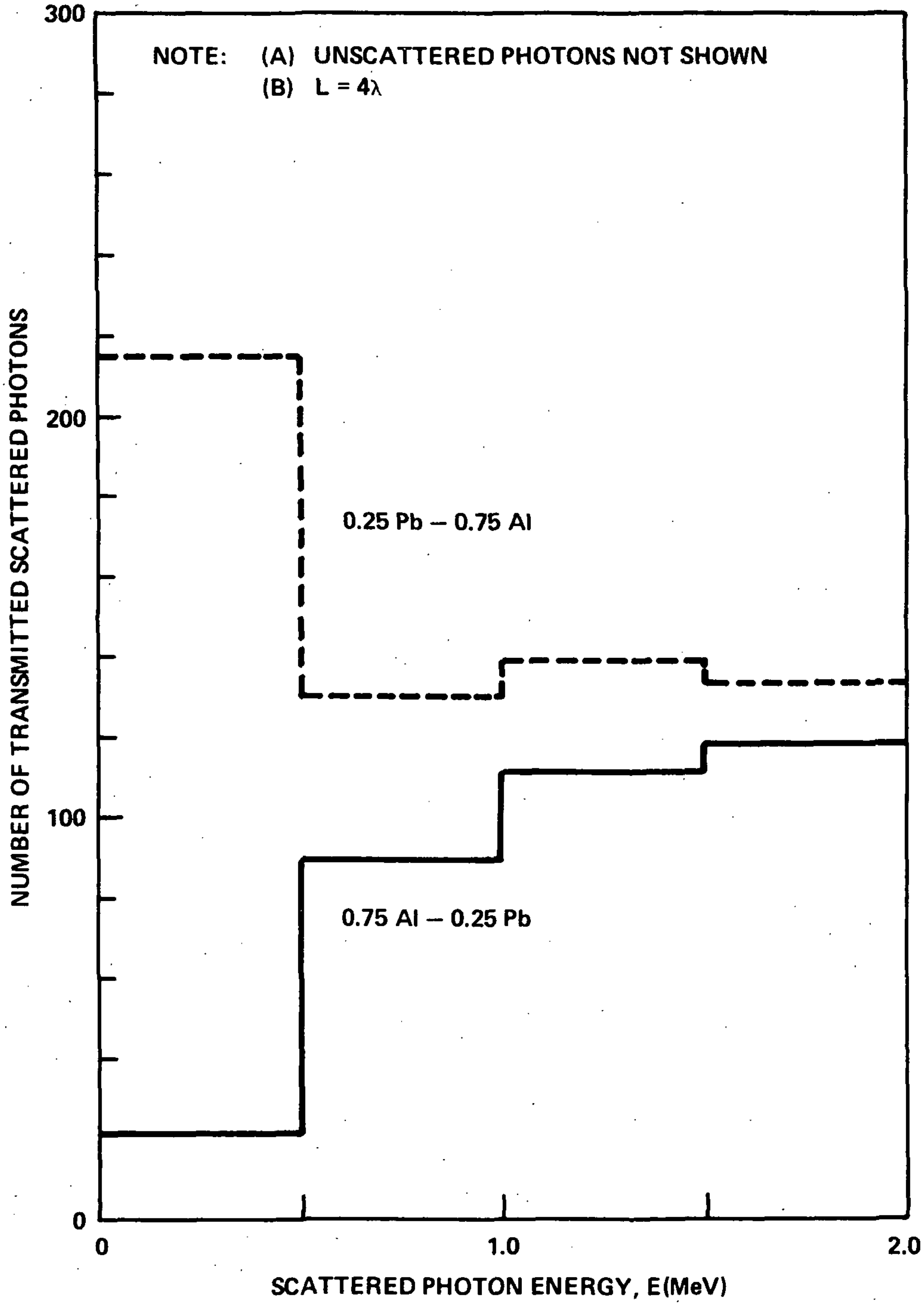

FIGURE 27

SCATTER SPECTRA FOR (2.0 MeV) PHOTONS TRANSMITTED BY Al – Pb AND Pb – Al SHIELDS

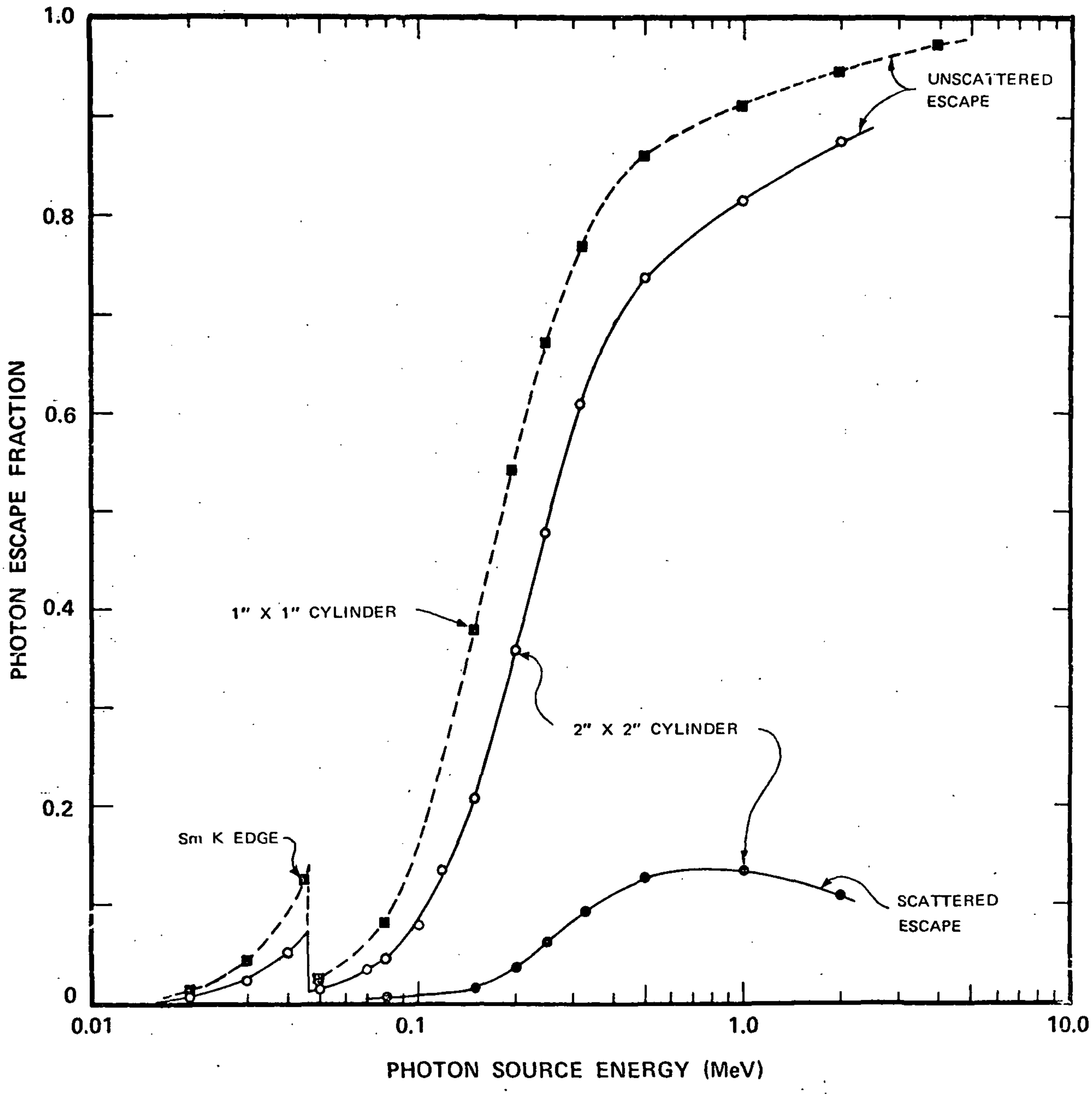

FIGURE 28

PHOTON NUMBER FRACTION EMITTED INTO 4π STERADIANS FROM Sm_2O_3 SOURCE CYLINDER

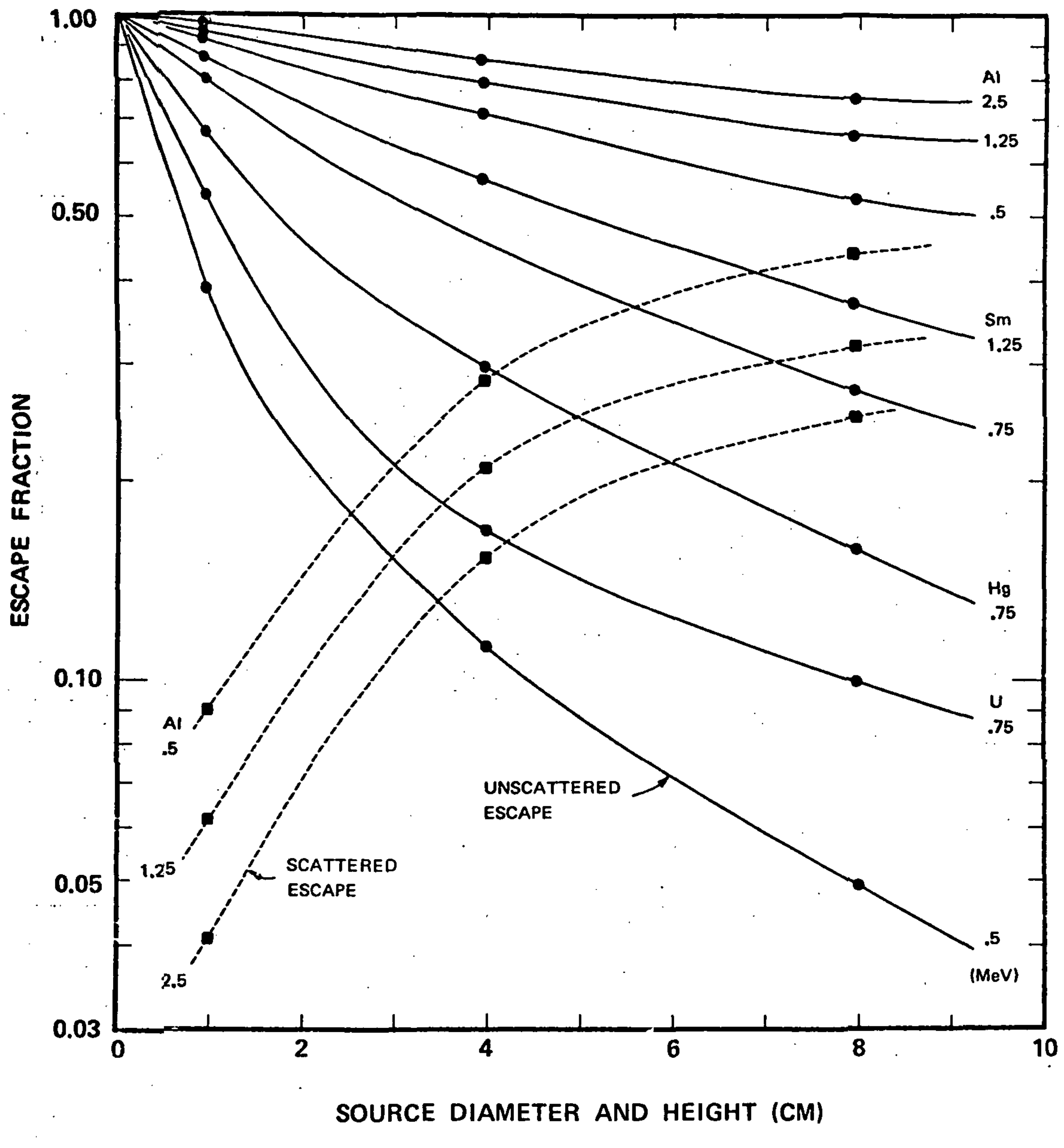

FIGURE 29

PHOTON NUMBER FRACTION EMITTED INTO 4π STERADIANS AS A FUNCTION OF SOURCE SIZE FOR SELECTED INITIAL PHOTON ENERGIES AND SOURCE MEDIA

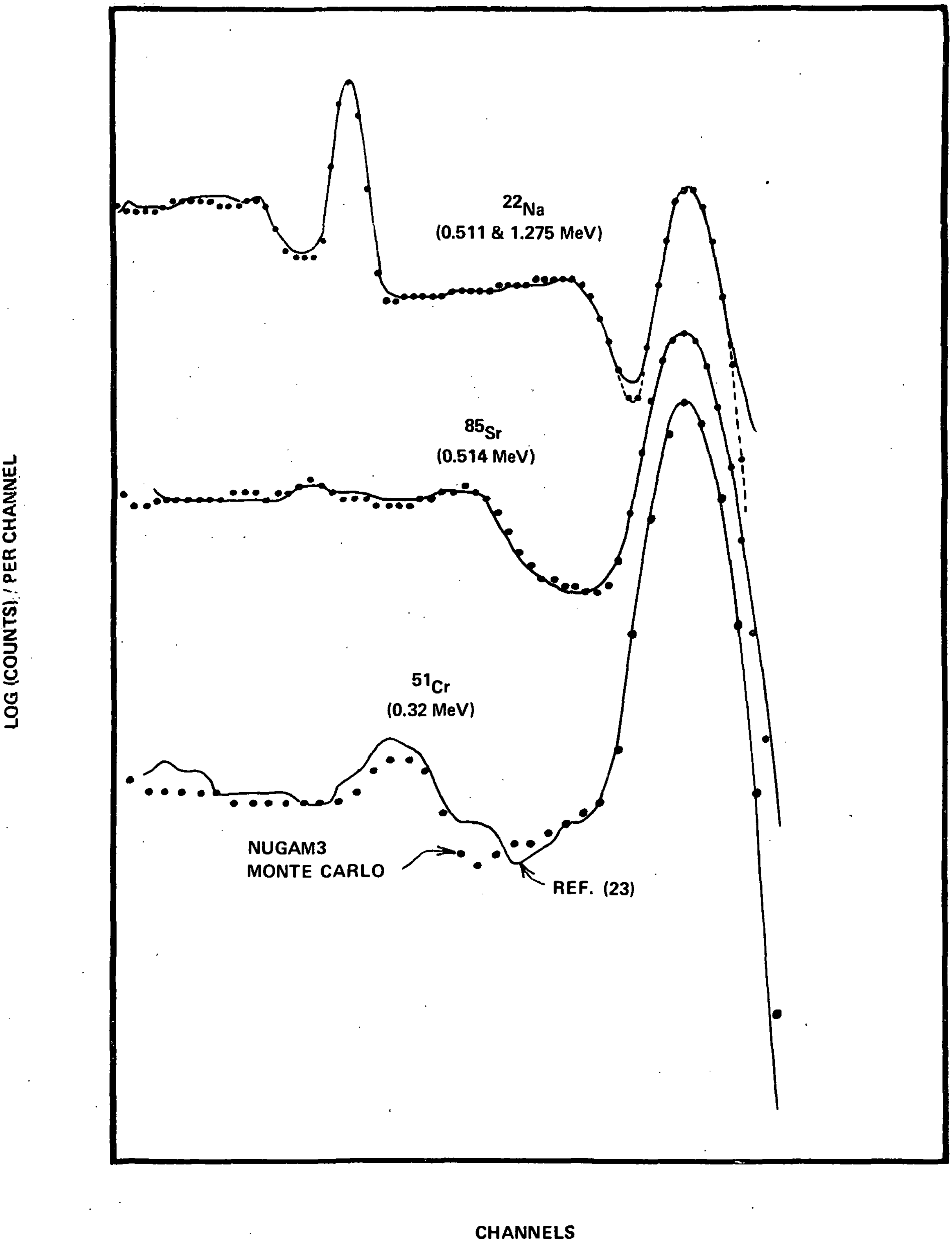

FIGURE 30
COMPARISON OF REFERENCE (23) EXPERIMENTAL SPECTRA
AND WITH NUGAM3 MONTE CARLO SPECTRA

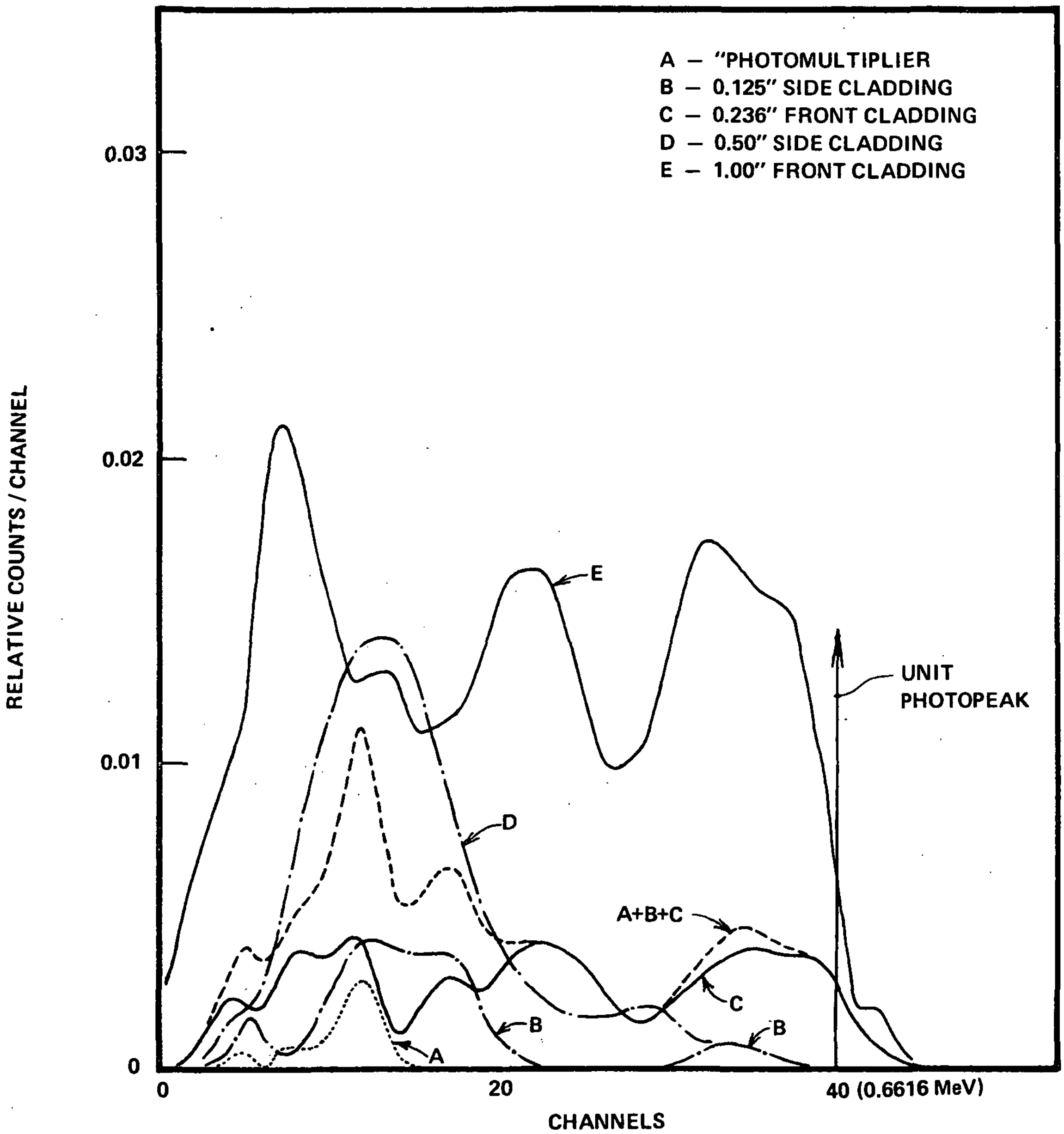

FIGURE 31

CLADDING AND PHOTOMULTIPLIER
RELATIVE COMPONENT SPECTRA

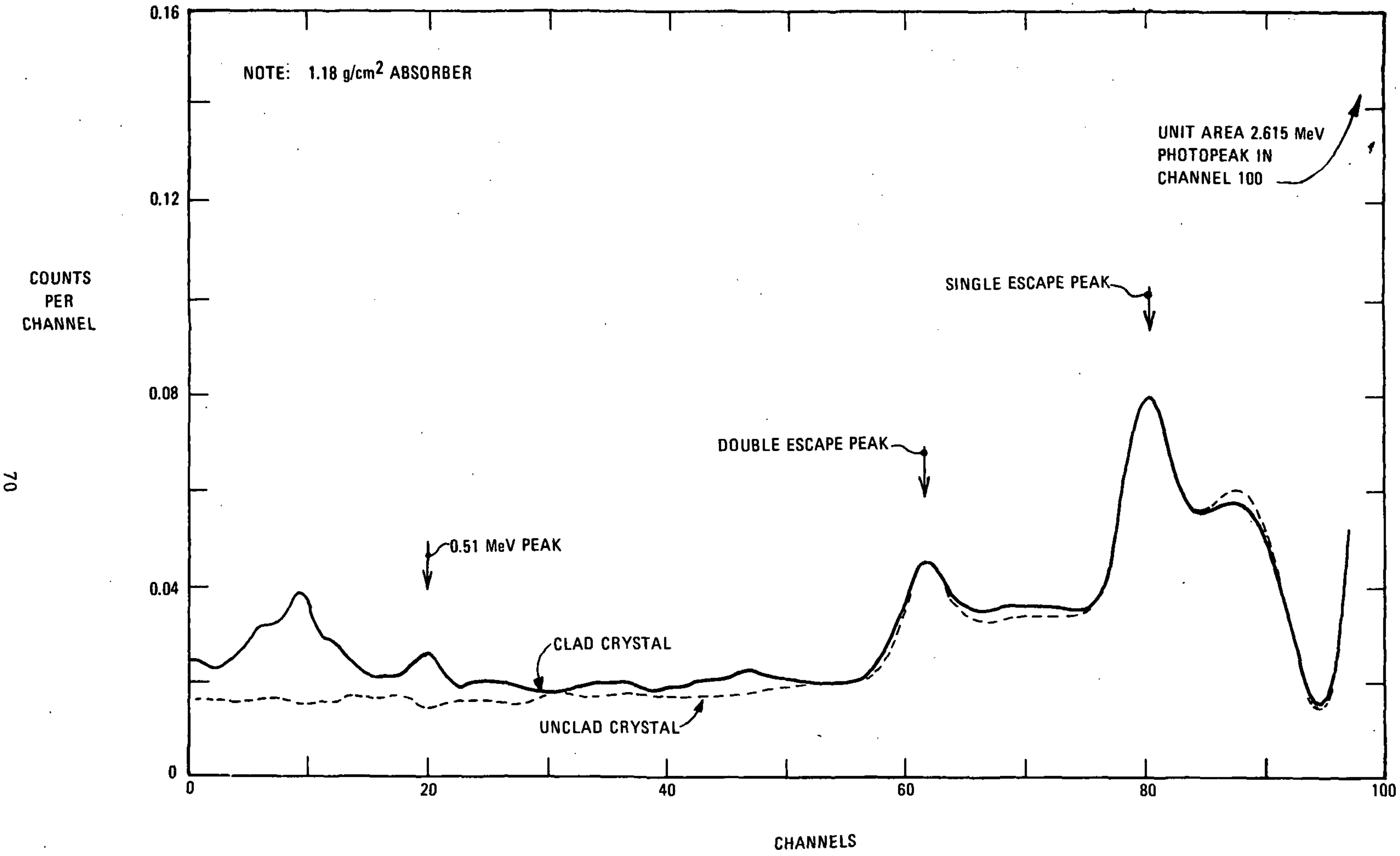

FIGURE 32

DISTRIBUTION FOR CLAD AND UNCLAD 3" x 3" NaI (Tℓ)
CRYSTAL EXPOSED TO POINT SOURCE AT 10cm DISTANCE

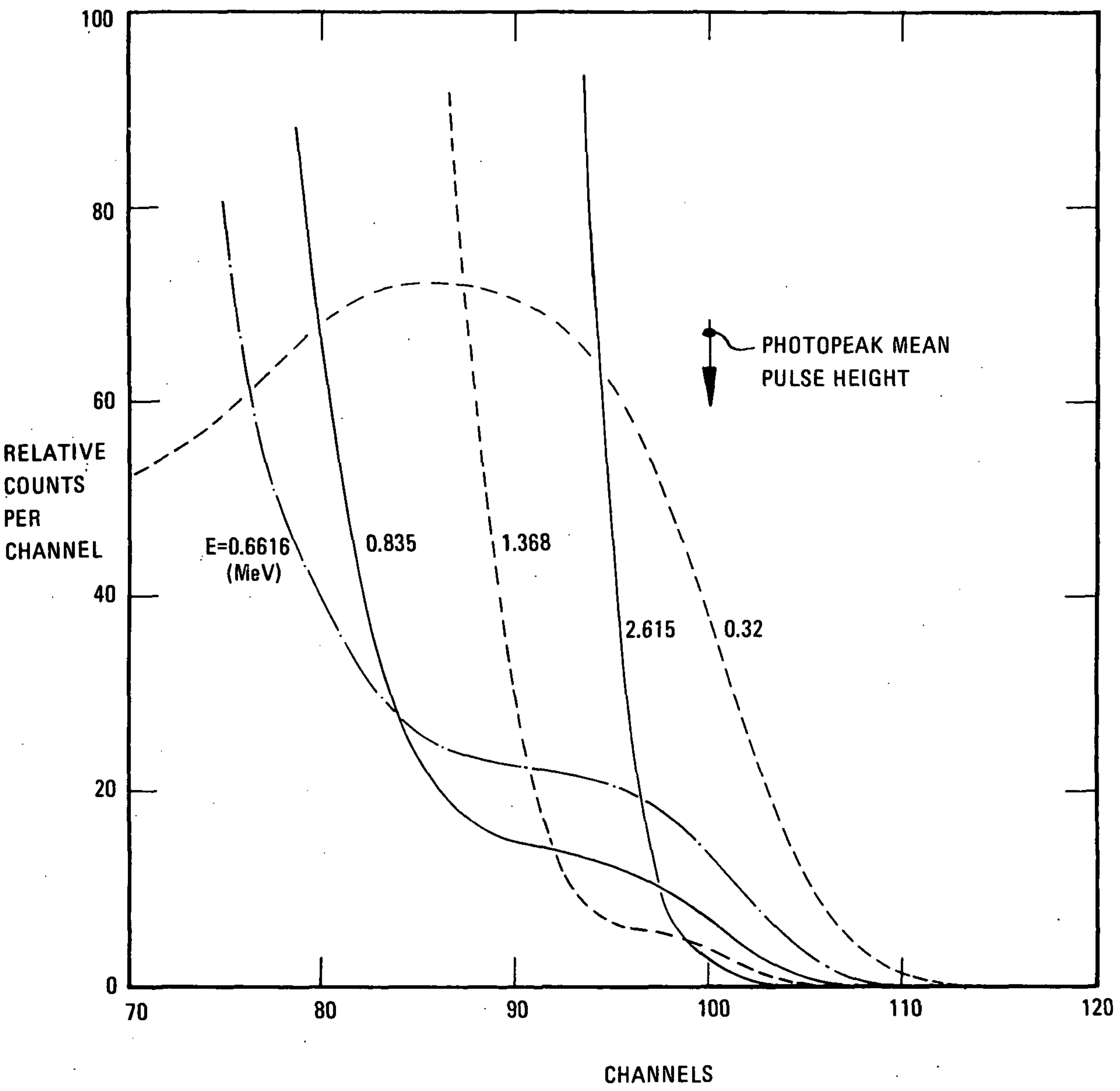

FIGURE 33

COMPTON TAIL DISTRIBUTIONS FOR 3" x 3"
NaI (Tℓ) CLAD CRYSTAL AND 10cm DISTANT POINT SOURCE
(GAUSSIAN SMEARED AND NORMALIZED TO 50,000 PHOTON HISTORIES)
(1.18 g/cm^2 ABSORBER)

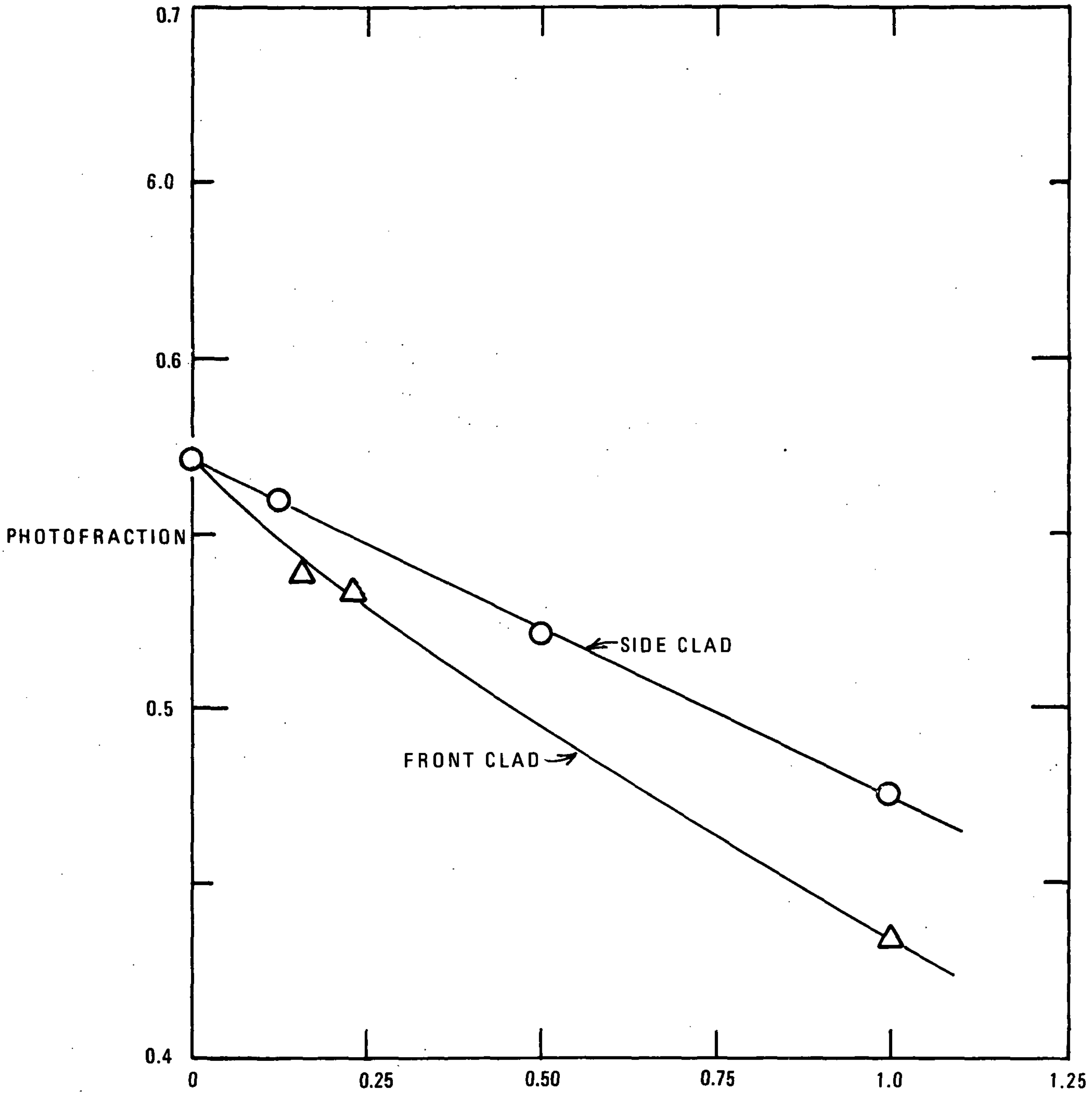

FIGURE 34
PHOTOFRACTION AS A FUNCTION OF CLADDING THICKNESS FOR 3"x 3"NaI (Tℓ) CRYSTAL EXPOSED TO AXIAL POINT SOURCE OF 0.662 MeV PHOTONS

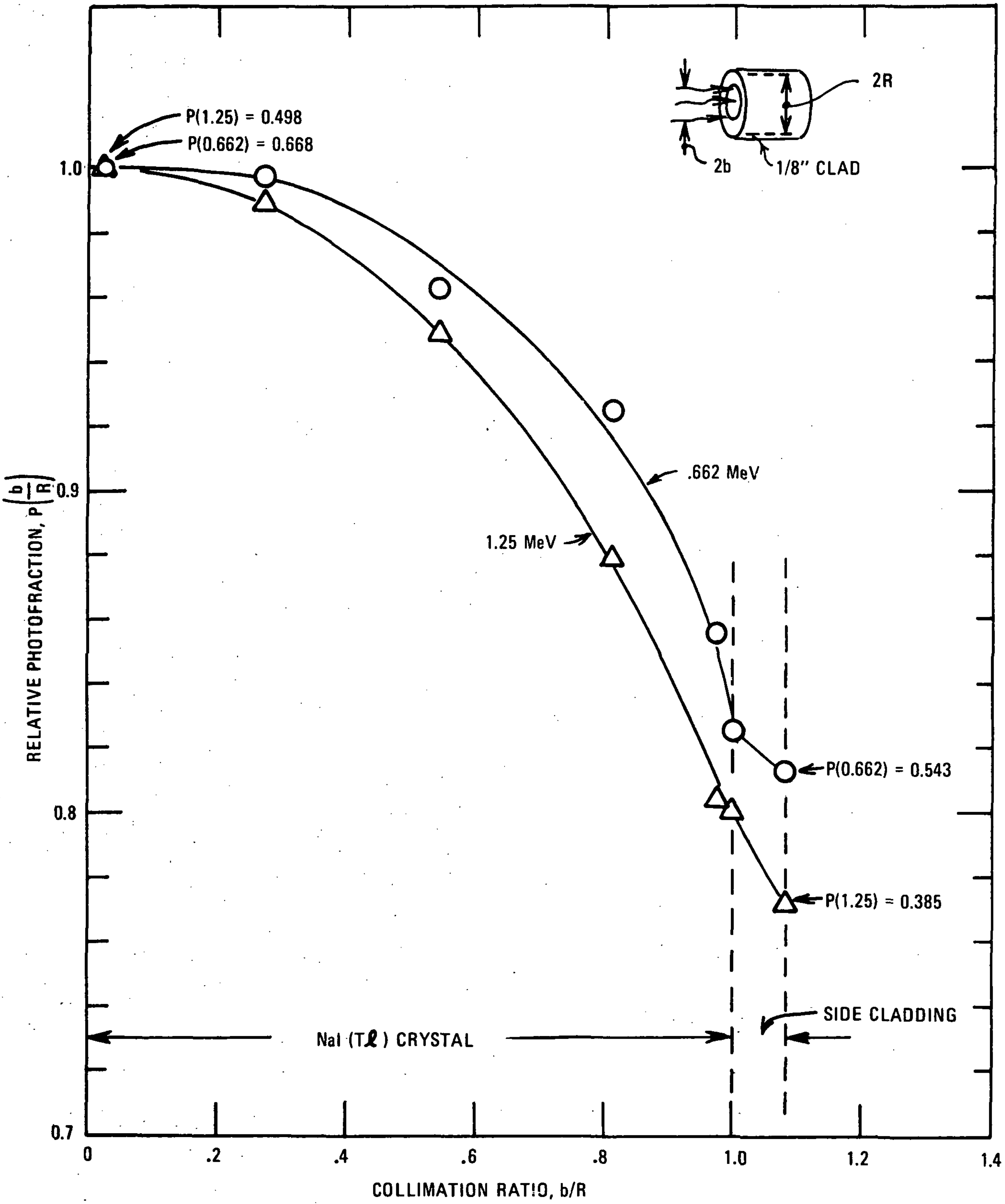

FIGURE 35
RELATIVE PHOTOFRACTION AS A FUNCTION OF COLLIMATION OF BROAD PARALLEL BEAM FOR CLAD 3" x 3" NaI (Tℓ) CRYSTAL

TABLES

TABLE 1

THE EXPERIMENTAL RATIO $(\tau_{pe}/\tau_K)_{K\text{-edge}}$ AS DERIVED FROM KIRCHNER [1930] BY DAVISSON [1965].(17)

Element	$(\tau_{pe}/\tau_K)_{K\text{-edge}}$	Element	$(\tau_{pe}/\tau_K)_{K\text{-edge}}$
$_1H$	1.00	$_{20}Ca$	1.11
$_4Be$	1.03	$_{28}Fe$	1.12
$_6C$	1.04	$_{29}Cu$	1.13
$_7N$	1.05	$_{42}Mo$	1.16
$_8O$	1.06	$_{50}Sn$	1.18
$_{11}Na$	1.075	$_{53}I$	1.19
$_{12}Mg$	1.08	$_{74}W$	1.20
$_{13}Al$	1.09	$_{79}Pt$	1.22
$_{14}Si$	1.09	$_{82}Pb$	1.22
$_{18}Ar$	1.10	$_{92}U$	1.235
$_{19}P$	1.10		

TABLE 2

K FLUORESCENT YIELD AS A FUNCTION OF ATOMIC NUMBER(19)

Atomic Number	Yield
10	.017
15	.050
20	.160
25	.30
30	.475
40	.71
50	.83
60	.90
70	.95
80	.967
90	.975

TABLE 3
X–RAY CRITICAL ABSORPTION AND EMISSION ENERGIES IN KEV (20)

K Series

Line	α	α_1	α_2	β_1	β_3	β_2	β_4	β_5	-
Transition K ⟶		L_{III}	L_{II}	M_{III}	M_{II}	$N_{II}N_{III}$	$N_{IV}N_V$	$M_{IV}M_V$	$O_{II,III}$
Approximate Intensity (Relative $K_{\alpha 1}$)	150	100	50	15		5	1	1	1

L Series

Line	α	α_1	α_2	β_1	β_2	β_3	β_4	β_5	γ_1	γ_2	γ_3	γ_4	γ_6
Transition L_I ⟶ L_{II} ⟶ L_{III} ⟶		M_V	M_{IV}	M_{IV}	N_V	M_{III}	M_{II}	$O_{IV,V}$	N_{IV}	N_{II}	N_{III}	O_{III}	O_{IV}
Approximate Intensity (Relative $L_{\alpha 1}$)	110	100	10	80	60	30	20	30	40	10	10	10	20

	K_{ab}	K_{β_2}	K_{β_1}	K_{α_1}	K_{α_2}	L_{Iab}	L_{IIab}	L_{IIIab}	L_{γ_1}	L_{β_2}	L_{β_1}	L_{α_1}	L_{α_2}
1-H	0.0136												
2-He	0.0246												
3-Li	0.055			0.052									
4-Be	0.116			0.110									
5-B	0.192			0.185									
6-C	0.283			0.282									
7-N	0.399			0.392									
8-O	0.531			0.523									
9-F	0.687			0.677									
10-Ne	0.874			0.851		0.048	0.022	0.022					
11-Na	1.08		1.067	1.041		0.055	0.034	0.034					
12-Mg	1.303		1.297	1.254		0.063	0.050	0.049					
13-Al	1.559		1.553	1.487	1.486	0.087	0.073	0.072					
14-Si	1.838		1.832	1.740	1.739	0.118	0.099	0.098					
15-P	2.142		2.136	2.015	2.014	0.153	0.129	0.128					
16-S	2.470		2.464	2.308	2.306	0.193	0.164	0.163					
17-Cl	2.826		2.815	2.622	2.621	0.238	0.203	0.202					
18-A	3.203		3.192	2.957	2.955	0.287	0.247	0.245					
19-K	3.607		3.589	3.313	3.310	0.341	0.297	0.294					
20-Ca	4.038		4.012	3.691	3.688	0.399	0.352	0.349			0.344		0.341
21-Sc	4.496		4.460	4.090	4.085	0.462	0.411	0.406			0.399		0.395
22-Ti	4.964		4.931	4.510	4.504	0.530	0.460	0.454			0.458		0.452
23-V	5.463		5.427	4.952	4.944	0.604	0.519	0.512			0.519		0.510
24-Cr	5.988		5.946	5.414	5.405	0.679	0.583	0.574			0.581		0.571
25-Mn	6.537		6.490	5.898	5.887	0.762	0.650	0.639			0.647		0.636
26-Fe	7.111		7.057	6.403	6.390	0.849	0.721	0.708			0.717		0.704
27-Co	7.709		7.649	6.930	6.915	0.929	0.794	0.779			0.790		0.775
28-Ni	8.331	8.328	8.264	7.477	7.460	1.015	0.871	0.853			0.866		0.849
29-Cu	8.980	8.976	8.904	8.047	8.027	1.100	0.953	0.933			0.948		0.928
30-Zn	9.660	9.657	9.571	8.638	8.615	1.200	1.045	1.022			1.032		1.009
31-Ga	10.368	10.365	10.263	9.251	9.234	1.30	1.134	1.117			1.122		1.096
32-Ge	11.103	11.100	10.981	9.885	9.854	1.42	1.248	1.217			1.216		1.186
33-As	11.863	11.863	11.725	10.543	10.507	1.529	1.359	1.323			1.317		1.282
34-Se	12.652	12.651	12.495	11.221	11.181	1.652	1.473	1.434			1.419		1.379
35-Br	13.475	13.465	13.290	11.923	11.877	1.794	1.599	1.552			1.526		1.480
36-Kr	14.323	14.313	14.112	12.648	12.597	1.931	1.727	1.675			1.638		1.587
37-Rb	15.201	15.184	14.960	13.394	13.335	2.067	1.866	1.806			1.752	1.694	1.692
38-Sr	16.106	16.083	15.834	14.164	14.097	2.221	2.008	1.941			1.872	1.806	1.805
39-Y	17.037	17.011	16.736	14.957	14.882	2.369	2.154	2.079			1.996	1.922	1.920
40-Zr	17.998	17.969	17.666	15.774	15.690	2.547	2.305	2.220	2.302	2.219	2.124	2.042	2.040
41-Nb	18.987	18.951	18.621	16.614	16.520	2.706	2.467	2.374	2.462	2.367	2.257	2.166	2.163
42-Mo	20.002	19.964	19.607	17.478	17.373	2.884	2.627	2.523	2.623	2.518	2.395	2.293	2.290
43-Tc	21.054	21.012	20.612	18.370	18.250	3.054	2.795	2.677	2.792	2.674	2.538	2.424	2.420
44-Ru	22.118	22.072	21.655	19.278	19.149	3.236	2.966	2.837	2.964	2.836	2.683	2.558	2.554
45-Rh	23.224	23.169	22.721	20.214	20.072	3.419	3.145	3.002	3.144	3.001	2.834	2.696	2.692
46-Pd	24.347	24.297	23.816	21.175	21.018	3.617	3.329	3.172	3.328	3.172	2.990	2.838	2.833
47-Ag	25.517	25.454	24.942	22.162	[illegible]	3.810	3.528	3.352	3.519	3.348	3.151	2.984	2.978
48-Cd	26.712	26.641	26.093	23.172	22.984	4.019	3.727	3.538	3.716	3.528	3.316	3.133	3.127
49-In	27.928	27.859	27.274	24.207	24.000	4.237	3.939	3.729	3.920	3.713	3.487	3.287	3.279
50-Sn	29.190	29.106	28.483	25.277	25.042	4.464	4.157	3.928	4.131	3.904	3.662	3.444	3.435
51-Sb	30.486	30.387	29.723	26.357	26.109	4.697	4.381	4.132	4.347	4.100	3.843	3.605	3.595
52-Te	31.809	31.698	30.993	27.471	27.200	4.938	4.613	4.341	4.570	4.301	4.029	3.769	3.758
53-I	33.164	33.016	32.292	28.610	28.315	5.190	4.856	4.559	4.800	4.507	4.220	3.937	3.926
54-Xe	34.579	34.398	33.644	29.779	29.463	5.452	5.104	4.782	5.036	4.720	4.422	4.111	4.098
55-Cs	35.959	35.819	34.984	30.970	30.623	5.720	5.358	5.011	5.280	4.936	4.620	4.286	4.272
56-Ba	37.410	37.255	36.376	32.191	31.815	5.995	5.623	5.247	5.531	5.156	4.828	4.467	4.451
57-La	38.931	38.728	37.799	33.440	33.033	6.283	5.894	5.489	5.789	5.384	5.043	4.651	4.635
58-Ce	40.449	40.231	39.255	34.717	34.276	6.561	6.165	5.729	6.052	5.613	5.262	4.840	4.823
59-Pr	41.998	41.772	40.746	36.023	35.548	6.846	6.443	5.968	6.322	5.850	5.489	5.034	5.014
60-Nd	43.571	43.349	42.269	37.359	36.845	7.144	6.727	6.215	6.602	6.090	5.722	5.230	5.208
61-Pm	45.207	44.955	43.811	38.726	38.180	7.448	7.018	6.466	6.891	6.336	5.956	5.431	5.408
62-Sm	46.846	46.581	45.400	40.124	39.523	7.754	7.312	6.721	7.180	6.587	6.206	5.636	5.609
63-Eu	48.515	48.241	47.027	41.529	40.877	8.069	7.624	6.983	7.478	6.842	6.456	5.846	5.816
64-Gd	50.229	49.961	48.718	42.983	42.280	8.393	7.940	7.252	7.788	7.102	6.714	6.059	6.027
65-Tb	51.998	51.737	50.391	44.470	43.737	8.724	8.258	7.519	8.104	7.368	6.979	6.275	6.241
66-Dy	53.789	53.491	52.187	45.985	45.193	9.083	8.591	7.790	8.418	7.638	7.249	6.495	6.457
67-Ho	55.615	55.292	53.934	47.528	46.686	9.411	8.920	8.074	8.748	7.912	7.528	6.720	6.680
68-Er	57.483	57.088	55.690	49.099	48.205	9.776	9.263	8.364	9.089	8.188	7.810	6.948	6.904
69-Tm	59.382	58.969	57.487	50.730	49.762	10.144	9.628	8.652	9.424	8.472	8.103	7.181	7.135
70-Yb	61.303	60.959	59.352	52.360	51.326	10.486	9.977	8.943	9.779	8.758	8.401	7.414	7.367
71-Lu	63.304	62.946	61.282	54.063	52.959	10.867	10.345	9.241	10.142	9.048	8.708	7.654	7.604
72-Hf	65.313	64.936	63.209	55.757	54.579	11.264	10.734	9.556	10.516	9.346	9.021	7.898	7.843
73-Ta	67.400	66.999	65.210	57.524	56.270	11.676	11.130	9.876	10.892	9.649	9.341	8.145	8.087
74-W	69.508	69.090	67.233	59.310	57.973	12.090	11.535	10.198	11.283	9.959	9.670	8.396	8.335
75-Re	71.662	71.220	69.298	61.131	59.707	12.522	11.955	10.531	11.684	10.273	10.008	8.651	8.584
76-Os	73.860	73.393	71.404	62.991	61.477	12.965	12.383	10.869	12.094	10.596	10.354	8.910	8.840
77-Ir	76.097	75.605	73.549	64.886	63.278	13.413	12.819	11.211	12.509	10.918	10.706	9.173	9.098
78-Pt	78.379	77.866	75.736	66.820	65.111	13.873	13.268	11.559	12.939	11.249	11.069	9.441	9.360
79-Au	80.713	80.165	77.968	68.794	66.980	14.353	13.733	11.919	13.379	11.582	11.439	9.711	9.625
80-Hg	83.106	82.526	80.258	70.821	68.894	14.841	14.212	12.285	13.828	11.923	11.823	9.987	9.896
81-Tl	85.517	84.904	82.558	72.860	70.820	15.346	14.697	12.657	14.288	12.268	12.210	10.266	10.170
82-Pb	88.001	87.343	84.922	74.957	72.794	15.870	15.207	13.044	14.762	12.620	12.611	10.549	10.448
83-Bi	90.521	89.833	87.335	77.097	74.805	16.393	15.716	13.424	15.244	12.977	13.021	10.836	10.729
84-Po	93.112	92.386	89.809	79.296	76.868	16.935	16.244	13.817	15.740	13.338	13.441	11.128	11.014
85-At	95.740	94.976	92.319	81.525	78.956	17.490	16.784	14.215	16.248	13.705	13.873	11.424	11.304
86-Rn	98.418	97.616	94.877	83.800	81.080	18.058	17.337	14.618	16.768	14.077	14.316	11.724	11.597
87-Fr	101.147	100.305	97.483	86.119	83.243	18.638	17.904	15.028	17.301	14.459	14.770	12.029	11.894
88-Ra	103.927	103.048	100.136	88.485	85.446	19.233	18.481	15.442	17.845	14.839	15.233	12.338	12.194
89-Ac	106.759	105.838	102.846	90.894	87.681	19.842	19.078	15.865	18.405	15.227	15.712	12.650	12.499
90-Th	109.630	108.671	105.592	93.334	89.942	20.460	19.688	16.296	18.977	15.620	16.200	12.966	12.808
91-Pa	112.581	111.575	108.408	95.851	92.271	21.102	20.311	16.731	19.559	16.022	16.700	13.291	13.120
92-U	115.591	114.549	111.289	98.428	94.648	21.753	20.943	17.163	20.163	16.425	17.218	13.613	13.438
93-Np	118.619	117.533	114.181	101.005	97.023	22.417	21.596	17.614	20.774	16.837	17.740	13.945	13.758
94-Pu	121.720	120.592	117.146	103.653	99.457	23.097	22.262	18.066	21.401	17.254	18.278	14.279	14.082
95-Am	124.876	123.706	120.163	106.351	101.932	23.793	22.944	18.525	22.042	17.677	18.829	14.618	14.411
96-Cm	128.088	126.875	123.235	109.098	104.448	24.503	23.640	18.990	22.699	18.106	19.393	14.961	14.743
97-Bk	131.357	130.101	126.362	111.896	107.023	25.230	24.352	19.461	23.370	18.540	19.970	15.309	15.079
98-Cf	134.683	133.383	129.544	114.745	109.603	25.971	25.080	19.938	24.056	18.980	20.562	15.661	15.420
99-E	138.067	136.724	132.781	117.646	112.244	26.729	25.824	20.422	24.758	19.426	21.166	16.018	15.764
100-Fm	141.510	140.122	136.075	120.598	114.926	27.503	26.584	20.912	25.475	19.879	21.785	16.379	16.113

TABLE 4

TYPICAL MAIN PHOTON ENERGY DISTRIBUTION MATRIX

	Energy (mc^2)														
	Absorption or Loss* At Each Interaction														
Interaction No.:	1			2			3		4		5	Absorption per photon	Weighted absorption	Weighted Loss	
Interaction Kind:	pp	pe	sc	pp	pe	sc	pe	sc	pe	sc	sc				
Weight															
0.28	(8.0)[†]	-	-	-	-	-	-	-	-	-	-	-	-	2.240[†]	
0.02	-	8.0	-	-	-	-	-	-	-	-	-	8.00	0.160	-	
0.20	-	-	4.0	(4.00)[†]	-	-	-	-	-	-	-	4.00	0.800	0.800[†]	
0.05	-	-	4.0	-	(4.00)	-	-	-	-	-	-	4.00	0.200	0.200	
0.15	-	-	4.0	-	-	(2.10)	1.90	-	-	-	-	5.90	0.885	0.315	
0.20	-	-	4.0	-	-	(2.10)	-	1.0	0.90	-	-	5.90	1.180	0.420	
0.10	-	-	4.0	-	-	(2.10)	-	1.0	-	0.40	(0.50)	5.40	0.540	0.260	
1.00													3.765	4.235[†]	= 8.00

*Energy losses are given in parentheses

[†] Energy transferred to position-electron pair i.e. pair production (not an actual energy loss); the transferred energy is distributed as in Tables 5 and 6

TABLE 5

PAIR PRODUCTION ENERGY DISTRIBUTION MATRIX FOR THE MAIN PHOTON FIRST COLLISION SHOWN IN FIGURE 9

	Energy (mc^2)															
	Absorption or Loss* At Each Interaction															
nteraction No.**:	1		1'		2		2'		3	3'		4'	Absorption per photon	Weighted absorption	Weighted Loss	
Interaction Kind:	pe	sc	pe	sc	pe	sc	pe	sc	sc	pe	sc	pe				
Weight																
0.07	(1.0)	-	1.0	-	-	-	-	-	-	-	-	-	1.0	0.070	0.070	
0.03	-	(0.5)	1.0	-	0.50	-	-	-	-	-	-	-	1.5	0.045	0.015	
0.09	-	(0.5)	-	0.60	0.50	-	0.40	-	-	-	-	-	1.5	0.135	0.045	
0.03	-	(0.5)	-	0.60	-	0.20	0.40	-	(0.30)	-	-	-	1.2	0.036	0.024	
0.04	-	(0.5)	-0.60	0.60	-	0.20	-	0.30	(0.30)	0.10	-	-	1.2	0.048	0.032	
0.02	-	(0.5)	-	0.60	-	0.20	-	0.30	(0.30)	-	0.07	0.03	1.2	0.024	0.016	
0.28														0.358	0.202	= 0.560

*Energy Losses are given in parentheses.

**"Primed" numbers denote "second" member of 0.51 MeV photon pair.

TABLE 6

PAIR PRODUCTION ENERGY DISTRIBUTION MATRIX FOR THE MAIN PHOTON SECOND COLLISION SHOWN IN FIGURE 9

	Energy (mc^2)													
	Absorption or Loss* At Each Interaction													
Interaction No.**:	1		1'	2		3		4		5	Absorption per photon	Weighted absorption	Weighted Loss	
Interaction Kind :	pe	sc	sc	pe	sc	pe	sc	pe	sc	pe				
Weight														
0.05	1.00	-	(1.00)	-	-	-	-	-	-	-	1.00	0.050	0.050	
0.06	-	0.20	(1.00)	(0.80)	-	-	-	-	-	-	0.20	0.012	0.108	
0.07	-	0.20	(1.00)	-	(0.20)	0.60	-	-	-	-	0.80	0.056	0.084	
0.01	-	0.20	(1.00)	-	(0.20)	-	0.50	0.10	-	-	0.80	0.008	0.012	
0.01	-	0.20	(1.00)	-	(0.20)	-	0.50	-	0.08	0.02	0.80	0.008	0.012	
0.20												0.134	0.266	= 0.400

*Energy Losses are given in parenteses

**"Primed" numbers denote "second" member of 0.51 MeV photon pair.

TABLE 7

ENERGY ABSORPTION TERMINATION DISTRIBUTION FOR FIGURE 9 HISTORY

	Photon Weight	Energy (mc^2)
MAIN HISTORY	0.02	8.0
	0.20	4.0
	0.05	4.0
	0.15	5.9
	0.20	5.9
	0.10	5.4
FIRST PP	0.07	7.0
	0.03	7.5
	0.09	7.5
	0.03	7.2
	0.04	7.2
	0.02	7.2
SECOND PP	0.05	1.0
	0.06	0.2
	0.07	0.8
	0.01	0.8
	0.01	0.8

TABLE 8

TYPICAL VALUES OF THE CHARACTERISTIC DISTANCE $d_{1/2}$(IN UNITS OF λ (E))

ENERGY E (MeV)	ATOMIC NUMBER, Z			
	13	26	50	82
0.412	0.63	—	—	0.09
0.662	0.60	0.35	0.18	0.08
1.25	0.55	0.30	0.17	0.07

TABLE 9

SINGLE AND DOUBLE SCATTER TOTAL NUMBER ALBEDO RATIOS

R_{ss}/R_{ds} ($R_{ss} = \alpha_{ss}/\alpha_T$ AND $R_{ds} = \alpha_{ds}/\alpha_T$)

ENERGY E (MeV)	ATOMIC NUMBER, Z			
	13	26	50	82
0.2	.36/.24	–	–	.965/.031
0.412	.27/.21	–	–	.90/.09
0.662	.24/.21	.39/.27	.65/.24	.88/.11
1.25	.22/.19	.34/.28	.58/.24	.79/.14
2.0	.21/.17	–	–	.65/.11
4.0	.14/.12	–	–	.30/.07
6.0	.13/.11	–	–	.15/.05

TABLE 10

COMPARISON OF MONTE CARLO AND ANALYTIC SINGLE SCATTER TOTAL NUMBER ALBEDOS α_{SS}

MATERIAL	ENERGY (MeV)	d (cm)	L (cm)	$(\alpha_{SS})_{anal.}$	$(\alpha_{SS})_{mc}$
				X 10^{-2}	
Al	.622	17.0	17.0	6.56	6.42
			2.5	5.47	5.40
	1.25	17.0	17.0	4.71	4.79
			4.25	4.33	4.20
Fe	.662	6.0	6.0	4.29	4.48
			1.19	3.61	3.22
	1.25	6.0	6.0	5.82	5.77
			1.5	5.37	5.61
Sn	.662	5.0	5.0	2.92	2.89
			0.752	2.57	2.76
	1.25	7.0	7.0	2.48	2.13
			1.75	2.38	2.28
Pb	.662	4.0	4.0	1.12	1.30
			0.432	1.05	0.97
	1.25	4.0	4.0	1.02	1.06
			1.0	1.00	1.22

TABLE 11

PHOTOFRACTIONS AND EFFICIENCIES FOR 3" x 3" NaI (Tℓ) UNCLAD AND CLAD CRYSTALS EXPOSED TO A 10cm DISTANT POINT SOURCE*
(1.18 g/cm^2 ABSORBER)

Photon Energy (MeV)	Photofraction		Efficiency	
	P_u	P_c	ϵ_u	ϵ_c
4.45**	.280 (.278) (44)	–	.727 (.726) (44)	–
2.754	.268 (.254) (44)	.251	.423	.434
2.615	.274 (.262) (44)	.256	.426 (.428) (44)	.433
1.276	.402	.365	.506	.519
.835	.500	.449	.576	.584
.6616	.571 (.562) (44) (.569) (48)	.507	.615 (.619) (44)	.622
.511	.662	.588	.661	.667
.32	.845 (.832) (48)	.749	.766	–

---

* Unclad reference data indicated in parentheses.

** *4" x 4" Crystal and Parallel Beam*

REFERENCES

1. VAN TUYL, H. H., "BREMRAD - A Computer Code for External and Internal Bremsstrahlung Calculations," HW-83784m Hanford Laboratories (1964).

2. STEYN, J. J., "Code BREMRAD for the IBM-7094 Computer," NUS-TM-NA-91, NUS Corporation (1968).

3. RUDY, G. C., "Code BREMRAD for the IBM-360 Computer," NUS-TM-NA-109, NUS Corporation (1970).

4. STEYN, J. J. and STRAHL, J. T., "NUALGAM - A Monte Carlo Code to Predict the Angular Energy Escape of Gamma Photons from Cylindrical Sources," NUS-536, NUS Corporation (1969).

5. TEXTOR, R. E., and VERBINSKI, V. V., "05S: A Monte Carlo Code for Calculating Pulse Height Distributions Due to Monoenergetic Neutrons Incident on Organic Scintillators," ORNL-4160 (February 1968).

6. ____________________ "05S + SMOOTHIE," PSR-14, Radiation Shielding Information Center, Oak Ridge National Laboratory (December 1970).

7. WARNER, G. G., Mathematics Division, Oak Ridge National Laboratory (Private Communication, April 1968).

8. SNYDER, S. S., Health Physics Division, Oak Ridge National Laboratory (Private Communication, April 1968).

9. WARNER, G. G., and CRAIG, A. M., Jr., "ALGAM, A Computer Program for Estimating Internal Dose from Gamma-Ray Sources in a Man Phantom," ORNL-TM-2250 (June 1968).

10. STEYN, J. J., and HUANG, R., "Final Report for Unmanned Spacecraft RTG Shield Optimization Study," NUS-679, NUS Corporation (1970).

11. CASHWELL, E. D., and EVERETT, C. J., "Monte Carlo Method for Random Walk Problems," Pergamon Press (1959).

12. SHREIDER, YU A. (Editor); "The Monte Carlo Method," Pergamon Press (1966).

13. WHITE-GRODSTEIN, G., "X-Ray Attenuation Coefficients from 10 keV to 100 MeV," NBS Circular 583 (1957).

14. McGINNIES, R. T., "X-Ray Attenuation Coefficients from 10 keV to 100 MeV," Supplement to NBS Circular 583 (1959).

15. HUBBELL, J. H., and BERGER, M. J., "Photon Attenuation and Energy Absorption Coefficients Tabulations and Discussion," NBS report 8681 (1966).

16. STORM, E., GILBERT, E., and ISRAEL, H., "Gamma Ray Absorption Coefficients for Elements 1 to 100 Derived from Theoretical Values of NBS," LASL-2237 (1958).

17. HUBBELL, J. H., "Photon Cross Sections, Attenuation Coefficients, and Energy Absorption Coefficients from 10 keV to 100 GeV," NSRDS-NBS 29, (1969).

18. KAHN, H., "Applications of Monte Carlo," AECU-3259 (1954).

19. GRAY, P. R., "Auger Effect in the Heaviest Elements," Phys. Rev., <u>101</u>, 4, (1956), 1306.

20. FINE, S., and HENDEE, C. F., "X-Ray Critical-Absorption and Emission Energies in keV," Nucleonics, <u>13</u>, 3, Data Sheet #1 (1955) 36.

21. BEARDEN, J. A., "X-Ray Wavelengths," U. S. Atomic Energy Commission, NYO-19586 (1964).

22. BEARDEN, J. A., "X-Ray Wavelengths and X-Ray Atomic Energy Levels," NSRDS-NBS 14 (September 1967).

23. HEATH, R. L., "Scintillation Spectrometry Gamma-Ray Spectrum Catalogue," IDO-16880-1, Phillips Petroleum Co. (1964).

24. SKARSGARD, L. D., and JOHNS, H. E., "Iterative Response Correction for a Scintillation Spectrometer," Rad. Res., <u>9</u>, (1958) 261.

25. SKARSGARD, L. D., "The Spectral Distribution of Ionizing Radiations," Ph.D. Thesis, Dept. of Physics, University of Toronto (1960).

26. EVANS, R. D., "The Atomic Nucleus," McGraw-Hill Book Co., Inc., (1955).

27. STEYN, J. J., and BORN, U. "Code CUGEL: A Code to Unfold Ge (Li) Spectrometer Polyenergetic Gamma Photon Experimental Distributions," NUS-692, NUS Corporation (1970).

28. MAEDER, D., MULLER, R., and WINTERSTEIGER, V., "Uber die Linienform monochromatischer Y-Strahlungen im Szintillationsspektrographen," Helvetica Physica Acta, 27 (1954) 3.

29. PIEPER, A. G. and BEACH, L. A., "Stochastic Estimates of the Penetration of Gamma Rays Through Slab Shields," NRL-5981, Naval Research Laboratory (September 1963).

30. PEEBLES, G. H., "Gamma-Ray Transmission Through Finite Slabs," R-240, The Rand Corporation (1952).

31. BENNETT, B., BURKE, G. and BECK, H., "Experimental and Theoretical Studies of the Transport of Gamma Rays Through Slab Shields," HASL-205, USAEC, Health and Safety Laboratory, NY (January 1969).

32. JAEGER, R. G., Editor-in Chief, "Engineering Compendium on Radiation Shielding," Vol. I, Shielding Fundamentals and Methods, Springer-Verlag, Inc., N. Y. (1968) pp. 236-238.

33. STEYN, J. J. and ANDREWS, D. G., "Comprehensive Experimental Differential Number, Energy and Dose Albedos for Semi-Infinite Media for Normally-Incident Gamma Photons," NUS-665, NUS Corporation (1970).

34. STEYN, J. J. and ANDREWS, D. G., "Experimental and Differential Number, Energy and Exposure Albedos for Semi-Infinite Media for Normally Incident Photons," Nucl. Sci. Eng., 27 (1967) 318.

35. DOGGETT, W. O. and BRYAN, F. A. Jr., "Theoretical Dose Transmission and Reflection Probabilities for 0.2-10.0 MeV Photons Obliquely Incident on Finite Concrete Barriers," Nucl Sci. Eng., 39 (1970) 92.

36. JONES, T. H., SCOFIELD, W. E., HAGGMARK, L. G. and GURNEY, W. J., "Experimental Determination of the Gamma-Ray Dose Albedos of Concrete, Aluminum and Steel," USNRDL-TR-790, US Naval Radiological Defense Laboratory (1964).

37. BERGER, M. J. and RASO, D. J., "Backscattering of Gamma Rays," NBS-5982, Second Edition, National Bureau of Standards (1960).

38. DAVISSON, C. M. and BEACH, L. A., NRL Quarterly of Nuclear Science and Technology (U.S. Naval Research Laboratory) Jan. 1, 1960, p. 43.

39. DAVISSON, C. M. and BEACH, L. A., Private Communication (1964) page 245 of reference (32).

40. BAARLI, J., "An Experimental Study of Gamma-Ray Backscattering Using Scintillation Gamma-Ray Spectroscopy," Archiv for Mathematik og Naturvidenskap, (Oslo) B. LV. Nr. 8 (1961) 121.

41. RASO, D. J., "Monte Carlo Calculations on the Reflection and Transmission of Scattered Gamma Radiation," TO-B 61-39, Technical Operations Inc. (1962).

42. PERKINS, J. F., "Monte Carlo Calculation of Gamma-Ray Albedos of Concrete and Aluminum," J. Appl. Phys., 26, 6 (1955) 655.

43. RASO, D. J., "Scattering of Gamma Rays in Laminar Media," Radiation Research, <u>19</u>, 384 (1963).

44. MILLER, W. F., and SNOW, W. J., "Monte Carlo Calculations of the Energy Loss Spectra for Gamma Rays in Sodium Iodide and Cesium Iodide," ANL-6318, Argonne National Laboratory (1961).

45. HYODO, T., "Backscattering of Gamma Rays," Nucl. Sci. Eng., 12 (1962) 178.

46. BULATOV, B. P. and GARUSOV, E. A., "Co^{60} and Au^{198} Gamma Ray Albedos of Various Materials," J. Nucl. Energy, Part A: Reactor Science, 11 (1960) 159.

47. MANAGAN, W. W., Private Communication, Harshaw Chemical Co. (January 30, 1962).

48. ZERBY, C. D. and MORAN, H. S., "Calculation of the Pulse-Height Response of NaI(Tℓ) Scintillation Counters," Nuclear Instruments and Methods, 14 (1961) pp. 115-124.

49. STEYN, J. J. and ANDREWS, D. G., "A Comprehensive System for Computer Gain Changing of Scintillation Spectra," Nucl. Sci. Eng., 35 (1969) 399.

50. STEYN, J. J. and ANDREWS, D. G., "Empirical Photofractions for NaI(Tℓ) Scintillation Crystals," Nucl. Instr. and Meth., 68 (1969) 118.

51. IRVING, D. C. *et al.*, 05R, A General-Purpose Monte Carlo Neutron Transport Code, Report ORNL-3622, Oak Ridge National Laboratory, February, 1965.

52. VERBINSKI, V. V., TEXTOR, R. E., BURRUS, W. R., and LOVE, T. A., Neutron Response of the NE-213 Scintillator From 0.2 MeV to 22 MeV, (to be published).

53. STEYN, J. J. and LAMERS, G. B., "A Proposed Spectrometer for Radioisotope Power Source Fast Neutron and Gamma Photon Experiments," NUS-486, NUS Corporation (July 1968).

54. Santoro, R. T., Love, T. A., Burrus, W. R., Courtney, J. C., Textor, R. E., The Effects of Plastic Layers and Light Pipes on the Efficiency of Organic Neutron Scintillators, ORNL-3892, Oak Ridge National Laboratory, (to be published).

APPENDIX I

Brief Description of the 05S Code (5, 6)

APPENDIX I

Brief Description of the 05S Code (5, 6)

05S is a Monte Carlo code which directly simulates the experimental techniques used to obtain the pulse height distribution for a parallel beam of mono-energetic neutrons incident on organic scintillator systems (5, 6).

The code is patterned after the far more general 05R code (51) and, for the sake of brevity, at least passing familiarity with that code is assumed. Due to the nature of the specialization which 05S represents, a considerable amount of the memory storage required for 05R is avoided allowing the analysis of neutron events as they occur rather than after all have occurred.

Although the code is capable of calculating the pulse height distribution for neutrons in the energy range 20 KeV to 70 MeV, experimental verification presently exists only for the range 200 KeV to 20 MeV. The code is written in the FORTRAN IV language for the IBM-360/91 computer.

In this appendix some general features as given in reference (5) are repeated. An example input/output sample is given in Appendix V of report Volume II

INTRODUCTION

In the calculation of the response function of an organic scintillator to neutrons of all energies it is necessary to obtain pulse height distributions for mono-energetic neutrons at energies where experimental determinations are often quite impractical because of problems with background and absolute monitoring of neutron flux. For this reason it is desirable to have a method for accurately predicting the pulse height distribution per unit neutron flux over a wide range of energy and at reasonably small increments of energy. Because it allows direct simulation of typical calibration experiments with mono-energetic neutrons while utilizing all available empirical information (e.g., kinematics, angular distributions, cross-sections, light yields), a Monte Carlo "experiment" is frequently used for this purpose.

The Monte Carlo "experiment" follows the course of each neutron through the scintillator and obtains the energy-deposits of the ions produced by elastic scatterings and reactions. The light pulse produced by the neutron is obtained by summing up the contributions of the various ions with the use of appropriate light vs. ion-energy tables.

To a large extent the 05S code is patterned after the far more general neutron transport 05R code(51). The latter code covers the energy range from 77.13 MeV to 0.070×10^{-3} eV. The energy range is divided into 40 supergroups, each a factor of 2 apart; and each supergroup is divided into 2^n subgroups, where $n = 0, 1, \ldots, 9$, and n is specified by the user. Since 05R allows the treatment of complex geometries consisting of as many as 16 media with any practical number of nuclides per medium, a tremendous amount of cross-section information may be required. The code stores in memory the scattering probabilities for one supergroup and processes neutrons through that supergroup in batches of from 200 to 2000 neutrons. The scattering probabilities for the next lower supergroup are then read into memory and the process is repeated. The product of an 05R run is a magnetic tape(s) which contains information describing each reaction which occurred. The results of the Monte Carlo experiment are found by analysis of this tape(s).

Since the 05S code is concerned with only one medium, namely: the scintillating material, consisting of two elements and a total of eight reaction-types or scatterers, in the energy range 70 MeV to 200 KeV, the amount of cross-section information is small enough that the information for all supergroups may be stored in memory simultaneously. The result of interest is that neutrons may be followed individually, their histories analyzed as they occur, and, upon completion of the experiment, the results analyzed to obtain the pulse height distribution during one pass on the computer.

The other fundamental differences between the two codes are that 05S does allow the absorption of neutrons, but does not allow splitting or Russian roulette (biased weighting schemes).

A discussion of the use and experimental verification of the calculations of 05S is presented in a separate report on the calibration of the scintillator(52).

This IBM-360/91 version of the 05S code was obtained from the Radiation Shielding Information Center (RSIC), Oak Ridge National Laboratory(6). Reference (5) consists of a 'user's manual' for the 05S code, the XSECT code must be run to prepare the cross-section tape for 05S. The XSECT code is part of the 05R package obtainable from RSIC/ORNL. Both 05S and XSECT were made operational for NASA/GSFC by NUS Corporation.

A general treatment of the physics and kinematics of the organic scintillator as a neutron detector is given in reference (53).

O5S: General Features

Energy Units and Cross-Sections

Input and output energies for O5S are conventional eV units. Internal calculations are made with energy represented in neutron speed-squared units (cm^2/sec^2). The conversion for neutron energy in eV to speed squared in cm^2/sec^2 is

$$1\ cm^2/sec^2 = 1.913220092 \times 10^{12}\ eV.$$

O5S requires mean-free-flight paths and cumulative reaction probabilities in the manner provided by Code 6 of XSECT(51) (the cross-section handling code of the O5R package). Presently O5S uses the 12 energy supergroups from 77.13 MeV ($2^{67}\ cm^2/sec^2$) to 18.83 KeV ($2^{55}\ cm^2/sec^2$) with 128 subgroups per supergroup.

Scintillator System

Two geometrical situations for cylindrical scintillators are presently available. The first as in Figure I-1 is one of considerable interest. A parallel beam of mono-energetic nuetrons is incident on the portion of the lateral surface of the scintillator denoted by the negative x-axis.

In the second situation, as in Figure I-2, the beam of neutrons is incident on a concentric circular portion of the flat surface of a scintillator system consisting of:

(1) A C_1 detector whose radius is that of the scintillator and whose thickness is given in equivalent units of the scintillating material. This detector is often used in experiments to prevent the entrance of

SCINTILLATOR SYSTEM WITH NEUTRONS INCIDENT ON LATERAL SURFACE

ORNL-DWG 67-12335

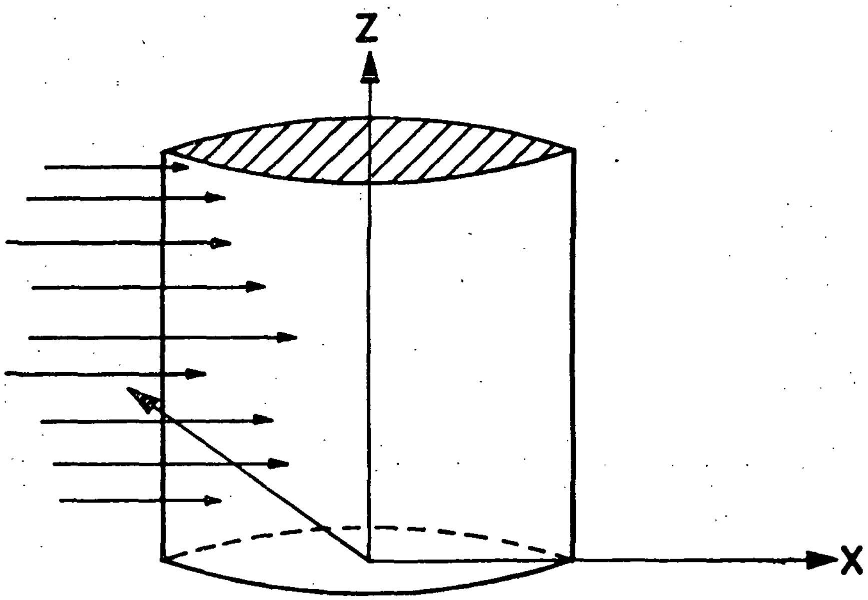

Figure I-1

SCINTILLATOR SYSTEM WITH NEUTRONS INCIDENT ON FLAT SURFACE

ORNL-DWG 67-12336

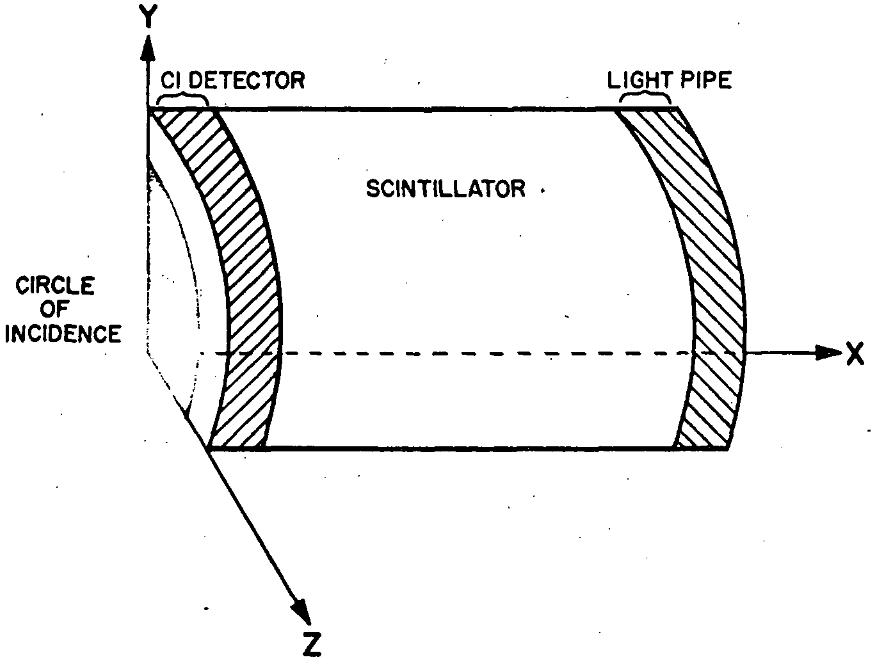

Figure I-2

charged particles into the scintillator and tends to slow down incident neutrons.(54)

(2) The scintillator proper.

(3) A light pipe whose radius is that of the scintillating material. This unit has the effect of scattering neutrons back into the scintillator.(54)

Generation of Neutron Histories

A neutron history is generated in much the same manner as is used in O5R.

(1) The neutron is given a NAME, a unique integer distinguishing it from other neutrons within the same case; initial energy and direction, and spatial coordinates of the point of incidence.

(2) The path length to the next reaction point is chosen by multiplying the mean free path, for the current neutron energy, by an exponentially distributed random number. The coordinates of the next reaction point are then calculated. When this point is outside the system, the neutron has escaped and analysis of the neutron history inside the scintillator is performed.

(3) The reaction which is to occur at the point chosen is selected by a random process from the possible reactions, given in Table I-1 according to the various partial cross-sections.

(4) The appropriate reaction routine calculates the parameters associated with the neutron after reaction, unless absorption occurs, and the energies of the reaction products.

TABLE I-1

NEUTRON-HYDROGEN, NEUTRON-CARBON REACTIONS AND PARAMETERS

Reaction	Q-Value (MeV)		Threshold (MeV)
H(n,n)H	0		0
$^{12}C(n,n)^{12}C$	0		0
$^{12}C(n,n'\gamma)^{12}C$	4.43		4.8
$^{12}C(n,\alpha)^{9}Be$	5.71		6.18
$^{12}C(n,n'3\alpha)$	12.73	(56.93%)	13.8
	11.1	(5.14%)	12.01
	9.63	(37.93%)	10.42
	7.656		8.3
$^{12}C(n,p)^{12}B$	12.613		13.69
$^{12}C(n,pn)^{11}B$	15.957		17.29
$^{12}C(n,2n)^{11}C$	18.72		20.13

Note: Q-values (always negative) are used as positive in O5S. Since a pulse shape discriminator is used to eliminate γ-pulses experimentally, the γ from the $^{12}C(n,n'\gamma)^{12}C$ reaction is ignored. For the $^{12}C(n,n'3\alpha)$ reaction the Q-values and branching ratios are those found to give best agreement with 14.4 MeV results. The 7.656 MeV Q-value for $^{12}C(n,n'3\alpha)$ is used only in the rare cases where the cross-section is finite but the other Q-levels are energetically impossible.

(5) The light yield of the reaction products is calculated unless the reaction occurred outside the scintillator proper but inside the system.

(6) If the neutron value has vanished (by absorption, escape from the system or loss of energy to less than 20 KeV) the neutron history is analyzed. Otherwise the neutron continues to be followed through the system.

Reaction Analysis

The light yield from each product of a reaction is calculated from the appropriate light *vs.* energy table. Presently there are tables for proton, alpha particle and ^{12}C nucleus light. The light for a ^{9}Be, ^{12}B, ^{11}B or ^{11}C nucleus is assumed to be the same as for a ^{12}C nucleus of the same energy.

Since proton escape is considered two energies are calculated for the proton after the reaction - the energy with which the proton left the reaction and the amount of that energy not lost in the scintillator. The amount of light lost by the proton inside the scintillator is the difference of the light yields corresponding to the two energies.

The light yield from each of a neutron's reactions is summed over all its reactions.

Neutron History Analysis

For each neutron history the total amount of light produced during all its reactions is stored as a single pulse in a histogram. The light interval ℓ in which the pulse is stored is given by

$$\ell = 1 + A^{0.5}/0.015,$$

where A is the total light yield and the constant 0.015 is called the bin width factor. The width of the interval $B_{\ell-1}$ to B_ℓ in light units (cobalts) is given by

$$B_\ell - B_{\ell-1} = (0.015\ell)^2 - (0.015(\ell-1))^2.$$

One cobalt is the base-line intercept of a straight line fit to the high end of a ^{60}Co gamma-ray pulse height distribution (linear plot).

Pulse Height Distribution Calculation

The histogram ("unsmeared" pulse height distribution) which results from the Monte Carlo experiment is composed of light intervals δA which vary proportionately to the square root of the light A. The final (smeared) pulse height distribution is composed of light intervals δA in which $\delta A/A$ is constant. Each interval of the final pulse height distribution represents the integral over that interval of the initial histogram convoluted by a Gaussian function of specified width, normalized by the number of incident neutrons and the interval width. The result of this process is a smeared distribution which matches the smearing due to photomultiplier statistics, and is absolutely normalized to one incident neutron.

APPENDIX II

The Kahn Monte Carlo Technique of Selection of Scattered Photon Energy and Direction(18)

22. Picking from the Klein-Nishina Scattering Formula

It can be shown that if a γ ray of energy α (in mc^2) is traveling in a cloud of free electrons, then it has a probability $g(x,\alpha)dx\,dl$ of having a collision in the distance dl and emerging from this collision with an energy α' such that

$$\frac{\alpha}{x} \leq \alpha' \leq \frac{\alpha}{x} + \frac{\alpha}{x^2}\,dx$$

$$g(x,\alpha)dx = \begin{cases} \dfrac{n\pi\alpha_0^{\,2}}{\alpha}\left(\cos^2\theta - 1 + x + \dfrac{1}{x}\right)\dfrac{dx}{x^2} & 1 \leq x \leq 1 + 2\alpha \\ 0 & x \leq 1,\ 1 + 2\alpha \leq x \end{cases}$$

where $\cos\theta = 1/\alpha = x/\alpha + 1$ = cosine of angle of scattering.

a_0 = classical radius of electron

$= 2.81833 \times 10^{-13}$ cm

$\pi a_0^2 = .249536 \times 10^{-24}\ \text{cm}^2$

n = number of electrons per cc

$\alpha' = x\alpha$ = energy of γ ray after collision.

If $\sigma(\alpha) = \int_1^{1+2\alpha} g(\alpha,x)dx$ then $\frac{\sigma(\alpha)}{n}$ is the so-called Compton scattering cross section and is tabulated in R-170 Tables 5 and 6. The probability that the γ ray will have any kind of scattering collision in the distance dl is then $\sigma(\alpha)dl$. $g(\alpha,x)$ can now be written in the form:

$$g(\alpha,x) = n\sigma(\alpha)f(\alpha,x)$$

where $$f(\alpha,x) = \frac{1}{x^2}(\cos^2\theta - 1 + x + \frac{1}{x})/K(\alpha)$$

and $$K(\alpha) = \int_1^{1+2\alpha} (\cos^2\theta - 1 + x + \frac{1}{x}) \frac{dx}{x^2}$$

$f(\alpha,x)$ is then the p.d.f. for the energy ratio x of a γ ray which enters collison with energy α. The normalizing factor, $K(\alpha)$, is shown in Graph 4.

Graphs and Tables of the equation

$$R = \int_1^x f(\alpha,x)dx$$

can also be found in R-170.

Empirical fits to these functions could be made, but it is undesirable to have to fit a two variable function unless absolutely necessary.

Several exact methods for picking out of the Klein Nishina p.d.f. will now be discussed. This is partly pedagogy and partly because the method used may depend on the particular section being picked from or the available machine.

---

[1] Actually $\cos\theta$ and $1/\alpha'$ as a function of R and α are tabulated, not x.

First, techniques in which x is drawn from a p.d.f. $m(x)$ and then accepted if R is $\leq T(x)$ will be considered. This implies that $E \cdot f(\alpha,x) = m(x)T(x)$.

a. Let

$$m(x) = \frac{1}{2\alpha} \qquad 1 \leq x \leq 1 + 2\alpha.$$

$$T(x) = \frac{1}{x^2}\left(\cos^2\theta - 1 + x + \frac{1}{x}\right)$$

It is clear that the expression to the right of the proportion sign is ≤ 2, since $\frac{(\cos^2\theta - 1)}{x^2} \leq 0$ and $\frac{1}{x^2}(x + \frac{1}{x}) \leq 2$ in the region $1 \leq x \leq 1 + 2\alpha$.

So if

$$T(x) = \frac{1}{2x^2}\left(\cos^2\theta - 1 + x + \frac{1}{x}\right)$$

the inequality $0 \leq T(x) \leq 1$ is satisfied. The efficiency is

$$\begin{aligned} E_a &= \frac{m(x)T(x)}{f(x)} \\ &= \frac{K(\alpha)}{4\alpha} \end{aligned}$$

b. Let

$$m(x) = \frac{1}{x\ln(1+2\alpha)} \qquad 1 \leq x \leq 1 + 2\alpha$$

$$T(x) = \frac{1}{2x}\left(\cos^2\theta - 1 + x + \frac{1}{x}\right)$$

$$E_b = \frac{K(\alpha)}{2\ln(1+2\alpha)}$$

---

c. Let $m(x) = \frac{1+2\alpha}{a\alpha}\ \frac{1}{x^2}$ $\qquad 1 \le x \le 1 + 2\alpha$

$$T(x) = (\cos^2\theta - 1 + x + \tfrac{1}{x})/(1 + 2\alpha + \tfrac{1}{1+2\alpha})$$

$$E_c = \frac{(1+2\alpha)^2\ K(\alpha)}{(2\alpha)\left[1 + (1+2\alpha)^2\right]}$$

That $0 \le T(x) \le 1$ can be verified by noting that $x + \frac{1}{x}$ is a monotonically increasing function in the region $1 \le x$ and that $\cos^2\theta - 1$ has a maximum value of 0. Therefore the function $(\cos^2\theta - 1 + x + \frac{1}{x}) \le x + \frac{1}{x} \le 1 + 2\alpha + \frac{1}{1+2\alpha}$ if $1 \le x \le 1 + 2\alpha$.

d. It is also possible to break up $f(x,\alpha)$ into the sum of two p.d.f.'s; for example:

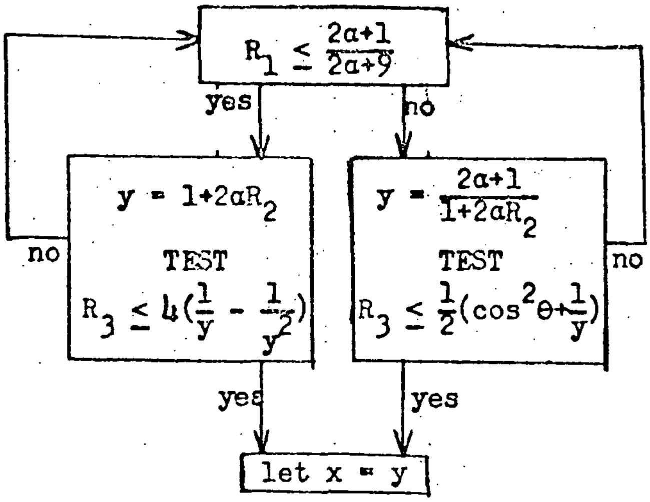

As always.

$$E_d \cdot f(x) = \frac{2\alpha+1}{2\alpha+9}\ \frac{1}{2\alpha}\ 4(\frac{1}{x} - \frac{1}{x^2}) + \frac{8}{2\alpha+9} \cdot \frac{2\alpha+1}{2\alpha x^2}\ \frac{1}{2}(\cos^2\theta+\frac{1}{x})$$

$$= \frac{2\alpha+1}{2\alpha+9} \cdot \frac{2}{\alpha}\ (\frac{1}{x} - \frac{1}{x^2} + \frac{1}{x^3} + \frac{\cos^2\theta}{x^2})$$

$$E_d = \frac{(2\alpha+1)}{(2\alpha+9)}\ \frac{2K(\alpha)}{\alpha}$$

The efficiencies E_a through E_d are shown in graph number 5.

NUS CORPORATION

■ 4 RESEARCH PLACE, ROCKVILLE, MARYLAND 20850 U.S.A. ■ TELEPHONE (301) 948-7010 CABLE: NUSWASH